ABSTRACT

Convection from Realistic Ice Roughness on a Simulated NACA 0012 Airfoil

Timothy Andrew Shannon, M.S.M.E.

Mentor: Stephen T. McClain, Ph.D.

Ice roughness properties are critically important to the development of ice accretions on aircraft surfaces. Ice accretions degrade aircraft performance by increasing the skin friction drag, increasing the weight of the aircraft, and decreasing the lift and stall angle. During the aircraft design process, icing effects are simulated using ice predictions codes such as LEWICE. These codes can be improved by providing a better characterization of the convective enhancement caused by ice roughness. Previous studies have considered convective enhancement from ice roughness surfaces with constant properties in the flow direction and in a flow with negligible acceleration. This work investigates convective enhancement from realistic ice roughness surfaces by 1) including roughness variations in the streamwise direction as measured in the Icing Research Tunnel at NASA Glenn with laser scanning and 2) including a flow acceleration profile in the flow direction by installing a foam insert on the wind tunnel ceiling.

Convection from Realistic Ice Roughness on a Simulated NACA 0012 Airfoil

by

Timothy Andrew Shannon, B.S.M.E.

A Thesis

Approved by the Department of Mechanical Engineering

_____

William Jordan, Ph.D., Chairperson

Submitted to the Graduate Faculty of
Baylor University in Partial Fulfillment of the
Requirements for the Degree
of

Master of Science in Mechanical Engineering

Approved by the Thesis Committee

_____

Stephen T. McClain, Ph.D., Chairperson

_____

Joseph Kuehl, Ph.D.

_____

Yang Li, Ph.D.

Accepted by the Graduate School

August 2015

_____

J. Larry Lyon, Ph.D., Dean

*Page bearing signatures is kept on file in the Graduate School.*

Copyright © 2015 by Timothy Andrew Shannon

All rights reserved

TABLE OF CONTENTS

LIST OF FIGURES ..... vii

LIST OF TABLES ..... xi

NOMENCLATURE ..... xii

ACKNOWLEDGMENTS ..... xvi

DEDICATION ..... xvii

CHAPTER ONE ..... 1

Introduction ..... 1

Motivation ..... 1

Objectives ..... 3

Presentation Outline ..... 3

CHAPTER TWO ..... 5

Technical Background ..... 5

Fluid Mechanics and Heat Transfer ..... 5

Boundary Layers ..... 5

Airfoils ..... 10

Surface Roughness ..... 12

Aircraft Icing ..... 15

Common Icing Terms ..... 15

Ice Accretion Process ..... 17

Ice Accretion Modeling ..... 18

Ice Roughness Investigations....20
CHAPTER THREE....27
Materials and Methodology....27
Instrumented Test Plate....27
Plexiglas Sub-Plate....28
Instrumentation and Wiring....29
Mylar Film Heaters....31
Aerodynamic Features....32
Realistic Ice Roughness Surfaces....33
Implementing Lagrangian Droplet Simulator....33
Matching Roughness Parameters....34
Historical ice roughness....35
Contemporary ice roughness....38
Manufacturing Surface Panels....41
Ceiling Insert for Flow Acceleration....45
Ceiling Insert Design....45
Ceiling Insert Construction....47
Experimental Setup and Procedure....50
Convection Measurements....50
Velocity Boundary Layer Measurements....57
CHAPTER FOUR....59
Data Reduction and Uncertainty Analysis....59
Convection Measurements....59

Data Reduction Equation ..... 59
Air Properties ..... 62
Thermocouple Calibration ..... 63
Smooth Surface Validation ..... 63
Uncertainty Analysis ..... 68
Velocity Boundary Layer Measurements ..... 69
Probe Calibration ..... 69
Data Reduction Equations ..... 70
CHAPTER FIVE ..... 72
Results and Discussion ..... 72
Convection Results ..... 72
Velocity Boundary Layer Characterization ..... 80
CHAPTER SIX ..... 88
Conclusions ..... 88
Summary of Work ..... 88
Future Work ..... 89
APPENDICES ..... 90
Appendix A ..... 91
Appendix B ..... 96
Appendix C ..... 116
REFERENCES ..... 125

LIST OF FIGURES


Figure 2.1: Velocity boundary layer development on a flat plate (not to scale) .....6

Figure 2.2: Thermal boundary layer on a flat plate .....7

Figure 2.3: Surface pressure distribution on an airfoil .....11

Figure 2.4: Flow separation process .....11

Figure 2.5: Early stage ice accretion on airfoil leading edge [25] .....17

Figure 2.6: Modes of energy transfer for an unheated airfoil in icing in icing conditions [26] .....18

Figure 2.7: Comparison of measured roughness height with predicted sand-grain roughness height [29] .....20

Figure 2.8: Ordered roughness distributions used by Poinsatte et al. [31] .....21

Figure 2.9: Heat transfer enhancement with varying freestream turbulence [32] .....22

Figure 2.10: Casting of ice roughness on a NACA 0012 airfoil [27] .....23

Figure 2.11: Solid model of realistic ice roughness surface [36] .....24

Figure 2.12: Convective heat transfer coefficient contour maps for varying thermal boundary conditions [37] .....25

Figure 2.13: Roughness height measurements in Appendix O conditions [6] .....26

Figure 3.1: Solid model of test plate [4] .....28

Figure 3.2: Plexiglas sub-plate [4] .....29

Figure 3.3: Side view of test plate showing thermocouple placement from the leading edge of the Plexiglas sub-plate (dimensions in inches, flow is from left to right) [4] .....30

Figure 3.4: Side view of test plate [4] .....31

Figure 3.5: Layout of the heated sections on the Plexiglas sub-plate (dimensions in inches, flow is from left to right) [4] ..... 32

Figure 3.6: Isometric view of test plate with Mylar film heaters installed in the second and third heated sections [4] ..... 33

Figure 3.7: Flow chart of algorithm used in the Lagrangian droplet simulator ..... 34

Figure 3.8: Ice accretion images for run identifiers a) 052996.04 and b) 053096.01 from Anderson et al. [34] ..... 36

Figure 3.9: Droplet distributions for the 052996.04 case corresponding to a) unconditioned simulator data, b) truncated data, c) truncated and stretched data, and d) truncated, stretched, and scaled data [4] ..... 37

Figure 3.10: A 20 mm wide section of the 113012.04 case point cloud color mapped to normal height from the self-organizing map mean manifold ..... 39

Figure 3.11: 99% Gaussian maximum roughness height variation for the 113012.04 case point cloud ..... 41

Figure 3.12: Scaled and replicated roughness distributions for the 052996.04 case (not to scale) ..... 42

Figure 3.13: Row C surface panel assemblies of a) 113012.04_IRT, b) 053096.01_x10, c) 052996.04_x10_SSL, and d) 052996.04_x10 (flow is from left to right) ..... 44

Figure 3.14: Pressure coefficient variation along a low speed NACA 0012 airfoil ..... 46

Figure 3.15: Scaled airfoil velocity variation and design velocity variation ..... 47

Figure 3.16: Solid model of ceiling insert ..... 48

Figure 3.17: Foam insert profile shown from a) side-view and b) top-view (dimensions in inches, flow is from left to right) ..... 49

Figure 3.18: Side view of overall experimental setup for a) the convection tests and b) velocity boundary layer tests (not to scale) ..... 51

Figure 3.19: Side view of convection test section ..... 53

Figure 3.20: Modified wood cart outfitted with experimental equipment ..... 54

Figure 3.21: Wiring diagram for heated sections [4] ..... 55

Figure 3.22: Wind tunnel ceiling with two-dimensional traversing system.....58

Figure 4.1: Heated section heat flow schematic (not to scale).....61

Figure 4.2: Surface maps of Smooth Laminar a) steady state temperature and b) convective heat transfer coefficient.....65

Figure 4.3: Surface maps of Smooth Turbulent a) steady state temperature and b) convective heat transfer coefficient.....66

Figure 4.4: Comparison of local experimental and theoretical Stanton numbers for the a) Smooth Laminar case and b) Smooth Turbulent case.....67

Figure 4.5: Hot-film probe calibration plot.....70

Figure 5.1: Convection coefficient contour maps without ceiling insert for a) 113012.04_IRT surface, b) 053096.01_x10 surface [5], c) 052996.04_x10_SSL surface, and d) 052996.04_x10 surface [5] (flow is from left to right).....76

Figure 5.2: Convection coefficient contour maps with ceiling insert for a) 113012.04_IRT surface, b) 053096.01_x10 surface, c) 052996.04_x10_SSL surface, and d) 052996.04_x10 surface (flow is from left to right).....77

Figure 5.3: Local Stanton number measurements for the rough surfaces in flow with negligible freestream acceleration.....79

Figure 5.4: Local Stanton number measurements for the rough surfaces in accelerating flow.....79

Figure 5.5: Velocity profiles for Smooth Laminar surface at the center of the heated sections for the a) negligible flow acceleration case [4] and b) accelerated flow case.....82

Figure 5.6: Velocity profiles for Smooth Turbulent surface at the center of the heated sections for the a) negligible flow acceleration case [4] and b) accelerated flow case.....82

Figure 5.7: Velocity profiles for 113012.04_IRT surface at the center of the heated sections for the a) negligible flow acceleration case and b) accelerated flow case.....83

Figure 5.8: Velocity profiles for 053096.01_x10 surface at the center of the heated sections for the a) negligible flow acceleration case [4] and b) accelerated flow case.....84

Figure 5.9: Velocity profiles for 052996.04_x10_SSL surface at the center of the heated sections for the a) negligible flow acceleration case and b) accelerated flow case ..... 85

Figure 5.10: Velocity profiles for 052996.04_x10 surface at the center of the heated sections for the a) negligible flow acceleration case [4] and b) accelerated flow case ..... 86

Figure 5.11: Comparison of turbulence intensities for the rough surfaces at the center of heated Section 2 for the a) negligible flow acceleration case [4] and b) accelerated flow case ..... 87

LIST OF TABLES

Table 3.1: Cases used to generate roughness data .....35

Table 3.2: Comparison of roughness parameters for the 052996.04 case throughout data conditioning [4] .....37

Table 3.3: Comparison of roughness parameters for the 053096.04 case Throughout data conditioning [4] .....38

Table 4.1: Conduction parameter values.....62

Table 4.2: Convective heat transfer coefficient measurement uncertainty .....68

Table 5.1: Convection coefficients for reported cases (units of $W/m^2K$) .....78

# NOMENCLATURE

| | |
|---|---|
| $A_{pix}$ | Pixel area (4.00E-04 $in^2$) |
| $A_t$ | Total area of heated section |
| $b^n$ | Winning codebook vector |
| $B_T$ | Correlated uncertainty (1.4 K) |
| c | Airfoil chord length |
| $c_f$ | Skin friction coefficient |
| $C_k$ | Conduction parameter for the $k^{th}$ heated section (0.9, 0.9, 1.05, 1.1, 1.05) |
| $c_p$ | Specific heat of fluid |
| $C_p$ | Pressure coefficient |
| D | Roughness element diameter |
| $D_{mean}$ | Average roughness element diameter |
| E | Voltage across heater |
| $F_s$ | Surface geometry scaling factor (10) |
| $F_t$ | Transition function |
| h | Convective heat transfer (convection) coefficient |
| H | Roughness element height OR local ceiling insert height |
| $H_s$ | Distance from test plate surface to test section ceiling without insert (12″) |
| I | Current through heater |
| $k_f$ | Thermal conductivity of fluid |
| $k_p$ | Thermal conductivity of Plexiglas (0.205 W/mK) |

| | |
|---|---|
| $L_{ha}$ | Length of heated section |
| $l_t$ | Transition length |
| N | Measurement sample size |
| $N_{f,stag}$ | Freezing fraction at stagnation point |
| $N_x^j$ | Orthogonal distance from an ice surface point to the mean ice shape |
| P | Roughness element spacing |
| $P_{mean}$ | Average roughness element spacing |
| Pr | Prandtl number |
| $Q_{conv}$ | Convection term in data reduction equation |
| $Q_{cond}$ | Conduction term in data reduction equation |
| $Q_{gen}$ | Heat generation term in data reduction equation |
| $Q_{rad}$ | Radiation term in data reduction equation |
| $q''_w$ | Wall heat flux |
| $r_a$ | Leading edge radius of curvature of NACA 0012 airfoil |
| Re | Reynolds number |
| Rq | Roughness height root-mean-square |
| s | Surface direction along airfoil |
| S | Standard deviation |
| $S_E$ | Element diameter standard deviation |
| St | Stanton number |
| $T_\infty$ | Freestream temperature |
| $T_{IR}$ | IR camera temperature reading |
| $T_s$ | Surface temperature |

| | |
|---|---|
| $T_{SS}$ | Calibrated subsurface thermocouple temperature |
| $T_{UP}$ | Calibrated under plate thermocouple temperature |
| t | Student's t-value |
| $t_p$ | Plexiglas sub-plate thickness (0.72″) |
| u | Streamwise velocity |
| U | Uncertainty |
| $U_\infty$ | Freestream velocity |
| $U_{CI}$ | Cut in velocity (5 m/s) |
| $U_e$ | Local freestream velocity |
| $V_{eff}$ | Effective velocity measured by hot-film wire(s) |
| $V_{meas}$ | Measured velocity by Pitot-static probe |
| $V_N$ | Velocity normal to hot-film wire |
| $V_T$ | Velocity tangential to hot-film wire |
| $W_{ha}$ | Width of heated section |
| x | Streamwise location on plate |
| $x_{cr}$ | Critical distance for flow transition |
| $x_k$ | Sand-grain equivalent roughness height in LEWICE |
| $x_t$ | Transition location |
| w | Wall-normal velocity |
| z | Wall-normal distance from plate surface |

*Greek*

| | |
|---|---|
| $\alpha$ | Thermal diffusivity OR angle of wire of x-array probe |
| $\delta$ | Velocity boundary layer height |

| | |
|---|---|
| $\delta_T$ | Thermal boundary layer height |
| $\Delta t_s$ | Ice accretion time |
| $\Delta\theta$ | Change in momentum thickness |
| $\varepsilon$ | Emissivity (0.95) |
| $\zeta$ | Dummy variable representing $x$ in Stanton number correlations |
| $\kappa$ | Tangential velocity attenuation factor (0.115) |
| $\mu$ | Dynamic fluid viscosity |
| $\nu$ | Kinematic fluid viscosity |
| $\xi$ | Unheated starting length (1.7285″) |
| $\rho$ | Fluid density |
| $\rho_{ice}$ | Ice density |
| $\sigma$ | Stefan-Boltzmann constant (5.67E-8 $W/m^2K^4$) |
| $\tau_w$ | Wall shear stress |

*Subscripts*

| | |
|---|---|
| TC,cal | Thermocouple temperature measurement during calibration |
| TC,test | Thermocouple temperature measurement during test |
| IR,cal | Infrared temperature measurement during calibration |

*Abbreviations*

| | |
|---|---|
| IRT | Icing research tunnel |
| LWC | Liquid water content |
| MVD | Median volumetric diameter |
| RMH | Roughness maximum height |

# ACKNOWLEDGMENTS

I offer my sincerest thanks to Dr. Stephen McClain for serving as my mentor. His support, guidance, and enduring patience has proven invaluable throughout the duration of this project. I would also like to thank Dr. Joseph Kuehl and Dr. Yang Li for serving as members of my thesis committee. Their time and input have helped shape this work, and I am honored to have them on my committee.

I owe much thanks to my predecessors, Logan Tecson and Chris Walker, for their foundational work on this grant. Their efforts paved the way for a smooth transition in continuing the research goals of this grant. I would also like to thank Mr. Ashley Orr for his contributions in the development of the various apparatus used in this investigation. I would also like to thank my fellow graduate students Michael Hughes, Trae Liller, Blake Heller, Jake Christoph, Carl Reid, and Travis Watson for their assistance and comedic relief. Finally, I would like to thank my parents and grandparents. Their love and encouragement made this document possible.

The efforts reported in this work were supported as part of NASA Collaborative Agreement No. NNX12AB85A. The assistance and guidance of the members of the Icing Research Branch at NASA Glenn Research Center in Cleveland, OH is greatly appreciated. Any opinions presented in this work are those of the author and do not reflect the views of NASA or the United States government.

DEDICATION

To my family

# CHAPTER ONE

# Introduction

## *Motivation*

Aerodynamic performance losses associated with ice accretions on aircraft surfaces is a well-documented phenomenon. Ice accretions increase an aircraft's weight and experienced drag while simultaneously decreasing the amount of developed lift. Ice accretions have also been shown to reduce the experienced stall angle [1]. This degradation in overall aircraft performance can eventually lead to unstable flight resulting in accidents. According to the National Transportation Safety Board, airframe icing accidents led to 819 fatalities from 1982 to 2000 [2].

Given the inherent danger of operating an aircraft in icing conditions, it is ideal to avoid these conditions altogether. However, with the increasing density of air traffic it is not practical or even possible for pilots to do so. Therefore, all aircraft must be able to safely operate in icing conditions. This is achieved using anti-icing and de-icing techniques. Anti-icing techniques focus on preventing ice from accreting on aircraft surfaces, typically through the use of electric heaters or routing relatively warm air from the engine compressor section to aircraft surfaces. De-icing techniques focus on removing ice once it has accreted. This is often accomplished by spraying aircraft surfaces with propylene glycol or using pneumatic boots. However, many of these techniques can be classified as anti-icing or de-icing depending on when the technique is applied.

In the application of de-icing techniques in particular, it becomes necessary to predict how ice forms on aircraft surfaces. This is achieved through the use of ice accretion codes. LEWICE, the ice accretion code developed by NASA, is used throughout the aviation industry to help predict the size and shape of ice accretions so de-icing systems can be properly designed. An area for improvement in LEWICE is the characterization of convective enhancement caused by the initial layer of ice roughness that forms on aircraft surfaces [3]. The correlations used in LEWICE to predict convective enhancement are based on sand-grain equivalent roughness or ordered arrays of elements with regular and consistent geometries exposed to constant freestream flows. Real ice roughness on aircraft surfaces differ from the surfaces used for the correlations in LEWICE in many ways. Those differences include: 1) ice roughness occurs with random distributions of roughness elements of different size, 2) surfaces with ice roughness exhibit changing thermal boundary conditions due to variations in ice thickness along the surface of an airfoil, 3) ice roughness properties vary in the flow direction, and 4) surfaces with ice roughness experience accelerating flow because of the shape of the airfoil.

Different studies have isolated different aspects of realistic ice roughness in an attempt to improve upon the characterization of convective enhancement in LEWICE. Tecson [4] investigated the convective enhancement of realistic ice roughness surfaces with negligible freestream acceleration. Walker [5] expanded on the work of Tecson [4] by imposing varying thermal boundary conditions. However, the surfaces studied by Tecson [4] and Walker [5] exhibited an abrupt smooth-to-rough transition with constant roughness properties downstream of the transition. Recent investigations of ice roughness

on airfoils [6,7] demonstrate that the transition is not an abrupt change, and the roughness characteristics decay in the flow direction.

### *Objectives*

The objective of this investigation was to improve upon the work of Tecson [4] and Walker [5] by 1) including realistic ice roughness variations as measured using laser scanning and 2) including a flow acceleration profile along the flow direction. For this work, six surfaces and two flow conditions were investigated. Two smooth surfaces and four surfaces with realistic ice roughness distributions were tested. The smooth surfaces served as validation and comparison tools. Three of the rough surfaces represent the historical concept of ice roughness with an abrupt smooth-to-rough transition and with constant roughness properties downstream of the transition. The last rough surface represents a more contemporary treatment of ice roughness with a gradual smooth-to-rough transition and varying roughness properties in the flow direction. For each of the surfaces tested, heat transfer and velocity boundary layer measurements were performed with negligible flow acceleration and with an insert attached to the wind tunnel ceiling to replicate flow acceleration found on a NACA 0012 airfoil.

### *Presentation Outline*

Chapter Two provides a technical background in fluid mechanics, heat transfer, surface roughness, and aircraft icing. Chapter Three describes the development of the apparatuses and experimental methods used during this investigation. Chapter Four details the development of the data reduction equation for the convection measurements and the uncertainty associated with these measurements. Chapter Four also provides the

data reduction equations used for the velocity boundary layer measurements. Chapter Five presents and discusses the results of the convection and boundary layer measurements. Chapter Six draws conclusions based on the results and offers suggestions for future work.

# CHAPTER TWO

## Technical Background

### *Fluid Mechanics and Heat Transfer*

#### *Boundary Layers*

A velocity (or viscous) boundary layer is characterized as a thin region on the surface of a body in which viscous effects are very important, and outside of which the fluid behaves as if it were inviscid [8]. Figure 2.1 demonstrates how the velocity boundary layer will develop over a smooth flat plate. For a given streamwise location on the plate ($x$) the velocity inside the boundary layer ($u$) varies as a function of the vertical distance from the surface ($z$). The velocity boundary layer thickness ($\delta$) is the distance from the surface to a point where the flow velocity has essentially reached the freestream velocity ($U_\infty$). As shown in Figure 2.1, the boundary layer thickness is a function of $x$.

Figure 2.1 shows the different flow regimes during boundary layer development. The boundary layer begins to grow in the laminar region. In this region, fluid particles flow along well-ordered streamlines. The flow then transitions to the turbulent regime once the critical distance ($x_c$) is reached. The turbulent region is characterized by chaotic fluid motion. A viscous sublayer also begins to form near the surface in the turbulent region. Flow within the sublayer is regarded as laminar since turbulent fluctuations are suppressed by viscous effects. Outside of the viscous sublayer instantaneous velocity profiles at the same streamwise location exhibit fluctuations due to the chaotic nature of the flow. If these profiles are time averaged, the resulting profile ($\bar{u}$) appears nearly

uniform. Due to the irregular fluid motion in the turbulent region, the velocity gradients near the wall are larger compared to those in the laminar region.

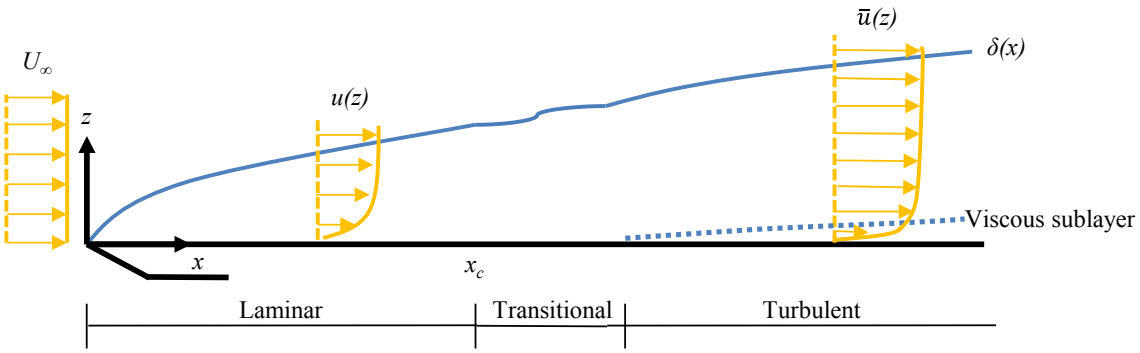


Figure 2.1: Velocity boundary layer development on a flat plate (not to scale)

The Reynolds number is a non-dimensional quantity that is used to characterize flow patterns in different fluids. That is, flows with similar Reynolds numbers are expected to behave similarly. The Reynolds number is defined as the ratio of inertial forces to viscous forces and thus helps quantify the relative importance of these forces for a given flow. For flow over a flat plate, the local Reynolds number is given by Eq. (2.1)

$$\mathrm{Re}_x = \frac{\rho U_\infty x}{\mu} \tag{2.1}$$

where $\rho$ is the fluid density, $\mu$ is the dynamic viscosity of the fluid, and $x$ is the surface distance from the leading edge of the plate. Flow over a smooth flat plate with a Reynolds number less than $5\text{x}10^5$ is considered laminar, and flow with a larger Reynolds number is considered turbulent [8].

A wall shear stress is incurred on surfaces as a result of fluid motion. For a Newtonian fluid the wall shear stress is given by Eq. (2.2).

$$\tau_w = \mu \left.\frac{\partial u}{\partial z}\right|_{z=0} \tag{2.2}$$

The wall shear stress can be represented non-dimensionally by the skin friction coefficient which is given by Eq. (2.3).

$$c_f = \frac{\tau_w}{1/2\,\rho U_\infty^2} \tag{2.3}$$

The skin friction coefficient is important as it can directly compare the amount of skin friction drag different surfaces experience under similar flow conditions.

If a temperature difference exists between a moving fluid and a surface, a thermal boundary layer will develop that is similar to the velocity boundary layer. Figure 2.2 illustrates a thermal boundary layer on a flat plate where the surface temperature is greater than the fluid temperature ($T_s > T_\infty$). Similar to the velocity boundary layer at a given streamwise location, the temperature ($T$) inside the thermal boundary varies as a function of the vertical distance from the surface. The thermal boundary layer thickness ($\delta_T$) is the distance to a point where the temperature has essentially reached the freestream temperature ($T_\infty$).

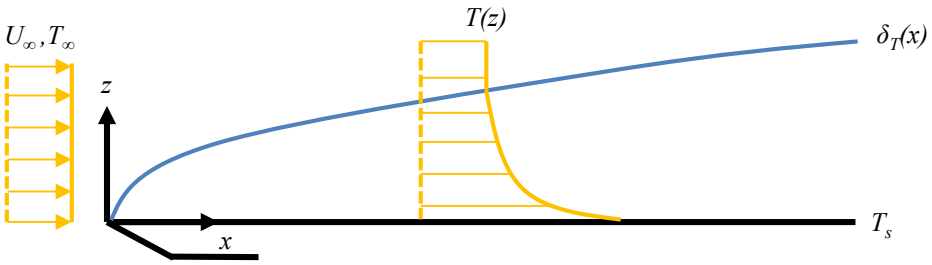


Figure 2.2: Thermal boundary layer on a flat plate

The Prandtl number is a non-dimensional quantity that is used to characterize the relative thickness of the velocity and thermal boundary layers, and it is defined as the

ratio of momentum diffusivity to thermal diffusivity of a fluid. The Prandtl number is given by Eq. (2.4)

$$\mathrm{Pr} = \frac{c_p \mu}{k_f} = \frac{\nu}{\alpha} = \frac{\delta}{\delta_T} \tag{2.4}$$

where $v$ is the kinematic viscosity of the fluid, $\alpha$ is the thermal diffusivity of the fluid, $c_p$ is the specific heat of the fluid, and $k_f$ is the thermal conductivity of the fluid. According to Eq. (2.4), a Prandtl number greater than one corresponds to a thicker velocity boundary layer compared to a thermal boundary layer, and a Prandtl number less than one corresponds to a thicker thermal boundary layer compared to a velocity boundary layer.

Similar to the wall shear stress associated with the velocity boundary layer, a heat flux is incurred on surfaces as result of the temperature gradient between the surface and fluid, as well as the bulk fluid motion. The surface heat flux is given by Eq. (2.5).

$$q''_w = -k_f \left.\frac{\partial T}{\partial z}\right|_{z=0} \tag{2.5}$$

The surface heat flux can also be represented non-dimensionally by the Stanton number which is given by Eq. (2.6)

$$\mathrm{St}_x = \frac{q''_w}{\rho U_\infty c_p \left(T_s - T_\infty\right)} = \frac{h}{\rho U_\infty c_p} \tag{2.6}$$

where $h$ is the convective heat transfer coefficient. Stanton numbers are often used to compare heat transfer values as they are independent of fluid type and flow condition, and because of their relationship to the skin friction coefficient for smooth surfaces via Reynolds' analogy. Reynolds' analogy relates these parameters by assuming that heat transfer (represented by the wall heat flux) and momentum transfer (represented by the

wall shear stress) are analogous processes. Accordingly, the Stanton number and skin friction coefficient are analogous parameters.

The theoretical Stanton number correlations for laminar and turbulent flow over a smooth flat plate with a constant heat flux boundary condition following an unheated starting length [9] are given by Eq. (2.7) and Eq. (2.8), respectively

$$\mathrm{St}_{x,\mathrm{laminar}} = \left[1-(\xi/x)^{3/4}\right]^{-1/3} 0.453\,\mathrm{Re}_x^{-1/2}\,\mathrm{Pr}^{-2/3} \tag{2.7}$$

$$\mathrm{St}_{x,\mathrm{turbulent}} = \left[1-(\xi/x)^{9/10}\right]^{-1/9} 0.0308\,\mathrm{Re}_x^{-1/5}\,\mathrm{Pr}^{-2/3} \tag{2.8}$$

where $\xi$ is the unheated starting length. These correlations include a correction for an unheated starting length since heat transfer will not occur in regions where a temperature gradient does not exist.

While the correlations given in Eq. (2.7) and (2.8) provide valuable insight to how the Stanton number varies along a smooth flat plate, they are not applicable to scenarios when the flow is subjected to freestream acceleration, such as over an airfoil. For accelerated flows in this investigation, the theoretical laminar Stanton numbers used were based on the correction of Smith and Spaulding [10] applied to the flat plate correlation of Eq. (2.7).

$$\mathrm{St}_{x,\mathrm{laminar}} = \left[1-(\xi/x)^{3/4}\right]^{-1/3} \frac{0.453\,\mathrm{Re}_x^{-1/2}\,\mathrm{Pr}^{-2/3}}{\left[\int_0^{\zeta}\left(\frac{U_e(\zeta)}{U_e(x)}\right)^{b-1}\frac{d\zeta}{x}\right]^{\frac{1}{2}}} \tag{2.9}$$

Where $\zeta$ is a dummy integration variable representing $x$, $U_e$ is local freestream velocity, and $b = 2.95\,\mathrm{Pr}^{0.07}$. The theoretical turbulent Stanton numbers were based on the correction of Ambrok [11] applied to the flat plate correlation of Eq. (2.8).

$$\mathrm{St}_{x,\mathrm{turbulent}} = \left[1-(\xi/x)^{9/10}\right]^{-1/9} \frac{0.0308\,\mathrm{Re}_x^{-1/5}\,\mathrm{Pr}^{-2/3}}{\left[\int_0^{\zeta}\left(\frac{U_e(\zeta)}{U_e(x)}\right)\frac{d\zeta}{x}\right]^{\frac{1}{5}}} \tag{2.10}$$

Since the original integral boundary layer correlations of Smith and Spaulding and Ambrok were derived under the assumption of an isothermal surface, their extrapolation to constant flux situations with an unheated starting length is not founded on experimental data. Therefore, the application of the correlations of Smith and Spaulding and Ambrok with the unheated starting length corrections may represent an extrapolation of the available methods. However, the combined use of the methods represents the best available option for capturing the effects of both the constant flux boundary with an unheated starting and the variable freestream velocity.

*Airfoils*

As air flows around an airfoil, flow acceleration initially occurs over the top surface according to conservation of mass. That is, a decrease in flow area requires an increase in flow velocity. According to Bernoulli's equation, an increase in flow velocity (i.e. flow acceleration) corresponds to a decrease in pressure in the flow direction. This is known as a favorable pressure gradient. The pressure will eventually reach a minimum value and begin to increase in the flow direction. This is known as an adverse pressure gradient. Figure 2.3 shows a surface pressure distribution on an airfoil and regions of favorable and adverse pressure gradients.

Flow over an airfoil can eventually separate from the surface in the presence of an adverse pressure gradient. The increasing pressure in the flow direction causes a fluid momentum deficit across the surface. The separation point occurs when the velocity

gradient at the wall is zero. A region of flow reversal (wake region) develops on the surface after the separation point. Figure 2.4 illustrates the separation process.

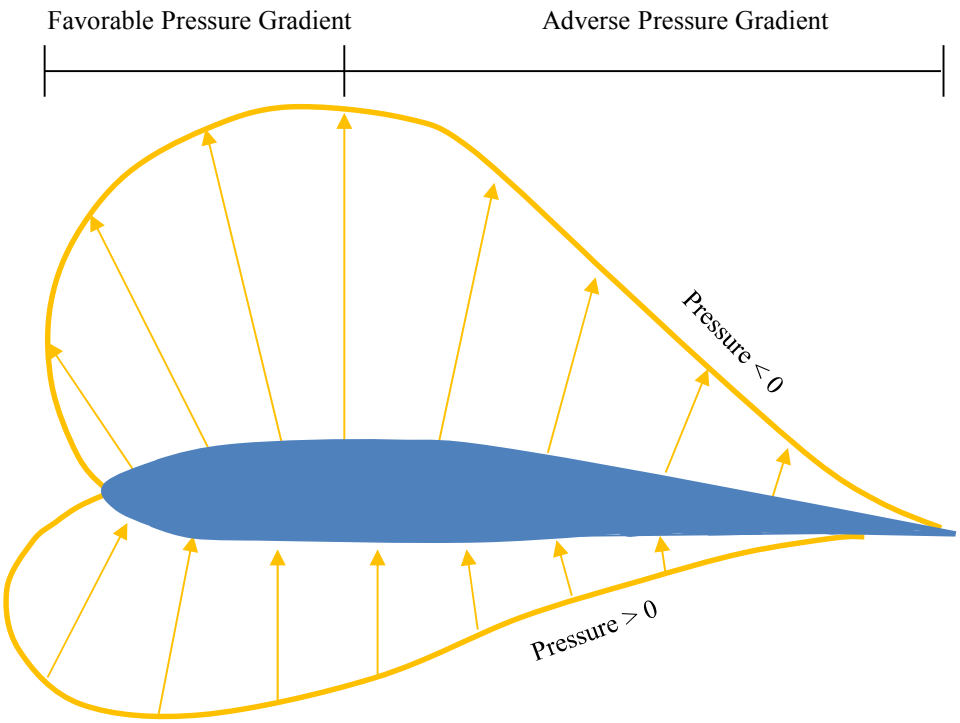


Figure 2.3: Surface pressure distribution on an airfoil

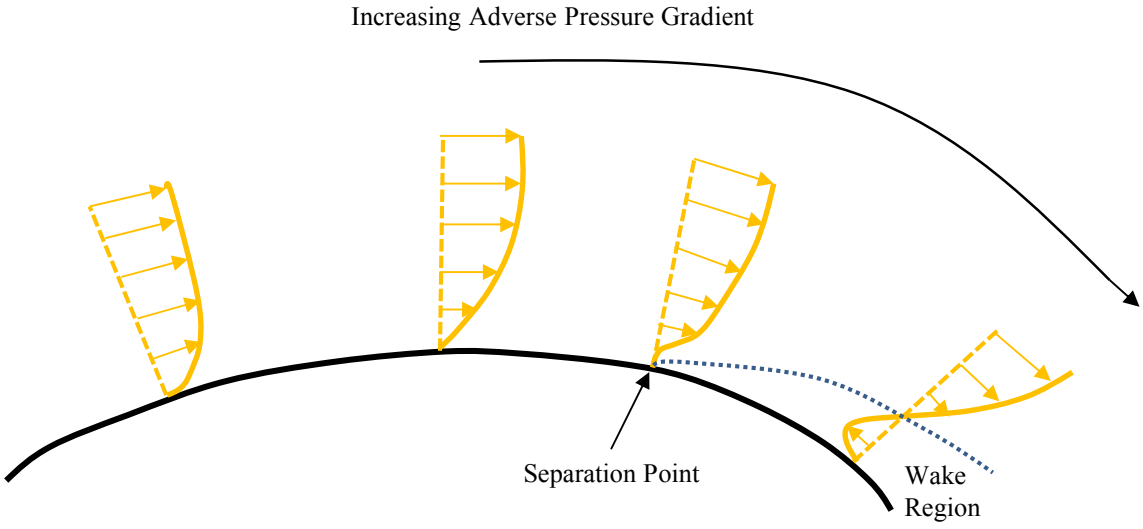


Figure 2.4: Flow separation process

The pressure distribution throughout a flow field is often represented non-dimensionally by the pressure coefficient which is given by Eq. (2.11)

$$C_p = \frac{p - p_\infty}{1/2\,\rho U_\infty^2} \tag{2.11}$$

where $p$ is the pressure at which the pressure coefficient is being evaluated and $p_\infty$ is the freestream pressure. The pressure coefficient is independent of Reynolds number which enables its use when designing scaled models. Applying Bernoulli's equation to Eq. (2.11), the local velocity in a flow field can be determined using Eq. (2.12).

$$U_e = U_\infty \left(1 - C_p\right)^{1/2} \tag{2.12}$$

Determining convective heat transfer coefficient data for complex surfaces, such as airfoils, is often difficult. While it is certainly possible to construct airfoil models, instrumenting these models with heat transfer equipment (thermocouples, heaters, etc.) adds complexity. This is only compounded if detailed surface maps are of interest since curved surfaces are not easily measured. Instead, it is easier to construct and instrument a flat plate with heat transfer equipment, and then construct a ceiling insert that matches the flow acceleration that occurs over the surface of an airfoil. Furthermore, heat transfer and fluid flow data is abundantly available for flat plates which allows for measurement comparison and validation.

*Surface Roughness*

Early experimental studies were performed by Nikuradse [12] and Schlichting [13] to characterize the effect surface roughness has on skin friction. Their results showed that skin friction is most affected by roughness in a turbulent boundary layer. This is

because roughness is likely to protrude through the viscous sublayer and produce complex flow fields that alter the wall shear stress [13].

A majority of the experimental work on roughness since has focused on determining skin friction and heat transfer enhancement using simulated roughness elements (hemispheres, cones, pyramids, etc.). Findings show the effect of roughness to be significant, with enhancements ranging from $1.5 < c_f / c_{f0} < 3.5$ and $1.1 < \mathrm{St}/\mathrm{St}_0 < 1.6$ [14]. In addition to these findings, multiple studies have been performed to quantify roughness enhancements corresponding to variable pressure gradients. Coleman et al. [15] created a surface with densely packed spheres and compared Stanton numbers at the same location for two flows: one at a constant freestream velocity and one at the same freestream velocity followed by an accelerated zone (favorable pressure gradient) prior to the measurement location. Their results indicated a 10-20% increase in the measured St (depending on Reynolds number) when comparing the accelerated flow condition to the constant freestream flow for the same roughness. Chakroun and Taylor [16] expanded on the studies of Coleman et al. by using hemispheres for the roughness elements as opposed to spheres. Results were similar to Coleman et al. with a 5-15% increase in the measured St (depending on Reynolds number) for an accelerated flow versus one with negligible freestream acceleration. Turner et al. [17] also performed a similar study involving an ordered array of pyramid shaped roughness elements and a favorable pressure gradient. Their results showed a 5% increase in the measured St versus a zero pressure gradient.

Based on the studies above, it is evident that a pressure gradient is an important parameter when considering heat transfer enhancement from rough surfaces. However, these studies employed systematic roughness distributions that are not characteristic of

real roughness. Bons and McClain [14] performed a study to determine the effect realistic roughness has on measured St. Realistic turbine roughness models (and one "simulated" roughness model for comparison) were tested at three different pressure gradients: adverse, zero, and favorable. In comparing the St enhancement relative to the zero pressure gradient, it was shown that the favorable pressure gradient increased St by 7% for the "simulated" roughness surface and increased St up to 18% for the realistic roughness model. This illustrates the importance of considering realistic roughness distributions in predicting heat transfer, as the "simulated" surface and realistic models behave dissimilarly under the influence of a favorable pressure gradient.

It is also important to consider the thermal conductivity of roughness elements when predicting heat transfer. Mart [18] tested two identical roughness distributions under similar heating and flow conditions; one surface was constructed with ABS plastic elements and the other with aluminum elements. The aluminum elements exhibited heat transfer values that were approximately 12% higher than the ABS elements.

There are several modeling approaches that are used to characterize the effects of surface roughness. One such model is the sand-grain equivalent roughness model that was developed by Schlichting [13]. This model relates the resistance of roughness being investigated to the size of sand grain in the experiments of Nikuradse [12] that give the same resistance. The sand-grain equivalent model is still used today as it can be adjusted to match skin friction values of realistic roughness surfaces. However, heat transfer from these surfaces is often poorly predicted using this model.

An alternative model to characterize the effects of surface roughness is the discrete element method (DEM), also proposed by Schlichting [13]. In this model the

total drag on a rough surface is the sum of the skin friction drag on the flat part of the surface and the form drag on individual roughness elements. By contrast to the sand-grain equivalent model, the DEM has proven effective in estimating heat transfer from realistic roughness surfaces. McClain et al. [19] suggested an improvement to the DEM with the extended surface discrete element method (ES-DEM). This model incorporates the heat transfer associated with temperature changes that occur along the height of the roughness elements.

Another method used to characterize the effects of roughness is through grid-resolved computational simulations. Upon model validation, this approach can be utilized to determine roughness effects for a wide range of parameters, thus reducing the cost associated with experimentation. However, an enormous amount of grid points or cells are needed to resolve complex roughness geometries; this can prove a challenge in terms of computation time and memory requirements. Bons et al. [20] showed that grid-resolved simulations can yield better agreement with experimental results compared to DEM, but come with a 2-3 order of magnitude increase in computational time.

## *Aircraft Icing*

### *Common Icing Terms*

There are several icing related parameters that are influential in the formation and evolution of ice accretions. These parameters include the liquid water content and median volumetric diameter. Liquid water content (LWC) is the amount of liquid water (mass) per unit volume of air. Median volumetric diameter (MVD) is the drop diameter that divides the total liquid water content in the drop distribution in half. Half of the water

volume will be in larger drops and half in smaller drops [21]. For example, in a cloud with an MVD of 10 μm, half of the water volume is contained in droplets having a diameter greater than 10 μm and the other half of the water volume is contained in droplets having a diameter less than 10 μm. The MVD is the most commonly used parameter when describing the size of droplets in icing conditions.

Together, the LWC and MVD help define a set of atmospheric icing conditions in which aircraft must be able to safely operate. The most well-known characterization of these conditions is known as Appendix C conditions [22]. Appendix C conditions are characterized as having supercooled or partially frozen droplets with an MVD of 1-50 μm and represent what is commonly known as "freezing drizzle." In the past, Appendix C conditions were the primary focus of ice protection system certification for small or business class aircraft. However, recent legislation has made Appendix O conditions [23] the new focus of ice protection system certification. Appendix O conditions, also known as supercooled large droplet (SLD) conditions, are characterized as having supercooled or partially frozen droplets with an MVD of > 50 μm and represent what is commonly known as "freezing rain."

The formation and evolution of ice accretions is also influenced by the icing regime. There are two main icing regimes: rime icing and glaze icing. In rime icing, 100% of the impinging water droplets freezing on impact. This regime typically occurs at freestream temperatures well below freezing (0ºF), and it is characterized by white opaque ice accretions. In glaze icing, less than 100% of the impinging water droplets freeze on impact, which leads to a layer of liquid water runback. This regime occurs at

freestream temperature close to freezing (32ºF), and it is characterized by clear ice accretions.

*Ice Accretion Process*

One of the first studies to capture the icing process was performed by Olsen and Walker [24]. A high speed camera was used to record the accretion process on an airfoil mounted in the test section of the Icing Research Tunnel (IRT) at the NASA Glenn Research Center. They were able to observe that as supercooled water droplets impinge on an airfoil they begin to coalesce and grow. If these droplets grow large enough, the aerodynamic drag on the droplets overcome the surface tension forces that keep the droplets stationary and allow them to move downstream along the airfoil surface. The droplets continue to move aft until they freeze, causing an initial layer of surface roughness. For a symmetric airfoil at zero angle of attack, this results in a symmetric smooth-zone about the stagnation region, shown in Figure 2.5.

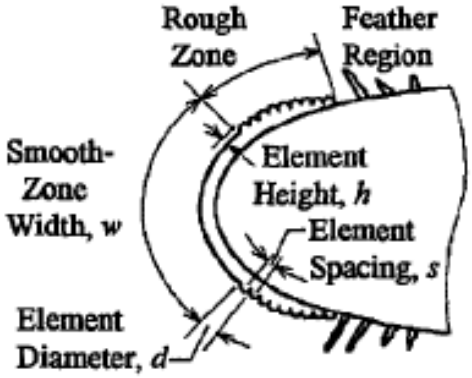


Figure 2.5: Early stage ice accretion on airfoil leading edge [25]

*Ice Accretion Modeling*

In 1953, Messinger [26] developed the foundational model for aircraft icing. This model performs an energy balance at an unheated surface in icing conditions. Energy losses are considered from convection, evaporation/sublimation (depending on the equilibrium surface temperature), and sensible cooling by the impinging water droplets. Energy gains are considered from the latent heat of fusion, viscous heating in the boundary layer, and the kinetic energy of the impinging water droplets. Figure 2.6 demonstrates the various modes of energy transfer for an unheated airfoil in icing conditions. Although several modes of heat transfer exist on an airfoil, the prediction of ice growth rates and ice shape formation is highly sensitive to convection since it is the predominant mode of heat transfer in aircraft icing [27].

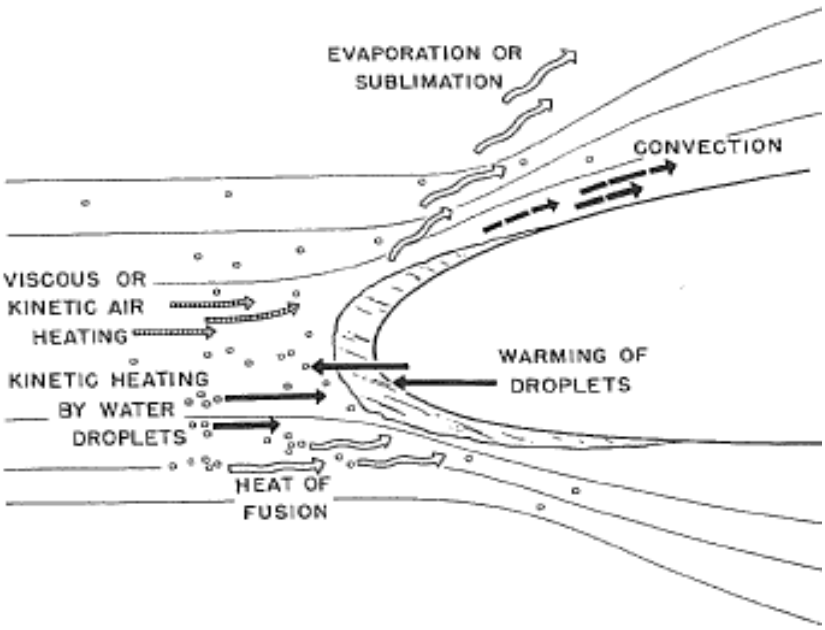


Figure 2.6: Modes of energy transfer for an unheated airfoil in icing conditions [26]

Messinger [26] also developed the freezing fraction. The freezing fraction is a non-dimensional parameter defined as the ratio of impinging water droplets that freeze to the total number of impinging water droplets. The value of the freezing fraction is limited between zero and one. When the freezing fraction is equal to one, all of the impinging water droplets freeze on impact (i.e. rime icing). As its value decreases, fewer droplets freeze on impact leading to water runback along the surface of the airfoil (i.e. glaze icing).

Despite its age the Messinger model remains relevant today as a form of it is used in NASA's Lewis Ice Accretion Code, or simply LEWICE. In LEWICE the ice roughness heights are estimated based on the sand-grain equivalent roughness model [28]. The equivalent sand-grain roughness height is determined using Eq. (2.13)

$$x_k = \frac{1}{2}\sqrt{0.15 + \frac{0.3}{N_{f,stag}}} \tag{2.13}$$

where $N_{f,stag}$ is the freezing fraction at the stagnation point. Its value is calculated separately. Convective heat transfer coefficients are then calculated using a semi-empirical method based on the turbulent momentum thickness and the equivalent sand-grain roughness height. These results can then be applied to the modified Messinger model to determine the local energy available for freezing the available water.

This handling of ice roughness is often criticized since sand-grain roughness differs from realistic ice roughness in both size and distribution density [29]. Furthermore, it has been shown that ordered arrays of roughness elements with regular and consistent geometries do not provide an accurate model for estimating heat transfer [14,30]. Also, the use of one parameter ( $N_{f,stag}$ ) to predict ice roughness heights over a

wide range of icing conditions is very simplistic. Shin [29] performed a study that compared measured ice roughness heights on an airfoil in the IRT to the LEWICE predicted sand-grain roughness heights with matched icing conditions. His results showed that LEWICE poorly predicted trends and magnitudes of roughness height when varying icing parameters (e.g. LWC, temperature, airspeed). Figure 2.7 shows a comparison of the measured roughness height and the predicted sand-grain roughness height as a function of LWC.

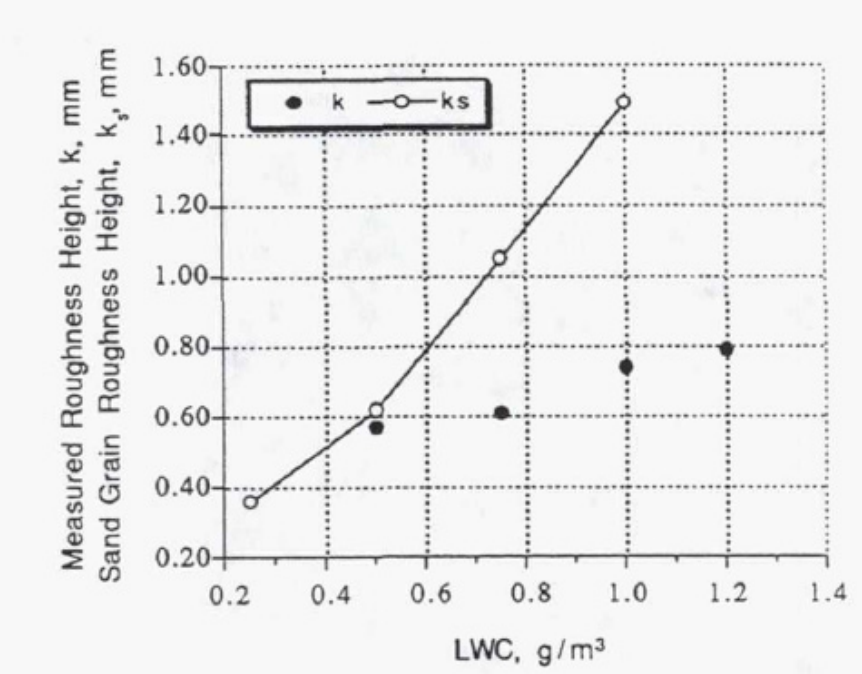


Figure 2.7: Comparison of measured roughness height with the predicted sand-grain roughness height [29]

*Ice Roughness Investigations*

Numerous studies have been performed to help characterize the effects initial ice roughness has on the development of ice accretions. Poinsatte et al. [31] sought to determine the effect roughness has on convective heat transfer on an airfoil.

Hemispherical roughness elements of uniform diameter were placed on the surface of a 21" chord NACA 0012 airfoil in different ordered patterns; two of these roughness patterns are shown in Figure 2.8. As expected, the addition of the roughness elements to the NACA 0012 airfoil drastically increased the measured heat transfer compared to the smooth airfoil. Additionally, their results showed that increasing the roughness distribution density increased heat transfer up to 54% relative to the sparsely placed roughness elements.

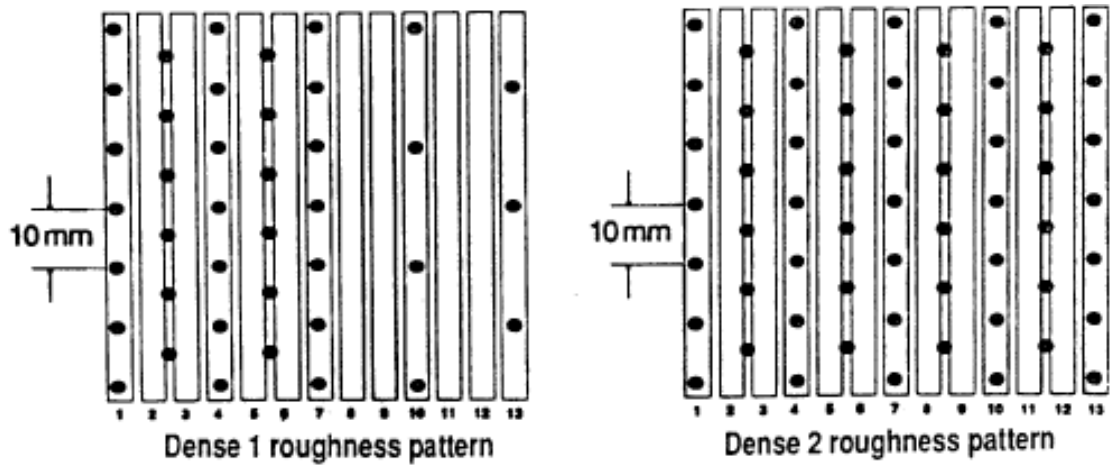


Figure 2.8: Ordered roughness distributions used by Poinsatte et al. [31]

Bragg et al. [32] performed a similar study using an ordered array of uniform diameter roughness elements on the surface of a 21" chord NACA 0012 airfoil, but focused on the smooth-to-rough boundary transition. In addition, the freestream turbulence intensity was varied to determine its effect on convective heat transfer enhancement. Results showed that a change in turbulence intensity had little to no effect on heat transfer enhancement in the leading 20-40% of the airfoil (based on Reynolds number). However, aft of this location the heat transfer enhancements corresponding to the elevated freestream turbulence cases exhibited a drop off in magnitude. This result

was attributed to the unperturbed boundary layer of the elevated turbulence cases transitioning earlier. The measured enhancements are shown in Figure 2.9. Although these studies [31,32] were performed on a real airfoil, they used a simplistic roughness model that is not characteristic of realistic ice roughness distributions.

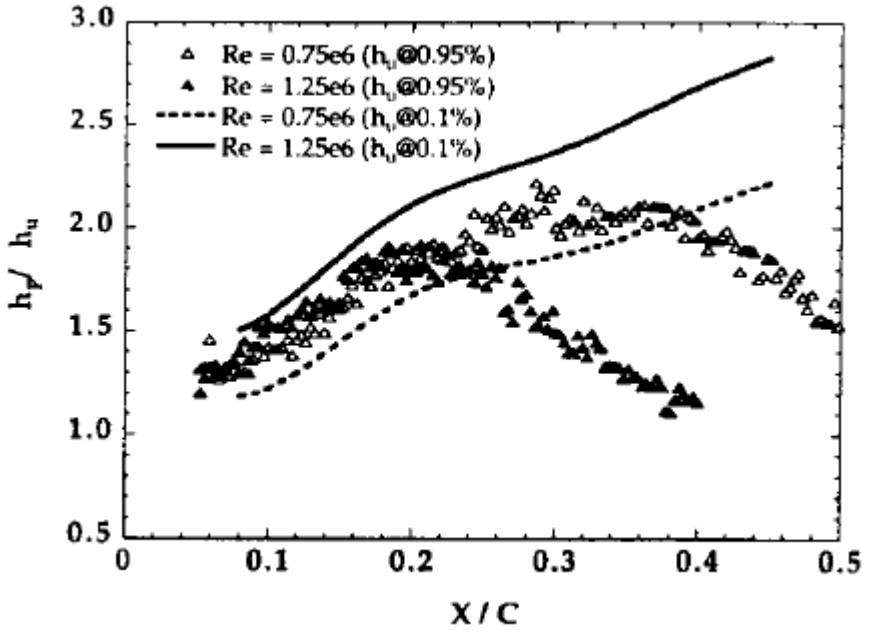


Figure 2.9: Heat transfer enhancement with varying freestream turbulence [32]

Dunkan et al. [27] improved upon the works of Poinsatte et al. [31] and Bragg et al. [32] by using realistic ice roughness distributions on the surface of an airfoil. A casting technique was used to manufacture testable models of iced NACA 0012 airfoils from the IRT. One of these models is shown in Figure 2.10. The models were instrumented with heat-flux gauges and heaters to measure local convective heat transfer coefficients. Compared to Poinsatte et al. [31] they observed much higher values of heat transfer. Their results underscore the importance of using realistic ice roughness distributions when determining heat transfer rates from ice roughness, as ordered arrays

of roughness elements often underestimate these values. Han and Palacios [33] performed a similar investigation involving casted NACA 0012 airfoils with naturally accreted ice roughness. Their experimental measurements of ice roughness height and heat transfer were compared with LEWICE predictions to quantify any differences. It was shown that LEWICE significantly over-predicted the maximum heat transfer values by 200-391%.

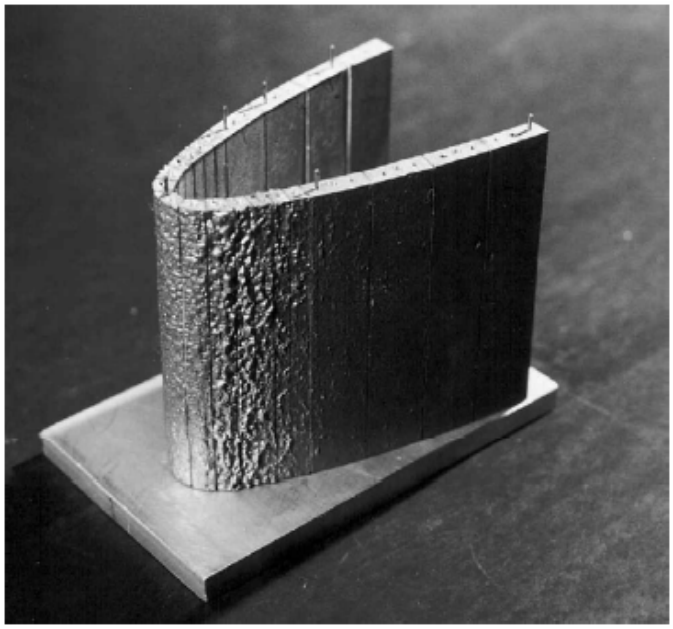

Figure 2.10: Casting of ice roughness on a NACA 0012 airfoil [27]

Anderson et al. [34] and Shin [29] performed studies that measured roughness parameters for ice roughness distributions on a NACA 0012 airfoil subjected to Appendix C conditions. The IRT was used to create ice roughness on the NACA 0012 airfoil and images were taken of the resulting accretions. Using image analysis approaches, Anderson et al. [34] reported a statistical and morphological description of the roughness elements which included the mean roughness element diameter, the standard deviation of the roughness element diameters, and the smooth zone width. The investigations

performed by Anderson et al. [34] and Shin [29] were important as they provided a complete description of ice roughness parameters corresponding to Appendix C conditions.

Tecson and McClain [35] investigated the enhancement of surfaces with roughness distributions similar to those found on airfoils with ice roughness. These surfaces were created using a Lagrangian droplet simulation of the beading and coalescence process [36]. The resulting bead pattern was modified to match the characteristics of surfaces measured from previous studies in the IRT [29,34]. A solid model of one of these surfaces is shown in Figure 2.11. The investigation of Tecson and McClain [35,36] provided an alternative method to casting for measuring heat transfer enhancement from realistic ice roughness surfaces.

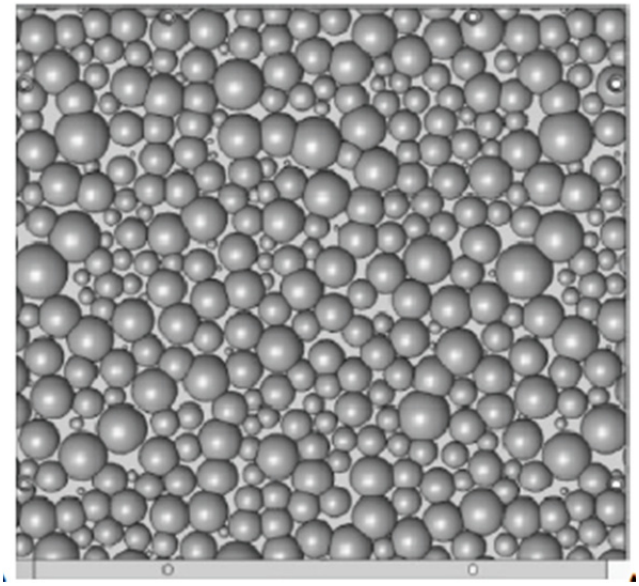

Figure 2.11: Solid model of realistic ice roughness surface [36]

Walker et al. [37] expanded on the study of Tecson and McClain [35,36] by imposing different flux boundary conditions. Walker et al. [37] found that although the

different boundary conditions produced slight variations in the measured heat transfer, shown in Figure 2.12, the relative enhancement above the smooth turbulent case was not significant for a given roughness pattern. Furthermore, the varying thermal boundary conditions did not replicate the differences between LEWICE predictions and experimental heat transfer measurements.

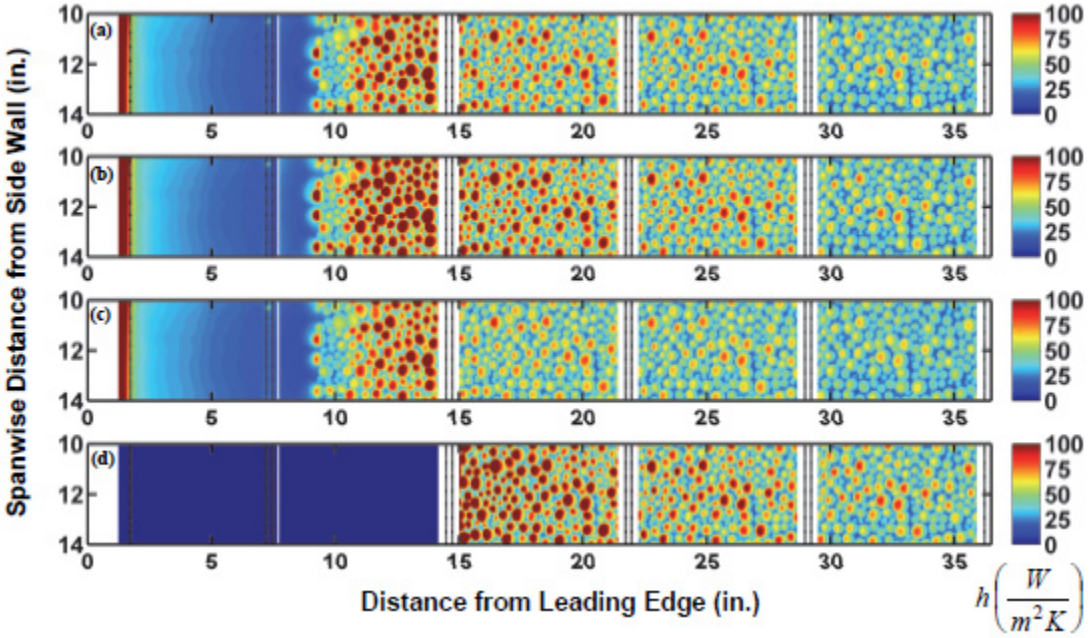


Figure 2.12: Convective heat transfer coefficient contour maps for varying thermal boundary conditions [37]

McClain et al. [6] performed a study that measured the variation in roughness height along the surface of an iced NACA 0012 airfoil in Appendix O conditions. Their results demonstrated that the smooth-to-rough transition does not occur abruptly, and the roughness characteristics decay in the flow direction downstream of the location where the maximum roughness height occurs. This was a significant observation as historical investigations of roughness on iced airfoils were characterized by an abrupt step change in the smooth-to-rough region, and constant roughness properties downstream of the

transition [29,34]. Figure 2.13 demonstrates the variations in roughness height along the airfoil surface for different Appendix O conditions.

The objective of this work is to expand on the investigations of Tecson and McClain [35,36] and Walker et al. [37] by 1) including realistic ice roughness variations as measured in the IRT using laser scanning and 2) matching the flow acceleration along the leading edge of a NACA 0012 airfoil. Heat transfer enhancements can then be measured to help provide a deeper validation database for icing convection methods, as well as continue to attempt to isolate the cause of increased heat transfer rates predicted by LEWICE.

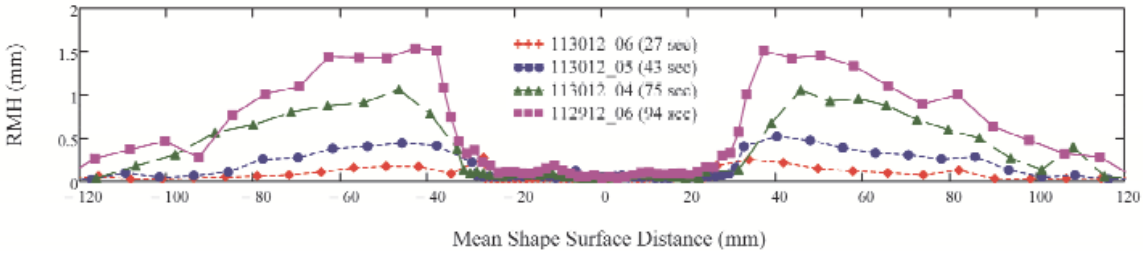


Figure 2.13: Roughness height measurements in Appendix O conditions [6]

# CHAPTER THREE

## Materials and Methodology

A series of experiments were performed to characterize the convective heat transfer from realistic ice roughness surfaces in the presence of a pressure gradient. In order to perform these experiments, several apparatuses were designed and constructed. This chapter describes the design and construction of these apparatuses, as well as the experimental setup and procedures.

### *Instrumented Test Plate*

The test plate was designed to model the leading 17.1% (3.6") region immediately downstream of the stagnation point of the 21" chord NACA 0012 airfoil used in the experiments of Anderson et al. [34]. A geometric scaling of 10x was applied to the surface distance from the leading edge and to the roughness dimensions. Consequently, the test velocity used is reduced by a factor of 10 in order to match the Reynolds number of the airfoil. The scaling and focus on the leading 17.1% of the airfoil are appropriate since the majority of ice roughness formation occurs near the stagnation region of the airfoil.

The construction of the test plate was performed by Tecson [4]. Enough information will be provided for a rudimentary understanding of its creation. For a more complete and thorough account, refer to Tecson [4]. A solid model of the test plate is shown in Figure 3.1. The test plate was designed to accommodate 25 interchangeable surface panels. This design feature has the benefit of eliminating the need to construct a

test plate for each surface that is tested. In total, six different surfaces were created, manufactured, and tested. The test plate can be broken down into the following subsystems which will be discussed in greater detail:

1. Plexiglas sub-plate
2. Instrumentation and wiring
3. Mylar film heaters
4. Aerodynamic features

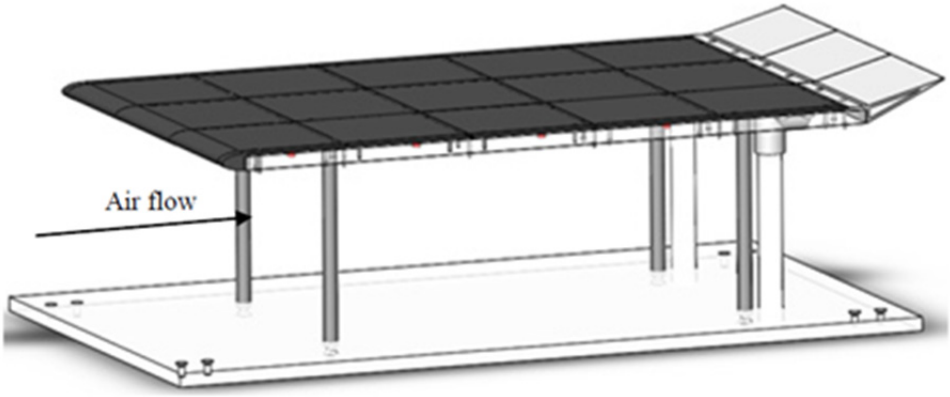


Figure 3.1: Solid model of test plate [4]

*Plexiglas Sub-Plate*

The base of the test plate was constructed using a 24" x 36" x 0.75" Plexiglas plate. A router with a 1/2" diameter straight bit was used to machine channels to a depth of 0.035" for the placement of copper electrodes. This depth was chosen to allow the electrodes to remain flush with the surface of the Plexiglas plate. A 1/8" diameter straight bit was used to machine additional channels to a depth of 1/8" on the top surface of the plate for the placement of thermocouples. A through-hole was drilled at the off-center end of each of the thermocouple channels to allow the wires to exit. An additional 52

through-holes were drilled using a drill press. These holes, in combination with #4 1.25" long bolts and #4 nuts, are used to affix the 25 surfaces panels to the test plate. Four 0.75" diameter steel legs were used to affix the Plexiglas sub-plate to the wind tunnel floor. Figure 3.2 shows the Plexiglas sub-plate after machining.

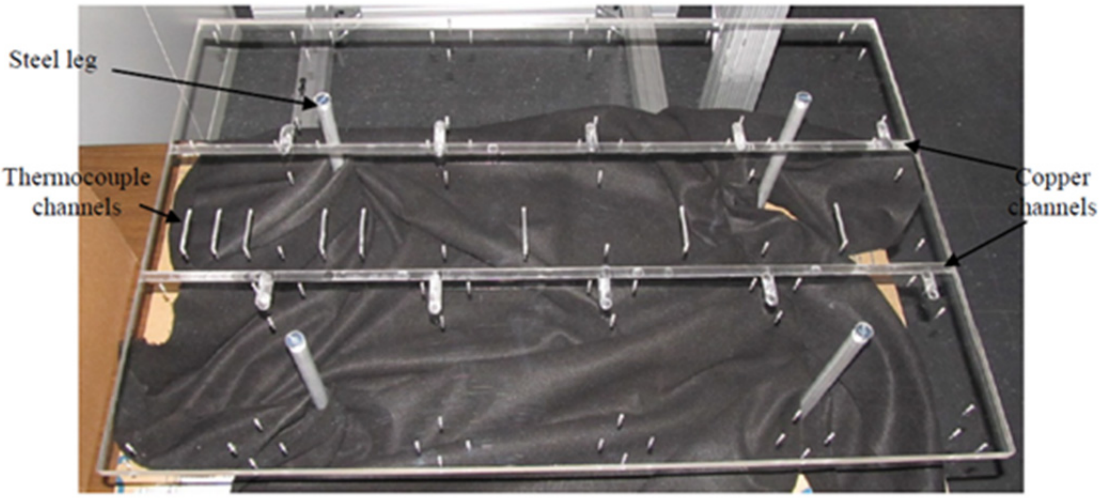


Figure 3.2: Plexiglas sub-plate [4]

*Instrumentation and Wiring*

Eight Type K thermocouples were placed in the thermocouple channels shown in Figure 3.2. The thermocouple beads were positioned at the centerline of the test plate 1/16" beneath the Plexiglas surface in the center of each of the five heated sections, and the remaining thermocouple wire was routed through holes in each channel. Two additional thermocouples were added to the first section (closest to the leading edge) and one additional thermocouple was added to the second section to characterize any heat loss gradients in the streamwise direction. The thermocouples were then imbedded in the channels using a plastic epoxy. Additionally, eight self-adhesive Type K thermocouples were affixed on the bottom of the test plate directly below the thermocouple channels.

Together, the eight thermocouple pairs account for the heat loss through the bottom of the test plate. Figure 3.3 shows the location of the thermocouple pairs. The surface distance from each thermocouple to the leading edge of the plate can be evaluated by adding 1.7285" to the reported dimensions. The thermocouple pairs were numbered according to the heated sections, with letters used to distinguish thermocouples in sections with multiple pairs.

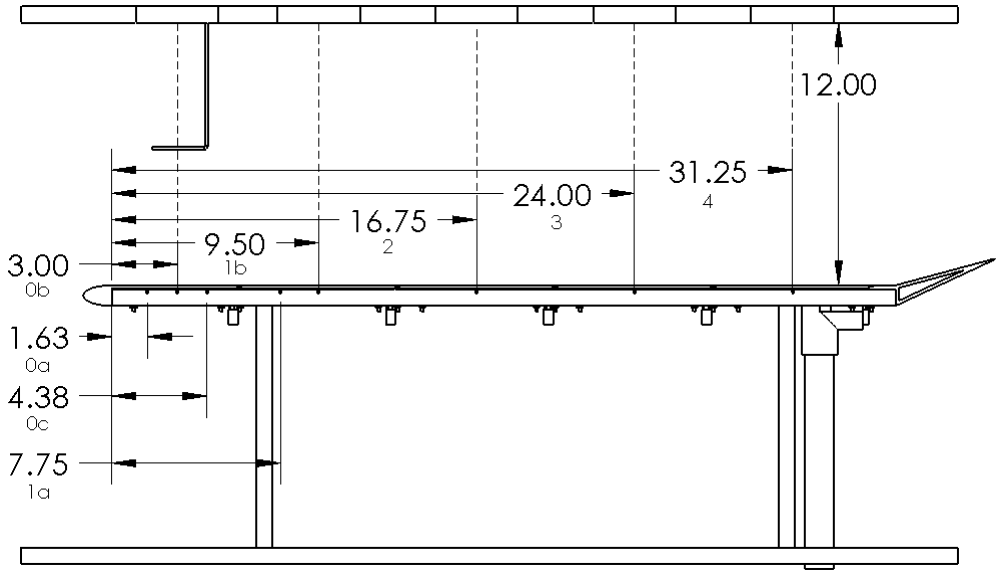


Figure 3.3: Side view of test plate showing thermocouple placement from the leading edge of the Plexiglas sub-plate (dimensions in inches, flow is from left to right) [4]

Fourteen gauge copper wire was connected to terminal posts on each of the copper electrodes to supply power to the Mylar film heaters. Additionally, twenty-two gauge copper wire was connected to the bottom of each terminal post in order to measure the voltage across each heater. The wires were bound and routed on the bottom of the Plexiglas sub-plate to the electrical junction box. The electrical junction box consists of 3D printed elbows that connect to two 1" schedule 40 PVC pipes that run from the underside of the Plexiglas sub-plate through the wind tunnel floor to allow access to the

wires outside of the test section. Figure 3.4 illustrates the location of the electrical junction box and terminal posts on the bottom of the Plexiglas sub-plate.

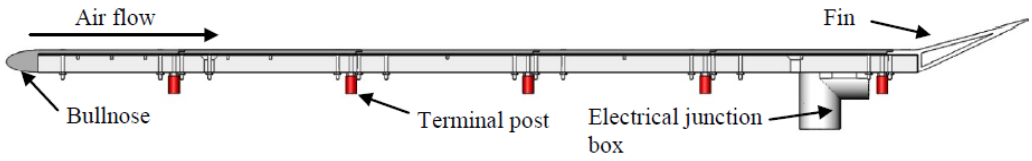


Figure 3.4: Side view of test plate [4]

*Mylar Film Heaters*

Five separate gold-deposited Mylar film heaters were used to provide a nominally constant flux boundary condition for each of the heated sections. Each heater spanned the distance between the copper electrodes affixed in the Plexiglas sub-plate. In order to minimize the contact resistance between the electrodes and the heater, conductive silver paint was applied at their interface. The shaded regions in Figure 3.5 denote the location of the Mylar film heaters in the Plexiglas sub-plate, and the designation of the heated sections. Figure 3.5 also demonstrates that there are 0.25" gaps between the Mylar film heaters to allow screws to pass through the lap joints of the surface panels.

Great care was taken during the installation of the Mylar film heaters. Latex gloves were worn throughout the process to ensure that skin oils and other contaminates did not come into contact with the gold layer, as this could result in uneven heating. The Mylar film heaters were cut to specification and attached to the Plexiglas sub-plate, gold side down, using 3M Super 77 spray adhesive. A rubber brayer was used remove excess adhesive and air bubbles between the Mylar film heaters and the Plexiglas sub-plate. This was done in an effort to prevent the heaters from delaminating and creating uneven

heating. Figure 3.6 illustrates the Mylar film heaters installed in the second and third heated sections.

*Aerodynamic Features.*

The test plate was designed with two important aerodynamic features, a bullnose at the leading edge and a fin at the trailing edge. The purpose of the bullnose was to prevent flow separation at the leading edge. The purpose of the fin was to account for the blockage on the underside of the test plate caused by the instrumentation and prevent preferential flow migration to the top side of the plate. The fin was designed to have a frontal area approximately equal to the area of the blockage underneath the plate caused by the PVC pipes, test plate legs, and the electrical connectors. The bullnose and tail fin are shown in Figure 3.4.

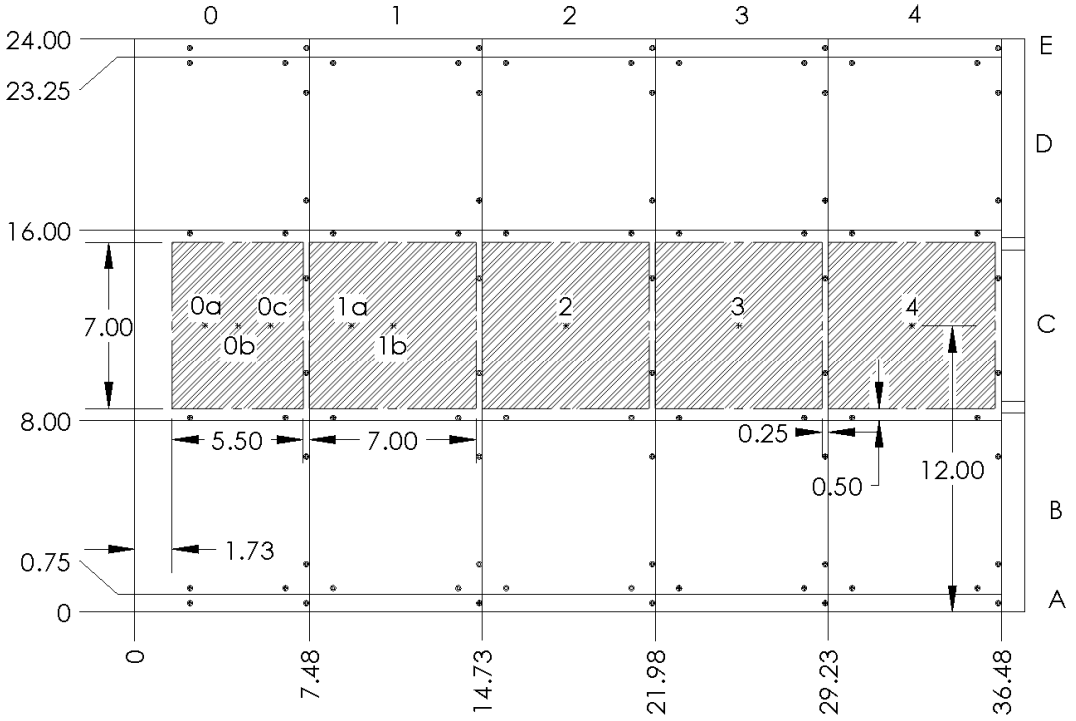


Figure 3.5: Layout of the heated sections on the Plexiglas sub-plate (dimensions in inches, flow is from left to right) [4]

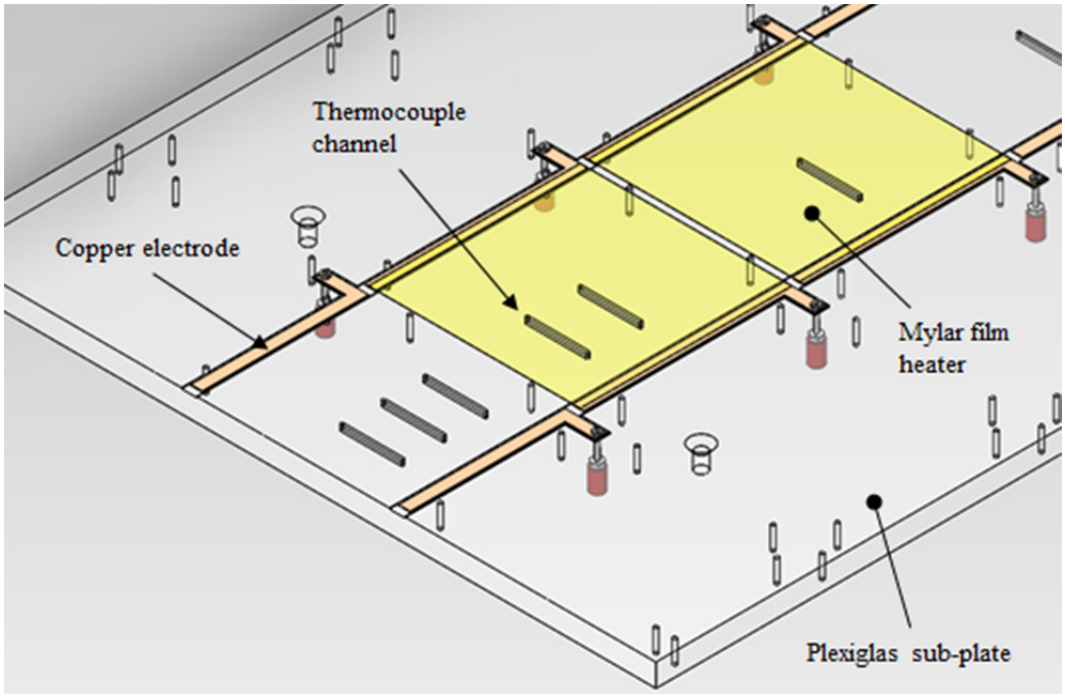


Figure 3.6: Isometric view of test plate with Mylar film heaters installed in the second and third heated sections [4]

## *Realistic Ice Roughness Surfaces*

### *Implementing Lagrangian Droplet Simulator*

A Lagrangian droplet simulator was developed by Tecson and McClain [36] to create realistic ice roughness distributions. This was accomplished by modeling how ice roughness forms on a surface; that is, the simulator models the impingement and coalescence of droplets. The required simulator inputs are 1) the simulation area, 2) the diameter of the impinging droplets, 3) the contact angle of the impinging droplets relative to the surface, and 4) the total number of droplets to impinge. The simulator performs the algorithm represented by the flow chart in Figure 3.7. Once the simulation was completed, a data file was generated that contained the final location (x and y position) and diameter of each droplet.

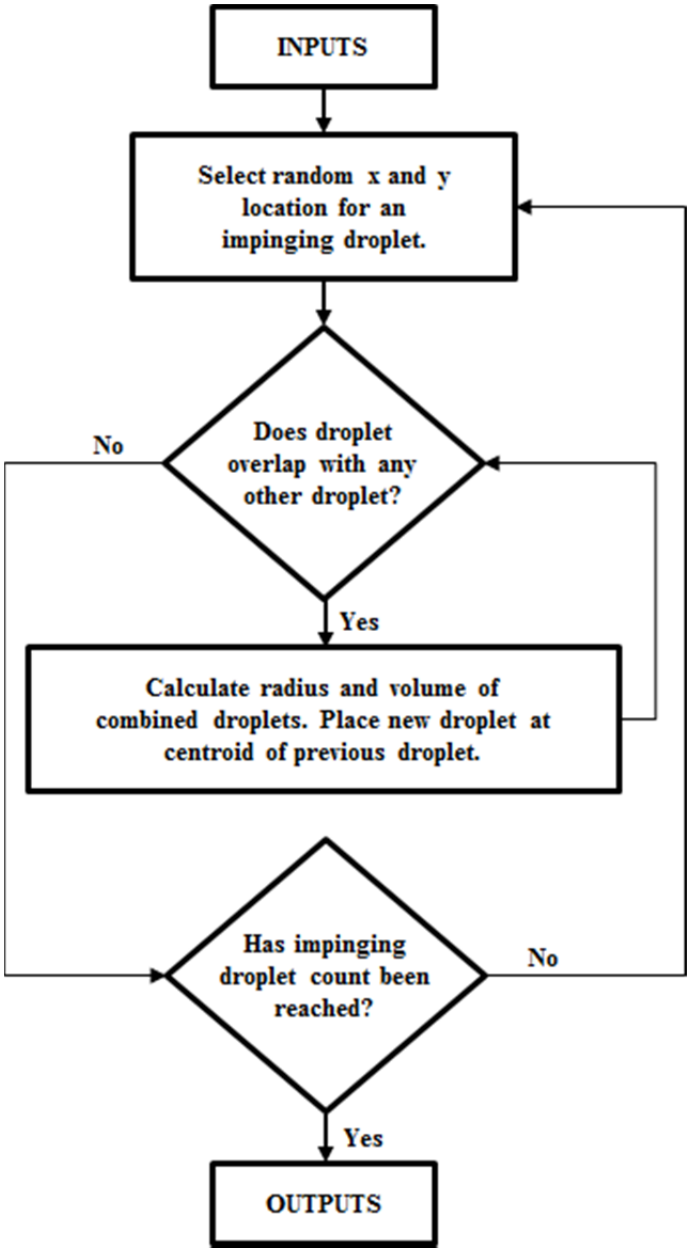


Figure 3.7: Flow chart of algorithm used in the Lagrangian droplet simulator

*Matching Roughness Parameters*

For this study, four realistic ice roughness surfaces were created. Three of these surfaces were created using the historical description of an “Appendix C” roughness on a 21" chord NACA 0012 airfoil. The other roughness surface was created by matching the variation in roughness characteristics, measured using laser scanning, on a 21" chord

NACA 0012 airfoil in SLD conditions. The creation of these two distinct surface types will be discussed independently.

*Historical ice roughness.* Three realistic ice roughness distributions were created using the ice roughness data reported by Anderson et al. [34] and Shin [29]. The data collected by Shin [29] was only used in determining roughness elements spacing-to-diameter values, which are not reported by Anderson et al. [34]. The airflow and cloud characteristics used to generate the ice roughness data used in this investigation are reported in Table 3.1. In Table 3.1, the run identifiers 052996.04 and 053096.01 correspond to the historical description of ice roughness. Also in Table 3.1, $A_c$ is the accumulation parameter and is defined by Eq. (3.1), where $r_a$ is the leading-edge radius of curvature of the NACA 0012 airfoil, and $\rho_{ice}$ is the density of ice at the freestream temperature.

$$A_c = \frac{LWC \cdot V \cdot \Delta t_s}{2 \cdot r_a \cdot \rho_{ice}} \tag{3.1}$$

Images were taken of the resulting ice accretions and are shown in Figure 3.8.

Table 3.1: Cases used to generate roughness data

| Run Identifier | T (°C) | V (m/s) | MVD (μm) | LWC ($gm/m^3$) | $\Delta t_s$ (s) | $A_c$ | Freezing Fraction |
|---|---|---|---|---|---|---|---|
| 052996.04 [34] | -4.2 | 66.7 | 29.7 | 0.6 | 94 | 0.245 | 0.217 |
| 053096.01 [34] | -5.6 | 67.1 | 29.9 | 1.0 | 14 | 0.061 | 0.216 |
| 113012.04 [6] | -2.4 | 66.7 | 150.0 | 0.6 | 75 | 0.195 | 0.217 |

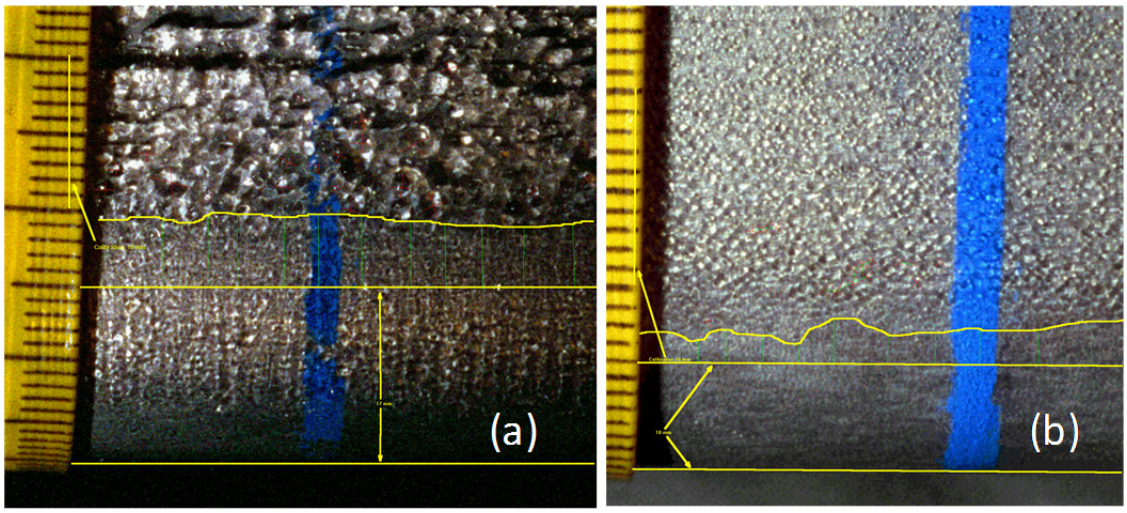


Figure 3.8: Ice accretion images for run identifiers a) 052996.04 and b) 053096.01 from Anderson et al. [34]

The Lagrangian droplet simulator was used to match the roughness parameters reported by Anderson et al. [34]. However, it was observed that the generated distributions from the simulator differed from the reported data in the following ways: 1) overall average element diameter, 2) diameter standard deviation, and 3) element spacing-to-diameter values. To resolve these inconsistencies, a series of data conditioning procedures were applied to the simulator data. Roughness elements with small diameters were truncated, the roughness elements were stretched, and the roughness elements were scaled to match the roughness parameters observed by Anderson et al. [34]. For a more thorough account of the data conditioning procedures, refer to Tecson [4]. Figure 3.9 shows the droplet distributions at each stage of the data conditioning process for the 052996.04 case. Tables 3.2 and 3.3 present the roughness parameters at each stage of the data conditioning process for the 052996.04 and 053096.01 cases, respectively. Table 3.2 shows that roughness parameters for the 053096.01 case were not "scaled" because the "Truncated and Stretched" parameters showed good agreement to the reported data.

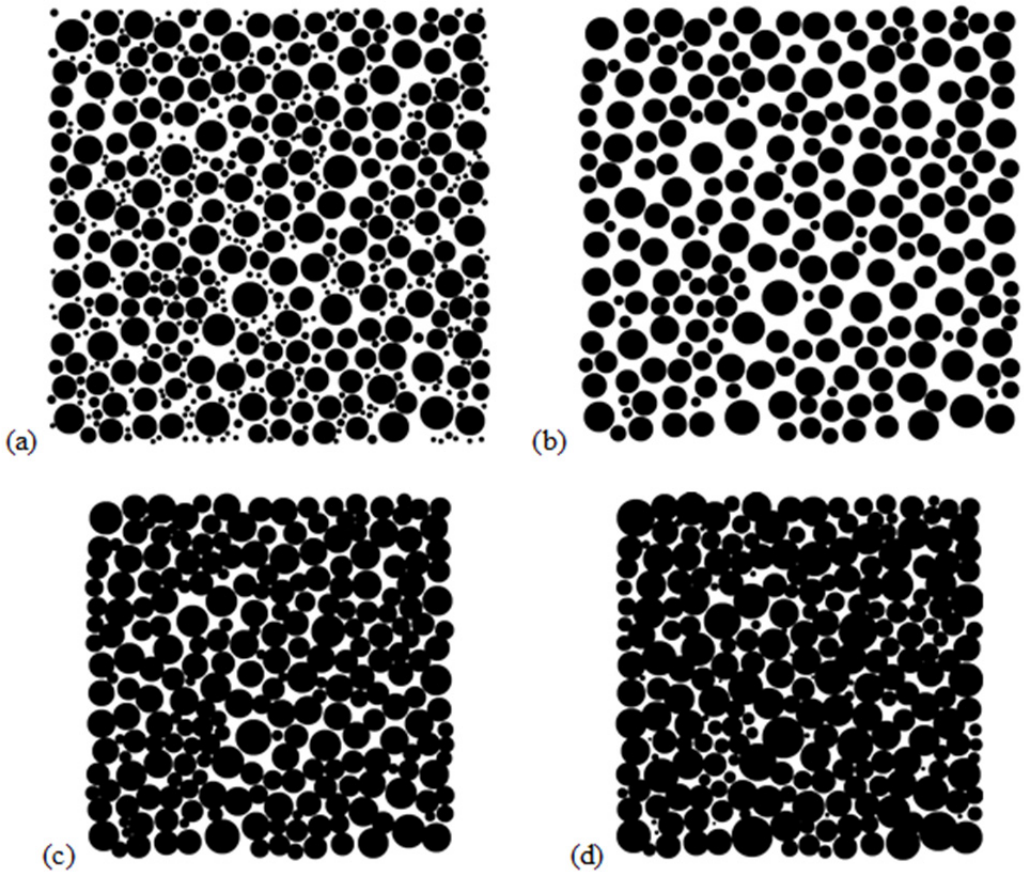


Figure 3.9: Droplet distributions for the 052996.04 case corresponding to a) unconditioned simulator data, b) truncated data, c) truncated and stretched data, and d) truncated, stretched, and scaled data [4]

Table 3.2: Comparison of roughness parameters for the 052996.04 case throughout data conditioning [4]

| Parameter | Reported Data [29,34] | Unconditioned Simulator Data | Truncated | Truncated and Stretched | Truncated, Stretched, and Scaled |
|---|---|---|---|---|---|
| $D_{mean}$ (mm) | 0.936 | 0.583 | 1.037 | 1.037 | 1.037 |
| $S_E$ (mm) | 0.372 | 0.410 | 0.254 | 0.254 | 0.381 |
| $(P/D)_{mean}$ | N/A | 1.330 | 1.057 | 0.878 | 1.032 |
| $P_{mean}/D_{mean}$ | 1.2 | 0.979 | 1.012 | 0.840 | 0.840 |
| H/D | 0.515 | 0.50 | 0.50 | 0.50 | 0.50 |

Table 3.3: Comparison of roughness parameters for the 053096.01 case throughout data conditioning [4]

| Parameter | Reported Data [29,34] | Unconditioned Simulator Data | Truncated | Truncated and Stretched |
|---|---|---|---|---|
| $D_{mean}$ (mm) | 0.573 | 0.472 | 0.586 | 0.586 |
| $S_E$ (mm) | 0.148 | 0.201 | 0.152 | 0.152 |
| $(P/D)_{mean}$ | N/A | 1.143 | 1.143 | 0.870 |
| $P_{mean}/D_{mean}$ | 1.2 | 1.014 | 1.014 | 0.840 |
| H/D | 0.515 | 0.50 | 0.50 | 0.50 |

*Contemporary ice roughness.* One realistic ice roughness distribution was created by varying the roughness parameters in the longitudinal-surface direction. The IRT at was used to create an ice accretion on a 21" chord NACA 0012 airfoil that spanned the entire 72" of the wind tunnel test section. The airfoil was set at 0° angle of attack. The airflow and cloud characteristics used to generate the ice roughness data for the 113012.04 case is reported in Table 3.1. A thermocouple was embedded in the NACA 0012 airfoil to determine when thermal equilibrium was reached with flow. Following the accretion of the ice, the wind tunnel velocity was reduced to approximately 5 m/s while keeping the static temperature around -4 °C to avoid thawing of the ice shape. The iced airfoil was painted with an alcohol-based titanium dioxide paint. A Romer Absolute Arm was placed in the IRT test section upstream of the airfoil and a laser scan was made of the leading 120-150 mm on both sides of the airfoil leading edge. The scan was approximately 100 cm wide (in the spanwise direction) and was performed at the center-span location of the airfoil.

The self-organizing map approach of McClain and Kreeger [7] was then used to characterize the roughness variations along the surface of the NACA 0012 airfoil in the longitudinal-surface direction. In their simplest essence, self-organizing maps are employed to capture tends of large data sets by representing those data sets by a relatively small set of codebook vectors [6]. Figure 3.10 presents a 20 mm strip of the point cloud where each point was color mapped by the height of the surface point relative to the mean surface location.

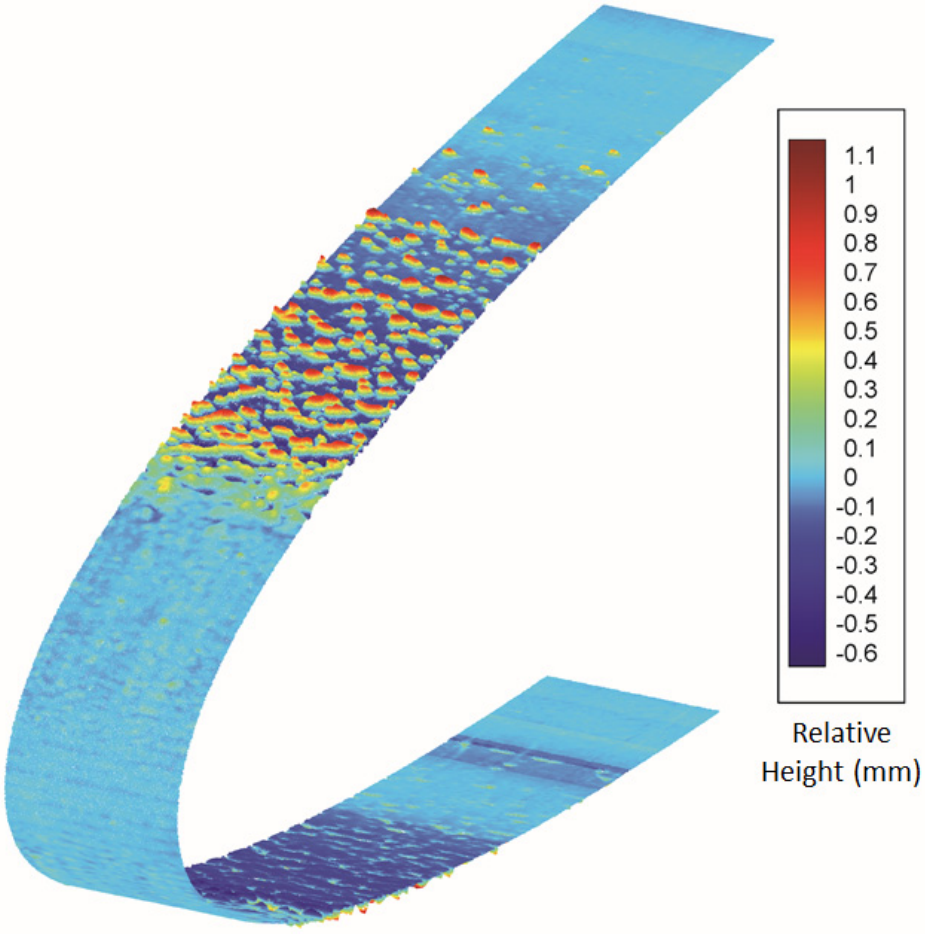


Figure 3.10: A 20 mm wide section of the 113012.04 case point cloud color mapped to normal height from the self-organizing map mean manifold

Figure 3.11 shows the local, 99%-Gaussian roughness maximum height variation evaluated using Eq. (3.2) at each control point or codebook vector used for the roughness characterization of the surface.

$$RMH_{\mathbf{b^n}} = 3.09R_q == 3.09\left[\frac{1}{J}\sum_{j=1}^{J} N_{\mathbf{x}^j}{}^2\right]^{\frac{1}{2}} \tag{3.2}$$

Where $J$ is the number of surface points for which $\mathbf{b^n}$ is the winning (closest) codebook vector.

Figure 3.11 demonstrates that the 113012.04 case exhibits a smooth region up to 30 mm from the stagnation point, and then the roughness height quickly increases to a maximum of approximately 1 mm just before the 50 mm mark. The roughness heights then gradually decay. A series of transition functions were then used to model the variation in roughness height along the surface distance in the flow direction. These functions are represented in Eq. (3.3)

$$F_t(x) = 0.5 + 0.5\tanh\left(\frac{x - x_t}{l_t}\right) \tag{3.3}$$

where $l_t$ is the transition length and $x_t$ is the transition location. The transition function in Eq. (3.3) is one for $x$ values much greater than $x_t$, and zero for $x$ values much less than $x_t$. The transitions can be multiplied by constants or functions to transition between constant values and functions. A linear combination of three transition functions were used to create a scaling function that modeled the measured RMH values of the 113012.04 case. The resulting scaling function is shown in Figure 3.11. The roughness

distribution used to model the 113012.04 case will be discussed in the subsequent section.

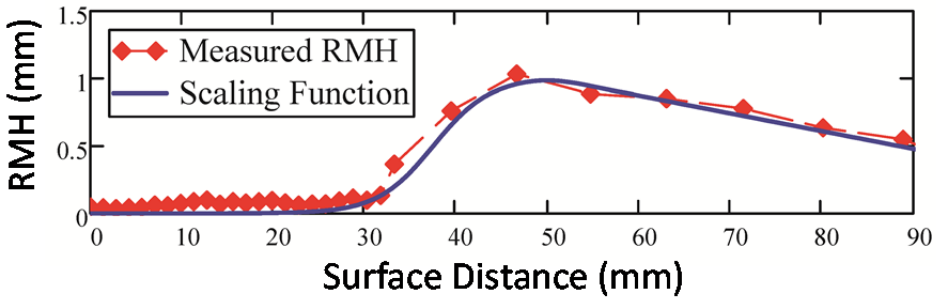


Figure 3.11: 99%-Gaussian maximum roughness height variation for the 113012.04 case point cloud

*Manufacturing Surface Panels*

As previously mentioned, a geometric scaling of 10x was applied to the surface distance from the leading edge and to the roughness dimensions. Therefore, the roughness distributions created with the Lagrangian droplet simulator were increased by a factor of 10. The roughness distributions then were replicated in a 4x6 pattern to cover the surface of the instrumented test plate. This was done to prevent preferential flow in the spanwise direction. Figure 3.12 shows the 052996.04 case as it was scaled 10x and replicated. Two surfaces were created using the 052996.04 case, and are identified as 052996.04_x10 and 052996.04_x10_SSL going forward. These surfaces have the identical roughness distribution, but the 052996.04_x10_SSL surface contains a smooth-zone starting length. It should be noted that the smooth-zone length was not reported by Anderson et al. [34]. As discussed by Walker et al. [36], the original images for the 052996.04 case (Figure 3.8(a)) were obtained from NASA to measure the width of the

smooth-zone. The final roughness surface for the 053096.01 case is identified as 053096.01_x10 going forward.

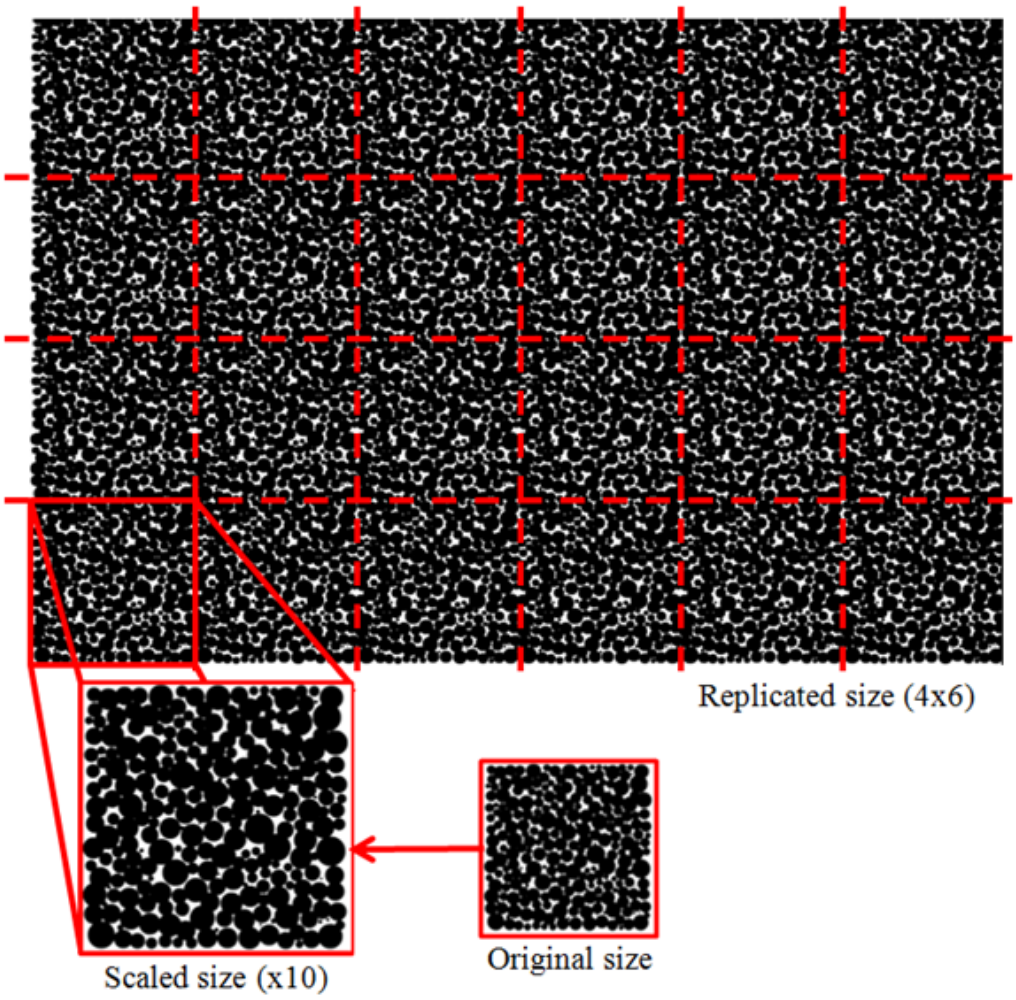


Figure 3.12: Scaled and replicated roughness distribution for the 052996.04 case (not to scale) [4]

In inspecting the roughness distribution of the 052996.04_x10 case, it was observed that maximum element diameter was 19 mm, which resulted in a maximum roughness element height of 9.5 mm. The 113012.04 case was chosen for this investigation because the maximum RMH value shown in Figure 3.11, when scaled by a factor of 10, is essentially the same height as the roughness of the 052996.04_x10 case.

Consequently, the same basic roughness pattern that was used for the 052996.04_x10 case was used to create the roughness for the scaled 113012.04 case. The 113012.04_IRT surface was generated by multiplying the 052996.04_x10 surface by the scaling function shown in Figure 3.11 with the surface distance scaled by 10.

The following steps were taken to complete the manufacturing process of the surface panels:

1. Smooth surface panels were created in SolidWorks.
2. The roughness distribution data was deconstructed into 25 subsets, one for each surface panel.
3. A SolidWorks macro was used to generate a solid model of the roughness distribution on each of the smooth surface panels.
4. The surface panels were manufactured using 3D printing. An Objet 30 was used to print Row C (see Figure 3.5 for the surface panel row/column naming designation) and a Dimension 768 SST was used to print the remaining surface panels.
5. 1/16" neoprene gaskets were affixed to the bottom of the surface panels. For the heated section, this was done to produce an even contact pressure between the Mylar film heaters and the surface panels.
6. The surface panels in the heated section (Row C) were spray painted with a thin coat of flat black paint to provide a known surface emissivity of 0.95.

The solid models of the resulting surfaces are shown in Figure 3.13. Figure 3.13 demonstrates the significant differences in the conceptual treatment of ice roughness. The 052996.04_x10_SSL and 053096.01_x10 surfaces reflect the historical treatment of ice

roughness, with an abrupt smooth-to-rough transition and constant roughness properties downstream of the transition. The 113012.04_IRT surface reflects a more contemporary treatment of ice roughness, with a realistic variation in the maximum roughness height.

A set of smooth validation surfaces were also manufactured. The Smooth Laminar and Smooth Turbulent surfaces are simply the smooth surface panels, with one caveat. The Smooth Turbulent surface has a 2 mm square trip at the end of the bullnose curvature to induce transition to turbulent flow.

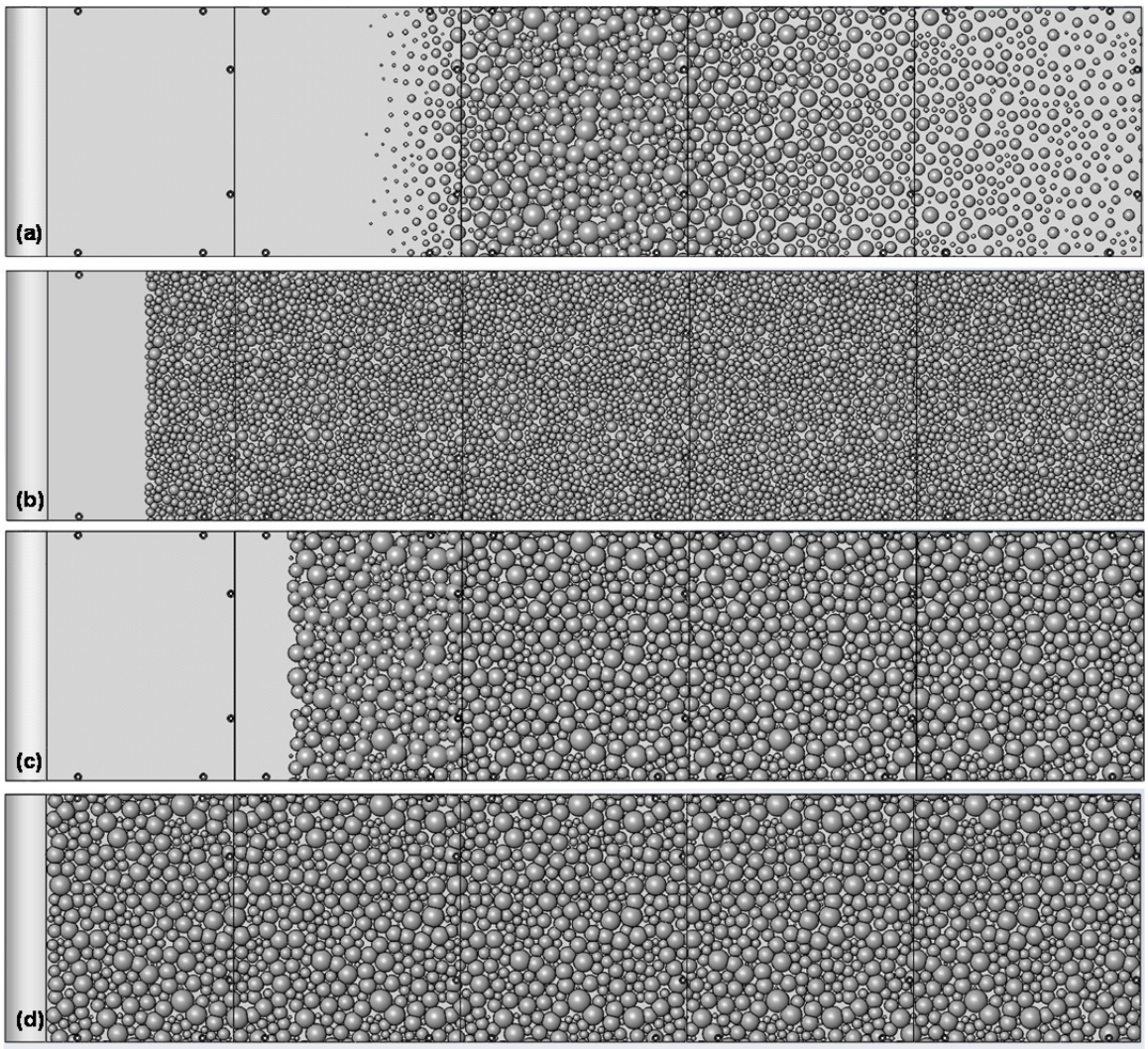


Figure 3.13: Row C surface panel assemblies of a) 113012.04_IRT, b) 053096.01_x10, c) 052996.04_x10_SSL, and d) 052996.04_x10 (flow is from left to right)

## *Ceiling Insert for Flow Acceleration*

### *Ceiling Insert Design*

The ceiling insert was designed to replicate the flow acceleration found along a 21" chord NACA 0012 airfoil at 0° angle of attack. In designing the shape of the insert, the desire was to match the local Reynolds number variation as shown in Eq. (3.4).

$$\left.\frac{\rho U_e x}{\mu}\right|_{Plate} = \left.\frac{\rho U_e s}{\mu}\right|_{\substack{NACA \\ 0012}} \tag{3.4}$$

Eq. (3.4) demonstrates that as flow moves downstream in the x-direction from the stagnation point of the test plate, the geometry and velocity are scaled to match the local Reynolds number of the NACA 0012 airfoil as calculated based on the surface distance from the stagnation point of the airfoil in the surface direction (*s*).

To begin the design, a vortex-panel solver was used to generate the variation in pressure coefficient along the surface of a NACA 0012 airfoil. All experiments performed in this investigation occurred at low subsonic speeds (Mach number < 0.1), so compressibility effects were neglected in the solver. The pressure coefficient distribution along the surface of the NACA 0012 airfoil is shown in Figure 3.14. In Figure 3.14, the region to the left of the vertical line is the leading 17.1% of the NACA 0012 airfoil that was modeled.

The pressure coefficient variation was then converted to the velocity variation using Eq. (3.5), where $F_s$ is the surface geometry scaling factor (10).

$$U_e(x) = \frac{U_{\infty,IRT}}{F_s}\left(1 - C_p\right)^{1/2} \tag{3.5}$$

Figure 3.15 shows the resulting velocity variation. The design velocity variation was then chosen to match the velocity variation around the surface of the NACA 0012 airfoil. Figure 3.15 shows that the acceleration in the first 0.02% of the airfoil near the stagnation region was not matched. This is an inherent complication when attempting to model flow acceleration with a flat plate and ceiling insert, as flow stagnation cannot be achieved easily. The issues in the stagnation region were managed by prescribing a "cut-in" velocity, $U_{CI}$, of 5 m/s. This means that in the bullnose region, which is unheated, the ceiling insert was designed to provide a flow velocity of 5 m/s. Downstream of the bullnose, the design velocity variation converged to the velocity variation of the airfoil.

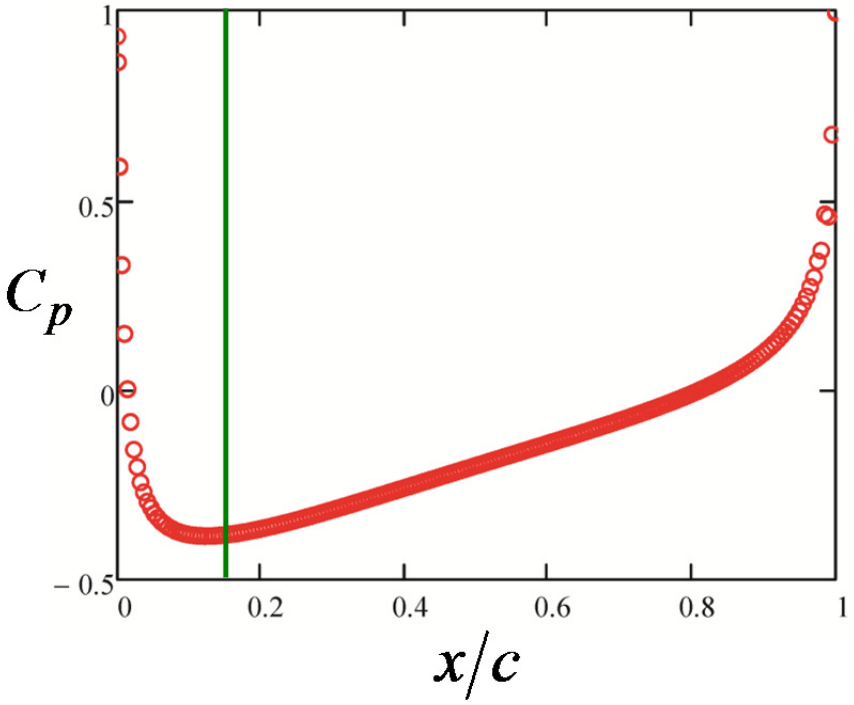


Figure 3.14: Pressure coefficient variation along a low speed NACA 0012 airfoil

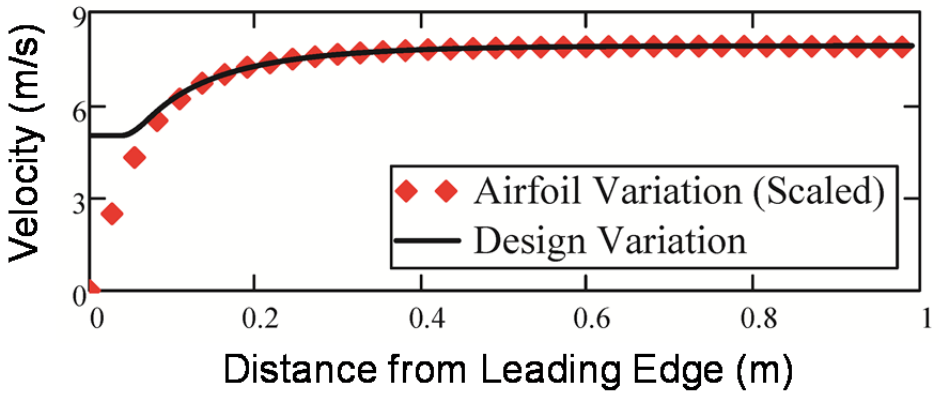


Figure 3:15: Scaled airfoil velocity variation and design velocity variation

The desired velocity variation on the test plate was then imported to a boundary layer code that calculates the momentum thickness growth on the test plate and on the ceiling of the wind tunnel test section. Using the desired velocity on the test plate and the known changes in the momentum thickness along the wind tunnel surfaces, the thickness profile of the ceiling insert was calculated using Eq. (3.6).

$$H(x) = H_s \frac{U_{CI}}{U_e(x)} + \Delta\theta_P + \Delta\theta_C \tag{3.6}$$

Where $\Delta\theta_P$ and $\Delta\theta_C$ are the changes in momentum thickness along the test plate and ceiling, respectively and $H_s$ is the distance from the test plate surface to the test section ceiling without the ceiling insert (12").

*Ceiling Insert Construction*

Figure 3.16 shows a solid model of the completed ceiling insert. The insert includes a wood mounting plate for installation in the ceiling of the wind tunnel test section.

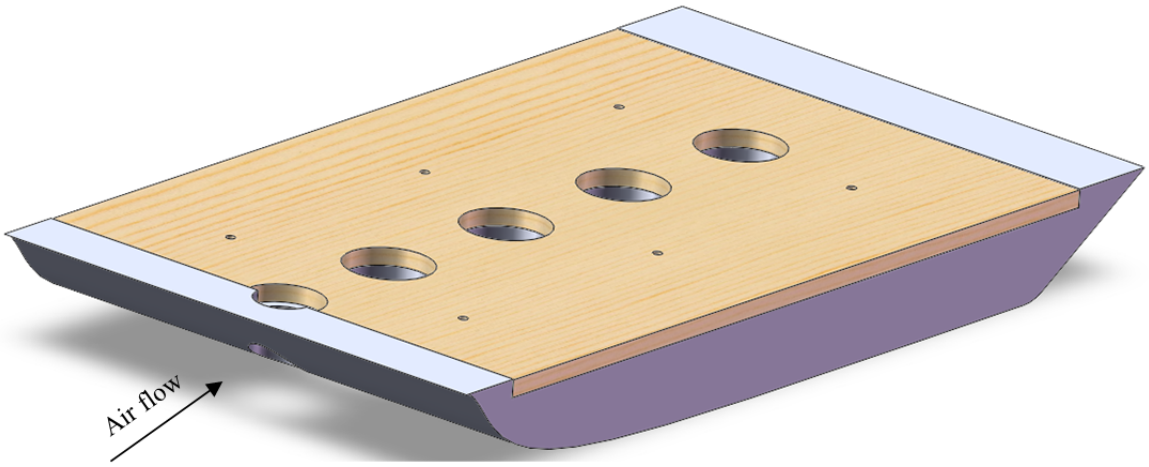


Figure 3.16: Solid model of ceiling insert

The profile of the ceiling insert was cut from a solid block of surfboard foam using a hot wire CNC foam cutter. The insert was constructed out of foam due to its relatively low cost and weight. The profile of the foam insert is shown in Figure 3.17(a). It should be noted that the 35.00" x 23.85" x 0.78" recess was cut from the top of the foam insert to accommodate the wood mounting plate. An 8" Hot Wire Foam Factory Hot Knife was then used to cut five cylindrical ports from the foam insert. These ports, shown in Figure 3.17(b), allowed for measurements to be taken in the wind tunnel test section. The ports are centered directly above the center of each heated section on the instrumented test plate. Figure 3.17(b) shows that the measurement port on the left-hand side of the foam insert was cut to a smaller diameter compared to the other ports. This was done in an effort to minimize the interference of the port with the curved profile of the insert at this location.

The mounting plate was constructed from a 35.00" x 23.85" x 0.75" wood plate. A router was used to machine five cylindrical ports in the wood plate at the same location as the ports in the foam insert. A drill press was then used to machine six 0.4" diameter

through-holes in the wood plate. Threaded inserts with a 3/8" diameter were pressed into the through-holes. The threaded inserts function as mounting points to the ceiling of the wind tunnel test section.

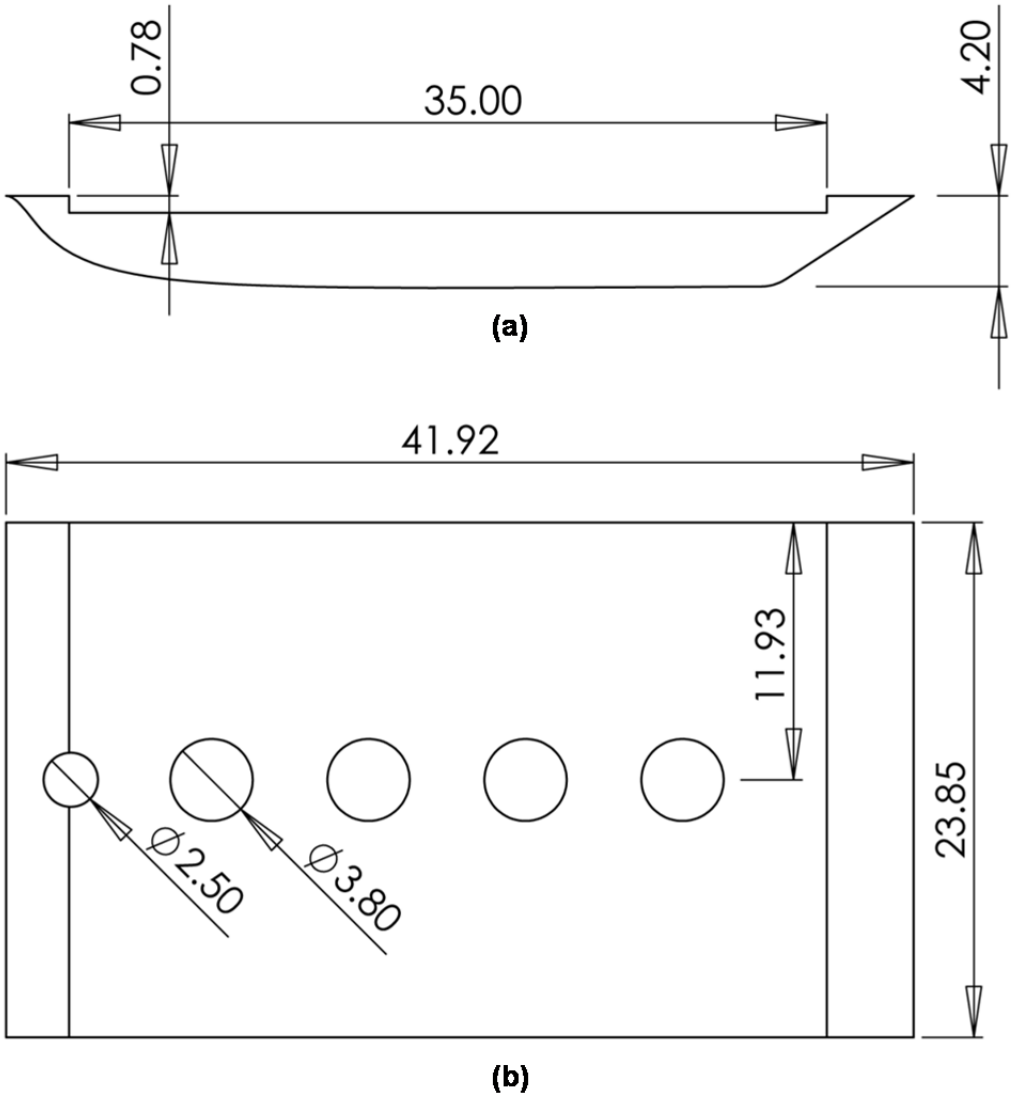


Figure 3.17: Foam insert profile as shown from a) side-view and b) top-view (dimensions in inches, flow is from left to right)

The wood mounting plate was affixed to the foam insert using Gorilla Glue. Lines of original Gorilla Glue were placed in the recess of the foam insert, and the wood

mounting plate was fitted in the recess. Ratcheting bar clamps were placed on the lateral edges of the foam insert and wood mounting plate. The assembly was left undisturbed for 24hrs while the glue cured.

### *Experimental Setup and Procedure*

All of the testing was performed in the Baylor University Subsonic Wind Tunnel (BUSWT), a Model 406B manufactured by Engineering Laboratory Design, Inc. The wind tunnel test section has cross-sectional dimensions of 24" x 24", and a length of 48" in the flow direction. A 40 horsepower, variable speed electric motor drives a constant pitch fan. The BUSWT is capable of producing airflows ranging from 0.1 m/s to 50 m/s with a velocity variation over the test section of less than ±1%. A honeycomb inlet and three high-porosity screens provide an inlet turbulence intensity of approximately 0.2%.

Two experiments were performed for each of the six surfaces in this investigation: 1) steady-state convective heat transfer coefficient measurements and 2) velocity boundary layer measurements. Figure 3.18 shows a sketch of the experimental setups for these experiments. The experimental equipment and procedures used are detailed in the following sections.

#### *Convection Measurements*

The convection tests employed a FLIR SC4000 ThermoVision IR camera with a 25 mm lens. The SC4000 has an indium-antimonide (InSb) detector capable of generating 320 by 256 pixel maps of temperature across a surface. The total viewing area for each image was 6.4" in the flow direction and 5.12" in the span direction. The data from the IR camera was recorded using FLIR ExaminIR software.

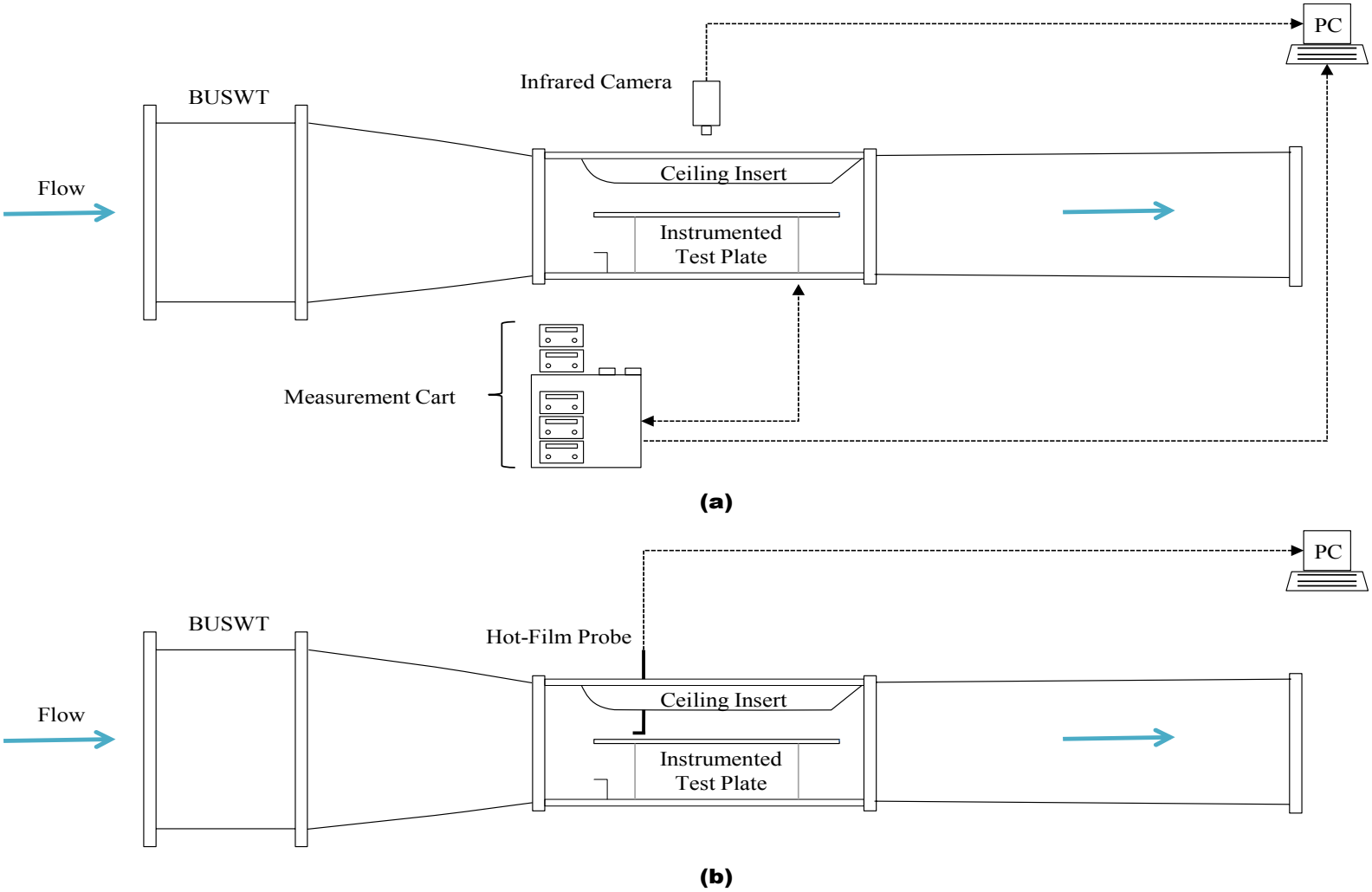


Figure 3.18: Side view of overall experimental setup for a) the convection tests and b) velocity boundary layer tests (not to scale)

FLIR IRW-3C calcium-fluoride windows were used to allow infrared (IR) access to each of the heated sections of the instrumented test plate. The windows were installed at a 30° angle to eliminate reflections from the IR camera. A one-dimension Velmex traversing system was installed on the ceiling of the wind tunnel test section to control the position of the IR camera. The IR camera is mounted on the traversing system via an aluminum carriage. Figure 3.19 illustrates the traversing system and IR windows installed in the test section.

A 6" Pitot-static probe and an Omega PCL-2A pressure transducer with a PCL-MA-01WC pressure module were used to monitor the freestream velocity. A Type K thermocouple was attached to the Pitot-static probe to measure the freestream temperature. Additionally, the ambient temperature, pressure, and relative humidity were measured using a zSeries-THPB-LCD atmospheric conditions monitor from Omega.

For the test cases with negligible freestream acceleration, the Pitot-static probe was installed on the ceiling of the wind tunnel test section. Conversely, for the test cases with freestream acceleration, the Pitot-static probe was installed on the floor of the wind tunnel test section to avoid interference with the ceiling insert. A calibration procedure was then performed to ensure that the correct freestream velocity was achieved over the top surface of the test plate. With the Smooth Laminar surface installed on the test plate, a second Pitot-static probe was placed in the flow between the ceiling insert and the test plate at heated Section 3. The wind tunnel velocity was adjusted so that the measured dynamic pressure at this location coincided with the theoretical dynamic pressure from the ceiling insert design. The dynamic pressure measured by the Pitot-static probe installed in the floor of the test section was then recorded (0.1595 in$H_2O$). Subsequently,

for each surface that was tested with freestream acceleration, the wind tunnel velocity was set by matching this pressure as measured by the floor Pitot-static probe.

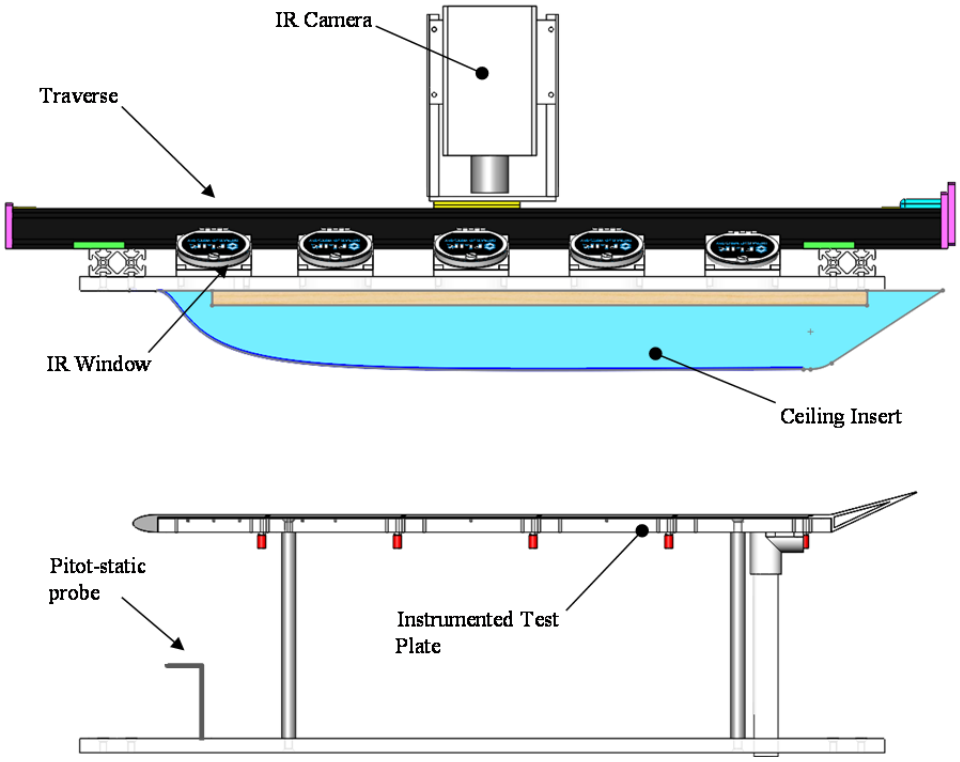


Figure 3.19: Side view of convection test section

A wooden rolling cart was modified by Tecson [4] to house the following equipment: power supplies, current transducers, data acquisition (DAQ) modules, and supermeters. The outfitted cart is shown in Figure 3:20. Five BK Precision power supplies were used to provide power to the Mylar film heaters, one power supply for each heater. For heated Sections 0-3, the voltage across each heater was measured using a National Instruments (NI) 9929 DAQ module. The current through the heater at Section 0 was measured using a Powertek CTH/20A/TH/24Vdc Type 1 current transducer and the current through the heaters at Sections 1-3 were measured using three Powertek CTH/10A/TH/24Vdc Type 1 current transducers. The outputs from the transducers were

read using an NI 9205 DAQ module. The NI 9929 and NI 9205 DAQ modules were mounted in an NI cDAQ-9172 chassis. The voltage across and the current through the heater at Section 4 was measured using two Newport TrueRMS HHM290/N Supermeters. Supermeters were used due to equipment availability. Figure 3.21 shows a wiring diagram for the heated section measurements. The eight thermocouple pairs affixed to the instrumented test plate and the one freestream thermocouple were connected to five NI 9211 DAQ modules mounted in a separate NI cDAQ-9172 chassis. The outputs from the DAQ modules were read using LabVIEW software. The lights over the test section were dimmed and a black felt sheet was placed over the test section to minimize any radiative effects from the lights within the room.

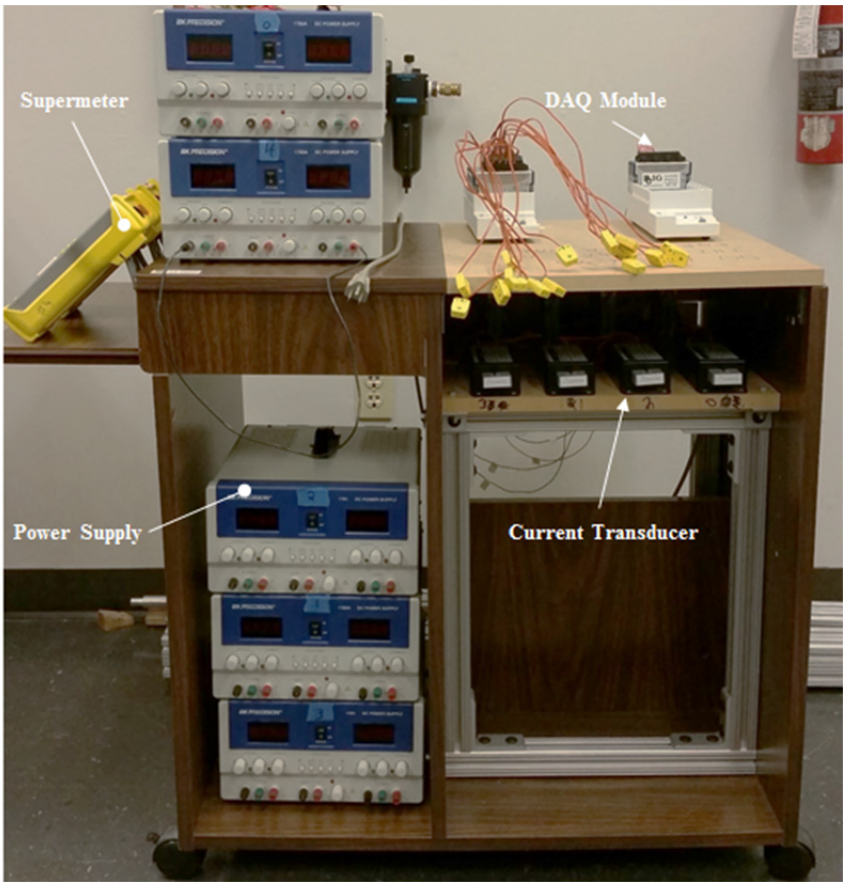


Figure 3.20: Modified wood cart outfitted with experimental equipment

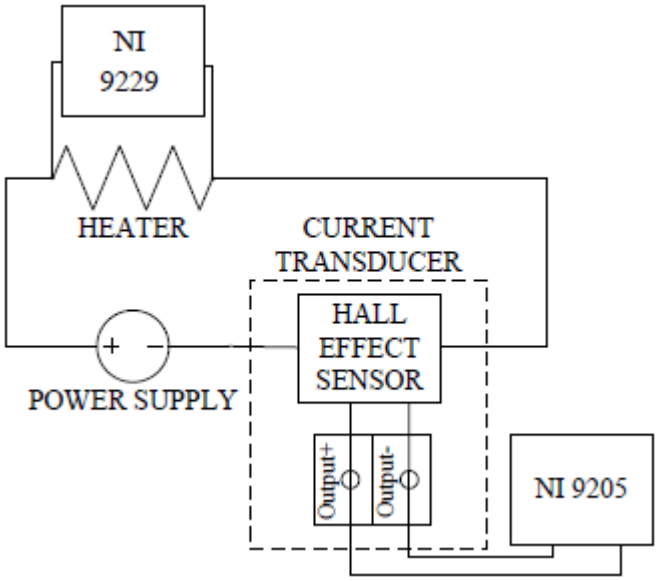


(a) Sections 0-3

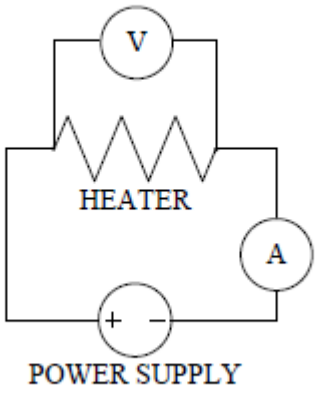


(b) Section 4

Figure 3.21: Wiring diagram for heated sections [4]

Before testing began, several procedures were performed a day in advance. The instrumented test plate (with surface panels of interest attached) was installed in the wind tunnel test section, and the Pitot-static probe was installed in the test section. Instrument wiring from the test plate was connected to corresponding equipment on the modified wood cart, and the IR camera was focused. The test section was left undisturbed

overnight to ensure that the temperature of the test plate and ambient air were nominally equal. The following procedure was used for the convection tests:

1. The IR camera was powered on and left undisturbed for fifteen minutes. This was done to allow the camera's detector to reach operating temperature.
2. The PCL-2A pressure transducer, current transducers, DAQ modules, and traversing system were powered on.
3. Two LabVIEW programs were started. The first program read the DAQ, zSeries, and PCL-2A pressure measurements. Temperature measurements were performed at 3 samples per second for 21 samples, and voltage measurements were performed at 100 samples per second for 100 samples. The second program controlled the position of the IR camera via the traversing system.
4. The ExaminIR software was started. Calibration images were taken at each of the heated sections. The IR camera recorded 70 frames at a rate of 7 frames per second for each of the five heated sections.
5. The PCL-2A pressure transducer was zeroed and the wind tunnel started. As previously mentioned, the velocity in the test section was set according to a measured dynamic pressure of 0.1595 in$H_2O$ by the floor Pitot-static probe.
6. The five power sources were turned on and set to provide a nominal flux of 500 W/$m^2$ for each heater.
7. The temperatures read by thermocouples affixed the test plate were monitored using LabVIEW until steady-state was achieved. This process generally took 2 hours.

8. Steady-state images were taken at each of the heated sections. The IR camera recorded 70 frames at a rate of 7 frames per second for each of the five heated sections.
9. The voltage and current in Section 4 was manually recorded when the image set was recorded in said section.
10. The equipment was powered down starting with the power supplies.

*Velocity Boundary Layer Measurements*

Hotwire anemometry tests were performed to characterize the velocity boundary layer at the center of each heated section. The only instrumentation required from the previous tests was the Pitot-static probe, PCL-2A pressure transducer, and zSeries conditions monitor. The sections were not heated for this test, so temperature and power data was not acquired. The ceiling from the convective heat transfer tests was modified to include a Velmex two-dimensional traversing system to allow movement in the vertical ($z$) direction. Figure 3.22 shows the modified ceiling with the two-dimensional traversing system. A model 1246-20 x-array hot-film probe powered by a TSI Inc., IFA300 constant temperature anemometry system was used to acquire velocity boundary layer data. ThermalPro software was used to initialize the IFA300 and to assign channels to the x-array probe.

Before boundary layer measurements were taken, a calibration procedure was performed; this was done without the ceiling insert in the wind tunnel test section. The probe was mounted on a Velmex B487TS rotary table at approximately the same height as the Pitot-static probe. A LabVIEW program was used to move the rotary table in 5° increments over a range of ±20°. For each rotation angle, a velocity sweep ranging from

0-20 m/s was performed. At each rotation angle and velocity, an NI 9223 DAQ module in an NI cDAQ-9178 chassis was used to acquire the velocity data from each wire.

For the boundary layer measurements the velocity of the wind tunnel was set using the same procedure as the convective heat transfer tests. The hot-film probe was fed through the measurement ports in the ceiling insert and positioned as close to the surface of the test plate as possible (within 1/64"). Special foam guards were created to make a sealed access through the measurement ports. A LabVIEW program was used to traverse the probe in the Z-direction through a 6", 101 station, geometrically expanding grid with a geometric expansion factor of 1.07. An NI 9223 DAQ module in an NI cDAQ-9178 chassis was used to acquire the velocity data at each of the 101 measurement stations. At each station, 300,000 samples were taken from each wire at a rate of 200,000 samples per second.

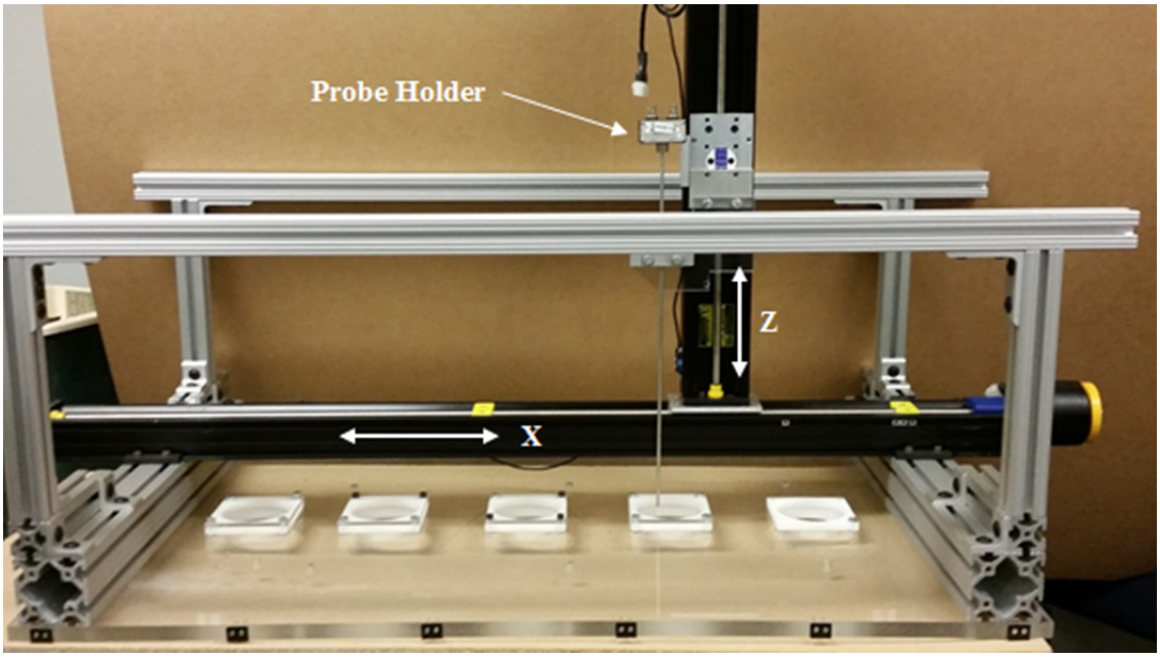


Figure 3.22: Wind tunnel ceiling with two-dimensional traversing system

# CHAPTER FOUR

## Data Reduction and Uncertainty Analysis

This chapter details the development of the data reduction procedures used during the convection and boundary layer tests. The measureable uncertainty associated with the heat transfer coefficients is also discussed.

### *Convection Measurements*

#### *Data Reduction Equation*

Figure 4.1 shows the modes of heat transfer for the steady state convection measurements. Heat is added to the system via the Mylar film heater ($Q_{GEN}$). Heat losses are considered from conduction through the Plexiglas sub-plate ($Q_{HL}$), radiation from the surface panels ($Q_{RAD}$), and convection from the surface panels ($Q_{CONV}$). If a one-dimensional energy balance is applied to Figure 4.1, the resulting equation is given by Eq. (4.1).

$$Q_{GEN} = Q_{HL} + Q_{RAD} + Q_{CONV} \tag{4.1}$$

The convection term is governed by Newton's law of cooling. On a per pixel basis, it is given by Eq. (4.2), where $A_{pix}$ is the pixel area, $T_{IR}$ is the pixel surface temperature as measured by the IR camera, and $T_\infty$ is the freestream temperature.

$$Q_{CONV} = hA_{pix}\left(T_{IR} - T_\infty\right) \tag{4.2}$$

The radiation term per pixel is given by Eq. (4.3), where $\varepsilon$ is the surface panel emissivity and $\sigma$ is the Stefan-Boltzmann constant.

$$Q_{RAD} = \varepsilon\sigma A_{pix}\left(T_{IR}^4 - T_\infty^4\right) \tag{4.3}$$

The conduction through the Plexiglas sub-plate is governed by Fourier's law of conduction. One a per pixel basis, it is given by Eq. (4.4), where $k_p$ is the thermal conductivity of the Plexiglas, $t_p$ is the thickness of the Plexiglas sub-plate, $T_{SS}$ is the Plexiglas sub-plate subsurface temperature as measured by the embedded thermocouples, $T_{UP}$ is the temperature on the bottom of the Plexiglas sub-plate, and $C_k$ is the conduction parameter; it will be discussed later in this chapter.

$$Q_{HL} = C_k \frac{k_p A_{pix}\left(T_{SS} - T_{UP}\right)}{t_p} \tag{4.4}$$

The heat added per pixel is given by Eq. (4.5), where $E$ is the voltage across the Mylar film heater, $I$ is the current through the Mylar film heater, and $A_t$ is the total area of the Mylar film heater.

$$Q_{GEN} = EI\frac{A_{pix}}{A_t} \tag{4.5}$$

Substituting Eqs. (4.2)-(4.5) into Eq. (4.1), the convective heat transfer coefficient at each pixel is given by Eq. (4.6).

$$h = \frac{\dfrac{EI}{A_t} - C_k \dfrac{k_p\left(T_{SS} - T_{UP}\right)}{t_p} - \varepsilon\sigma\left(T_{IR}^4 - T_\infty^4\right)}{T_{IR} - T_\infty} \tag{4.6}$$

The following assumptions were made during the derivation of Eq. (4.6):

- Lateral conduction in the spanwise direction is negligible.
- The Mylar film heaters generate a uniform heat flux.
- The heat loss through the Plexiglas sub-plate is constant across each heated section, as measured by the middle thermocouple.

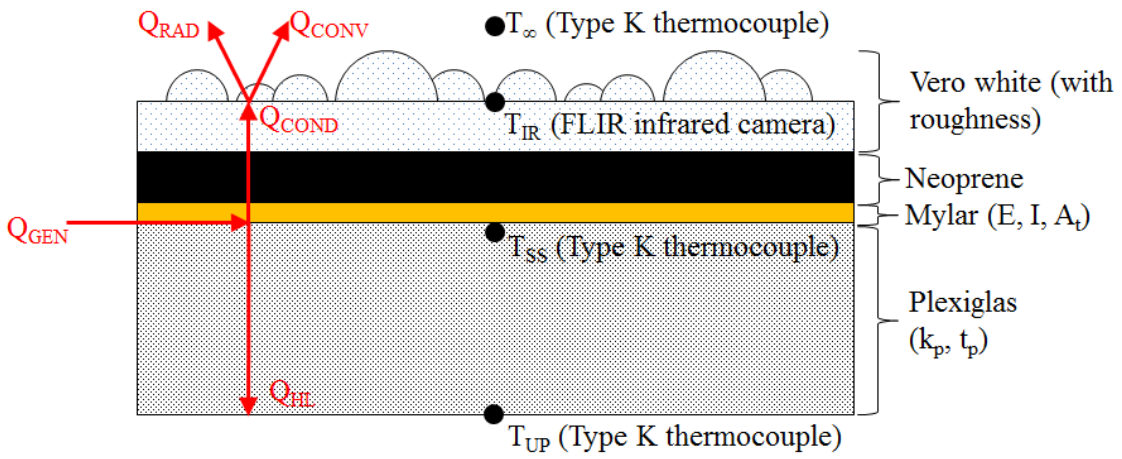


Figure 4.1: Heated section heat flow schematic (not to scale)

In his work with the same instrumented test plate, Walker [5] showed that the conduction term given by Eq. (4.4) is crucial in determining the heat transfer coefficients. When the traditionally accepted Plexiglas thermal conductivity of 0.187 W/m·K [38] was used, the measured heat transfer coefficients were larger than what was predicted using accepted correlations. Since the embedded thermocouples are encased in epoxy, the properties of the epoxy and the contact resistance between the epoxy and the Plexiglas were suspected of causing the differences. Walker [5] constructed an apparatus with the same construction as the Plexiglas sub-plate to measure the thermal conductivity of the system. Through repeated measurements, the average Plexiglas sub-plate thermal conductivity was found to be 0.205 W/m·K. For a detailed account of the thermal conductivity measurements, refer to Walker [5]. Even with the updated thermal conductivity, Walker [5] observed that agreement of the smooth-laminar validation case was off by more than 10%. The hypothesized cause of the differences is the variability of the embedded thermocouple depth. To calibrate the experimental test measurements to the smooth laminar case, $C_k$ parameters were added to the conduction term given by Eq.

(4.4). These parameters were determined by forcing the convection measurements for laminar flow over the test plate to match the theoretical correlations while maintaining continuity in the spanwise averaged heat transfer coefficient variation along the flow direction. The value of the $C_k$ parameter for each heated section is given in Table 4.1.

Table 4.1: Conduction parameter values

| Heated Section Number | $C_k$ |
|---|---|
| 0 | 0.90 |
| 1 | 0.90 |
| 2 | 1.05 |
| 3 | 1.10 |
| 4 | 1.05 |

*Air Properties*

The convection measurements were performed over several weeks. Therefore, the results are compared using non-dimensional Stanton numbers. This required an analysis of the air properties during each convection test. The method for obtaining air properties is identical to the ones used by Mart [18], Tecson [4], and Walker [5]. As noted in Chapter Three, an Omega zSeries zED-THPB-LCD atmospheric conditions monitor was used to record the ambient air temperature, pressure, and relative humidity at the inlet of the wind tunnel. A program based on the International Association for the Properties of Water and Steam guidelines [39], Sutherland's law [40], and Wilke's equation for gas mixtures [41] was then used to calculate the air density, dynamic viscosity, specific heat, thermal conductivity, and Prandtl number.

*Thermocouple Calibration*

An *in situ* calibration was performed to reference the thermocouple measurements to the averaged center 50x50 pixel temperature as measured by the IR camera. This process is shown in Eq. (4.7).

$$T_{TC,calibrated} = T_{TC,test} - \left(T_{TC,cal} - \overline{T}_{IR,cal}\right) \tag{4.7}$$

The thermocouples in each heated section were calibrated to the IR camera measurement for that section. For example, the thermocouples in Section 0 were calibrated using the IR camera measurement at Section 0.

*Smooth Surface Validation*

Convection measurements were performed on a set of smooth surface panels: one with laminar flow over the surface and one with turbulent over the surface. These test cases allowed for validation of the derived data reduction equation. The Smooth Laminar test case produced a Reynolds number of approximately $4x10^5$ at trailing edge of the test plate, which is less than the critical Reynolds number of $5x10^5$. Therefore, the flow over the surface of the test plate should be laminar unless a forced transition to turbulent flow occurred. An example MATLAB script used to perform the data reduction is given in Appendix A.

Figures 4.2 and 4.3 show the steady state temperature and convective heat transfer coefficient surface maps for the Smooth Laminar and Smooth Turbulent surfaces, respectively. In Figures 4.2 and 4.3 the dashed vertical lines indicate the locations of the edges of the heated sections, and the vertical white bands indicate regions where the infrared images did not overlap. In Figures 4.2(b) and 4.3(b) the solid red and yellow

areas located at the upstream and downstream edge of heated Section 0, as well as the upstream edges of heated Sections 1-4, result from the infrared camera capturing the wall temperature of the measurement ports in the ceiling insert.

Stanton numbers were evaluated using the average convective heat transfer coefficient of 1" square areas centered on each of the eight thermocouple pairs embedding in the Plexiglas sub-plate. The results were compared with the theoretical laminar and turbulent correlations given by Eqs. (2.9) and (2.10). Figure 4.4 shows a comparison of the measured and theoretical St for the validation surfaces. Figure 4.4(a) demonstrates the agreement of the measured St to the theoretical prediction for the Smooth Laminar case. Figure 4.4(b) demonstrates that the St measurements for the Smooth Turbulent case are higher than the values predicted by the correlation of Eq. (2.10). The difference for the Smooth Turbulent case is explained by the flow separation from the 2 mm trip employed to force transition to turbulent flow. In passing over the trip, the flow requires a finite length to reattach to the plate; consequently, the start of the turbulent flow is really much later than the bullnose or the trip location. Therefore, the measured St are actually shifted to the right as opposed to above the correlation values.

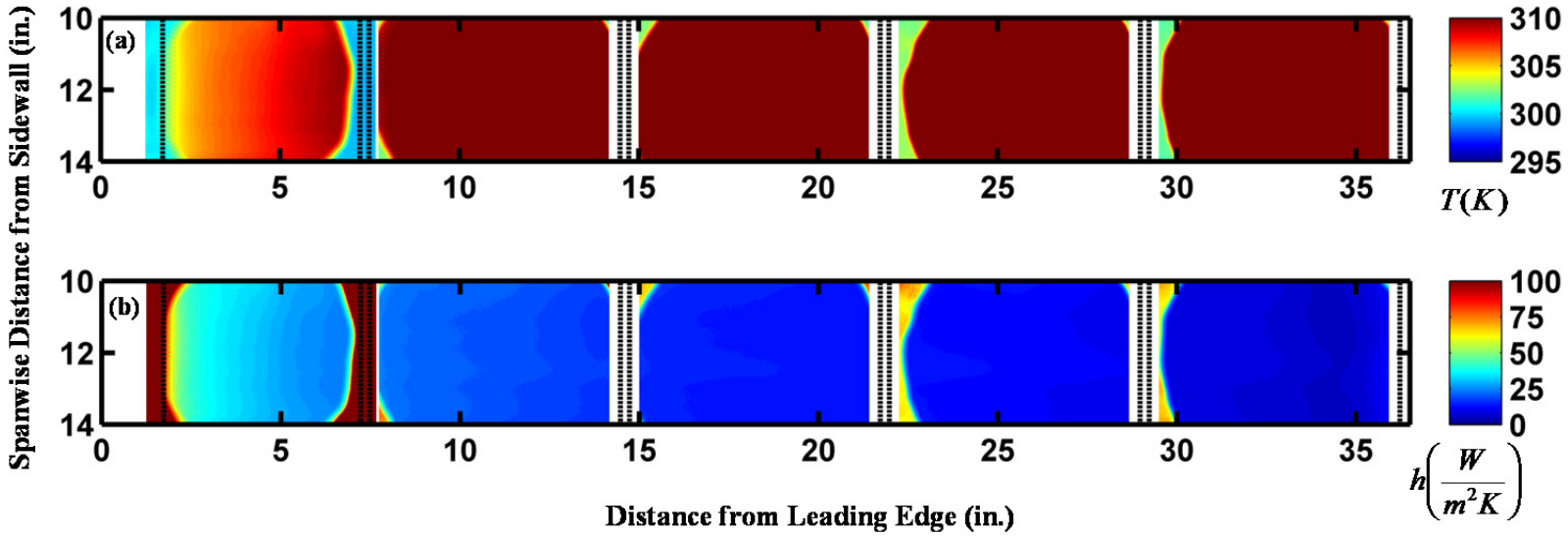


Figure 4.2: Surface maps of Smooth Laminar a) steady state temperature and b) convective heat transfer coefficient

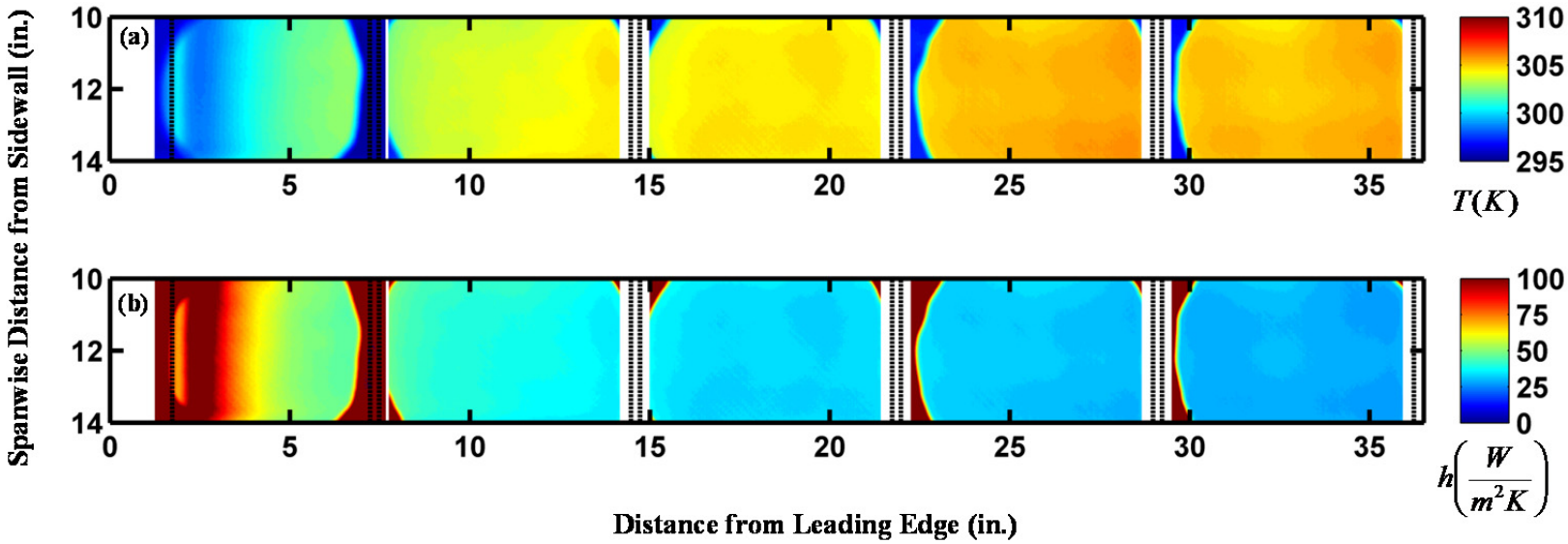


Figure 4.3: Surface maps of Smooth Turbulent a) steady state temperature and b) convective heat transfer coefficient

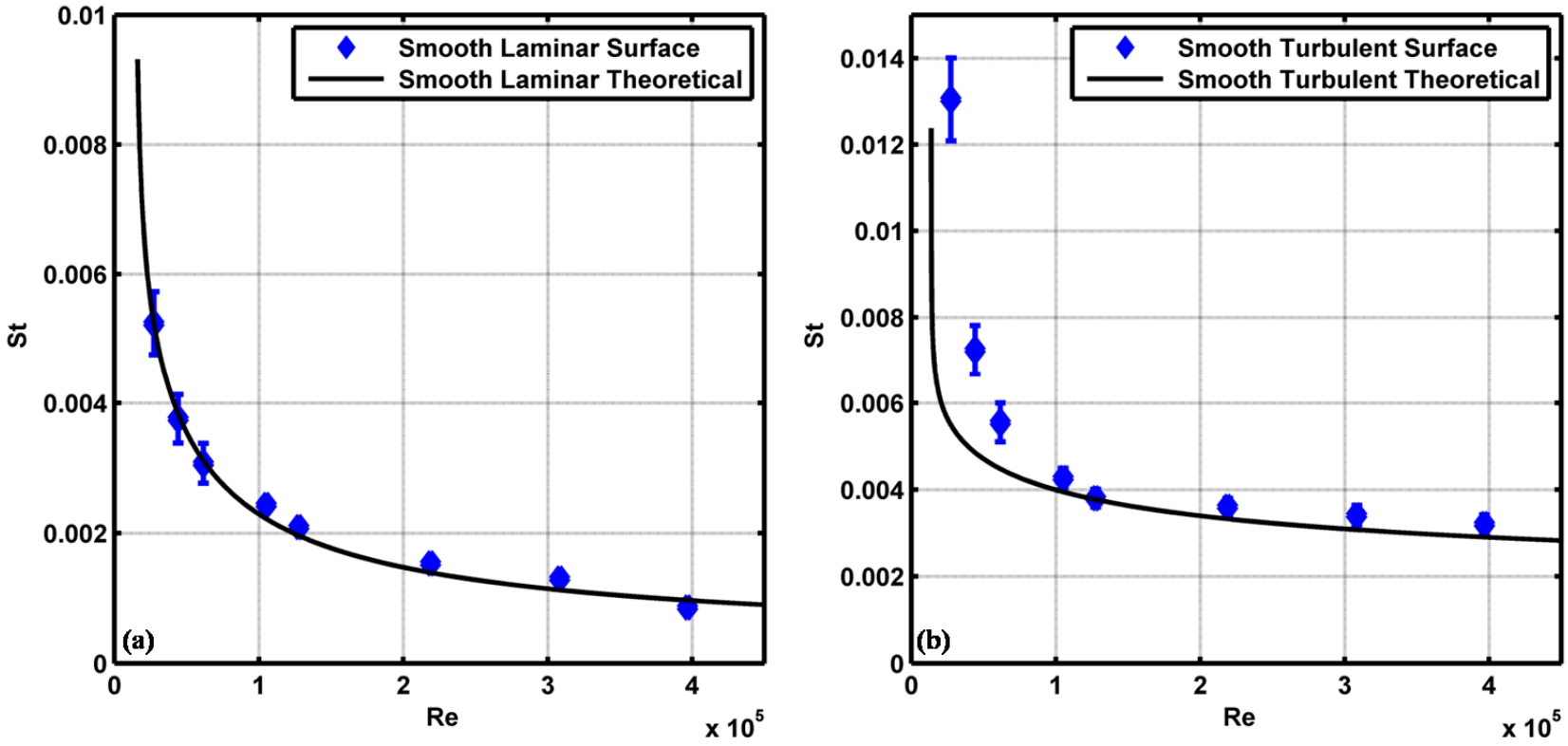


Figure 4.4: Comparison of local experimental and theoretical Stanton numbers for the a) Smooth Laminar case and b) Smooth Turbulent case

*Uncertainty Analysis*

In Chapter Five, area averaged heat transfer coefficients are presented. The uncertainties associated with these local values were determined using the large sample size method of Coleman and Steele [42], which is an extension of the work of Kline and McClintock [43]. Table 4.2 presents a summary of the total uncertainty associated with each variable.

Table 4.2: Convective Heat Transfer Coefficient Measurement Uncertainty

| Variable | Total Uncertainty | Uncertainty Components |
|---|---|---|
| $E$ | $\sqrt{U_{E,fixed}^2 + \left(\frac{tS_E}{\sqrt{N}}\right)^2}$ | $U_{E,fixed} = 0.03\%\ E$ (sections 0 - 3)<br>$U_{E,fixed} = 0.25\%\ E$ (section 4) |
| $I$ | $\sqrt{U_{I,fixed}^2 + \left(\frac{tS_I}{\sqrt{N}}\right)^2}$ | $U_{I,fixed} = 0.1$ A (section 0)<br>$U_{I,fixed} = 0.05$ A (sections 1 - 3)<br>$U_{I,fixed} = 2.5\%\ I$ (section 4) |
| $A_t$ | $\sqrt{\left(U_{d,fixed} W_{ha}\right)^2 + \left(U_{d,fixed} L_{ha}\right)^2}$ | $U_{d,fixed} = 1/32"$ |
| $T_{IR}$ | $\sqrt{B_T^2 + \left(\frac{tS_{T_{IR}}}{\sqrt{N}}\right)^2}$ | $B_T = 1.4$ K |
| $T_{SS}$ | $\sqrt{B_T^2 + \left(\frac{tS_{T_{IR}}}{\sqrt{N}}\right)_{cal}^2 + \left(\frac{tS_{T_{SS}}}{\sqrt{N}}\right)_{cal}^2 + \left(\frac{tS_{T_{SS}}}{\sqrt{N}}\right)_{test}^2}$ | $B_T = 1.4$ K |
| $T_{UP}$ | $\sqrt{B_T^2 + \left(\frac{tS_{T_{IR}}}{\sqrt{N}}\right)_{cal}^2 + \left(\frac{tS_{T_{UP}}}{\sqrt{N}}\right)_{cal}^2 + \left(\frac{tS_{T_{UP}}}{\sqrt{N}}\right)_{test}^2}$ | $B_T = 1.4$ K |
| $T_\infty$ | $\sqrt{B_T^2 + \left(\frac{tS_{T_{IR}}}{\sqrt{N}}\right)_{cal}^2 + \left(\frac{tS_{T_\infty}}{\sqrt{N}}\right)_{test}^2}$ | $B_T = 1.4$ K |

In Table 4.2 the random uncertainty is given by Eq. (4.8), where $t$ is the Student's t-value, $S$ is the standard deviation, and $N$ is the sample size.

$$U_{random} = \frac{t \cdot S}{\sqrt{N}} \tag{4.8}$$

As noted by Walker [4], the uncertainty associated with the thickness of the Plexiglas sub-plate is not assessed due to the handling of the conduction term. That is, because the conduction term was corrected to force agreement between the experiment and theoretical smooth laminar heat transfer coefficients, the uncertainty of the thickness was not thought to propagate through the heat transfer measurements. It is also noteworthy that there is no random uncertainty associated with the voltage or current measurements in heated Section 4, since a single sample was taken for these values. An example Mathcad sheet used to calculate the experimental uncertainty is given in Appendix B.

## *Velocity Boundary Layer Measurements*

### *Probe Calibration*

To begin the x-array probe calibration procedure, the effective velocity experienced by each wire of the x-array probe was calculated using Eqs. (4.9) and (4.10)

$$V_{eff,1} = \sqrt{\left(V_{meas}\cos\alpha_1\right)^2 + \kappa^2\left(V_{meas}\sin\alpha_1\right)^2} \tag{4.9}$$

$$V_{eff,2} = \sqrt{\left(V_{meas}\sin\alpha_2\right)^2 + \kappa^2\left(V_{meas}\sin\alpha_2\right)^2} \tag{4.10}$$

where $V_{meas}$ is the velocity measured by the Pitot-static probe, $\alpha$ is angle of the wire relative to the flow direction, and $\kappa$ is the tangential velocity attenuation factor. For each of the wires, the value of $\kappa$ was 0.115. A fourth-order polynomial was then fit to the calibration measurements for each wire of the x-array probe, shown in Figure 4.5.

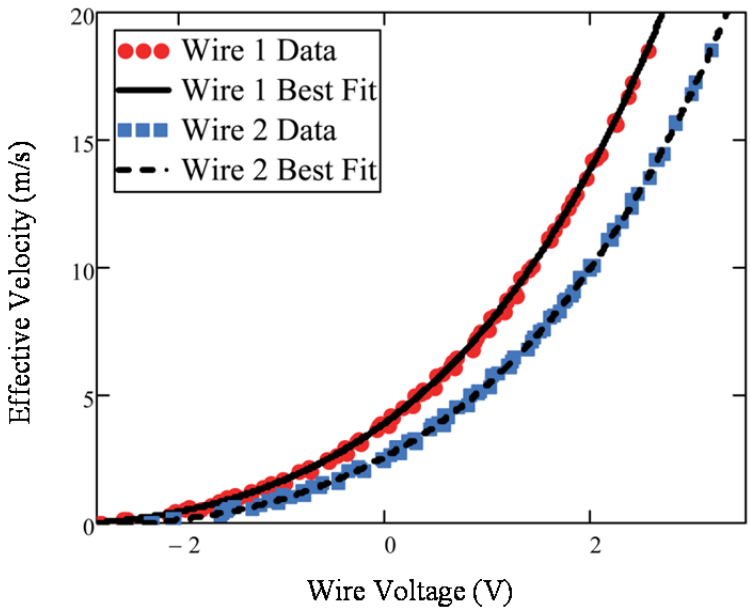


Figure 4.5: Hot-film probe calibration plot

*Data Reduction Equations*

For each set of voltage measurements obtained during the boundary layer tests, the flow velocity normal to the first wire and tangential to the first wire of the probe was determined using Eqs. (4.11) and (4.12), respectively.

$$V_{N1} = \left( \frac{V_{eff,1}^2 - \kappa^2 V_{eff,2}^2}{1 - \kappa^4} \right)^{1/2} \tag{4.11}$$

$$V_{T1} = \left( \frac{V_{eff,2}^2 - \kappa^2 V_{eff,1}^2}{1 - \kappa^4} \right)^{1/2} \tag{4.12}$$

The x and z-components of the flow relative to the probe were then determined using Eqs. (4.13) and (4.14), respectively.

$$u_i = \frac{V_{T1} + V_{N1}}{\sqrt{2}} \tag{4.13}$$

$$w_i = \frac{V_{T1} - V_{N1}}{\sqrt{2}} \tag{4.14}$$

At each measurement station, the mean velocity components are given by Eqs. (4.15)-(4.16) and the root-mean-square turbulent fluctuating velocity components are given by Eqs. (4.17)-(4.18).

$$\overline{u} = \frac{1}{N}\sum_{i=1}^{N} u_i \tag{4.15}$$

$$\overline{w} = \frac{1}{N}\sum_{i=1}^{N} w_i \tag{4.16}$$

$$u'_{RMS} = \sqrt{\frac{1}{N-1}\sum_{i=1}^{N}\left(u_i - \overline{u}\right)^2} \tag{4.17}$$

$$w'_{RMS} = \sqrt{\frac{1}{N-1}\sum_{i=1}^{N}\left(w_i - \overline{w}\right)^2} \tag{4.18}$$

# CHAPTER FIVE

## Results and Discussion

This chapter presents the results of the convection tests for the rough surfaces both with and without freestream acceleration. For the cases with negligible freestream acceleration (i.e. without the ceiling insert), the data for the 052996.04_x10 and 053096.01_x10 surfaces were first presented by Walker [5] and are replicated here for comparison. The results of the boundary tests on the validation and rough surfaces are also presented and discussed. For the cases with negligible flow acceleration, the data for the Smooth Laminar, Smooth Turbulent, 052996.04_x10, and 053096.01_x10 surfaces were first presented by Tecson [4].

### *Convection Results*

Figures 5.1 and 5.2 present the local convection coefficient contour maps for the rough surfaces without and with the ceiling insert, respectively. Figures 5.1 and 5.2 illustrate the effect the ceiling insert has on each of the rough surfaces in this investigation. For each of the surfaces, the accelerated cases exhibit higher convection coefficients than the cases with negligible freestream acceleration. This is particularly noticeable in the surface panels with roughness elements.

Similar to the validation surfaces presented in Chapter Four, local Stanton numbers were used to better compare the measured convection coefficients. Figures 5.3 and 5.4 present the 1" square area averaged Stanton numbers for each flow condition and each rough surface tested in this investigation. For the negligible flow acceleration cases,

the experimental measurements were compared to the theoretical laminar and turbulent correlations given by Eqs. (2.7) and (2.8). For the accelerated flow cases, the experimental measurements were compared to the theoretical correlations given by Eqs. (2.9) and (2.10). All of the surfaces tested in this investigation have an unheated starting length due to the implementation of the bull-nose at the leading edge of the test plate. That is, Eqs. (2.7)-(2.10) were evaluated using $\xi = 1.7285"$. The local convection coefficients used in the Stanton number calculations are given in Table 5.1. A complete set of test data for the accelerated cases, as well as the un-accelerated 113012.04_IRT and 052996.04_x10_SSL cases, can be found in Appendix C.

Figure 5.3 shows an interesting result that there is not a statistical difference between the measured St for the 052996.04_x10, 052996.04_x10_SSL, and 113012.04_IRT surfaces for heated Sections 2-4. Figure 5.3 demonstrates that the 052996.04_x10_SSL and 113012.04_IRT surfaces exhibit different behaviors in the smooth-to-rough transition regions, but once the flow reaches the maximum roughness height for the 113012.04_IRT surface, and the roughness characteristics match those of the 052996.04_x10 and 052996.04_x10_SSL cases, the measured convection coefficients are not statistically different. That is, the uncertainty bars associated with these surfaces overlap.

Figure 5.3 also shows that there is not a statistical difference between the measured St for the 052996.04_x10 and 053096.01_x10 surfaces for heated Section 1. This is interesting given the disparity in size of the roughness elements of these surfaces. This result can be attributed to the smooth-to-rough transition that occurred for the 053096.01_x10 surface. As a result of the transition, the measured St for the

053096.01_x10 surface increases to a maximum at heated Section 1 and then decreases in the flow direction. Accordingly, the St values for the 053096.01_x10 surface then diverge from the other rough surfaces for heated Sections 2-4.

Figure 5.4 shows the effect freestream acceleration has on the measured St values for the rough surfaces with constant roughness properties in the flow direction. Specifically, the 053096.01_x10, 052996.04_x10, and 052996.04_x10_SSL surfaces show St enhancement values up to 20% relative to the negligible flow acceleration cases. These results are comparable to previous investigations regarding surface roughness coupled with freestream acceleration [14,15,16].

Figure 5.4 also shows that for the accelerating flow cases, the freestream acceleration causes a discernable difference in the measured St values for the 052996.04_x10_SSL and 113012.04_IRT surfaces. These two surfaces exhibit similar smooth-to-rough transition behavior compared to the cases with negligible freestream acceleration. However, at heated Section 2, which is the surface panel where the roughness properties of the surfaces match, the 113012.04_IRT surface exhibits lower St values and values that decrease with increasing Reynolds number. An explanation for the difference for the accelerating flow cases is that in the presence of a favorable pressure gradient, the later and more gradual increase in roughness properties of the 113012.04_IRT surface does not generate the elevated levels of turbulence near the roughness resulting in lower St values. For the cases with negligible freestream acceleration, the smooth-to-rough transition occurs more abruptly for both of these surfaces and results in similar levels of turbulence near the roughness elements at the center of heated Section 2.

Lastly, Figure 5.4 shows that the freestream acceleration causes the measured St of the 053096.01_x10 surface to be similar to the measured St of the 113012.04_IRT and 052996.04_x10 surfaces for heated Sections 2-3. However, only the 113012.04_IRT surface has a St value that is statistically equivalent to the measured St value of the 053096.01_x10 surface for heated Section 4. This result is somewhat surprising given the other surfaces with constant roughness properties (i.e. 052996.04_x10 and 052996.04_x10_SSL) both exhibit no appreciable change in the measured St from heated Section 3 to 4, but the 053096.01_x10 surface exhibits a noticeable decrease in St value. A possible explanation for these trends is that the combination of the smooth-to-rough transition and the magnitude of the local freestream acceleration of the 053096.01_x10 case causes elevated levels of turbulence near the roughness and results in higher St for heated Sections 2-3. However, further downstream (Section 4) there is a negligible change in freestream velocity and the large roughness elements of the 052996.04_x10 and 052996.04_x10_SSL surfaces generate elevated levels of freestream turbulence, and therefore higher St values, compared to the 053096.01_x10 surface.

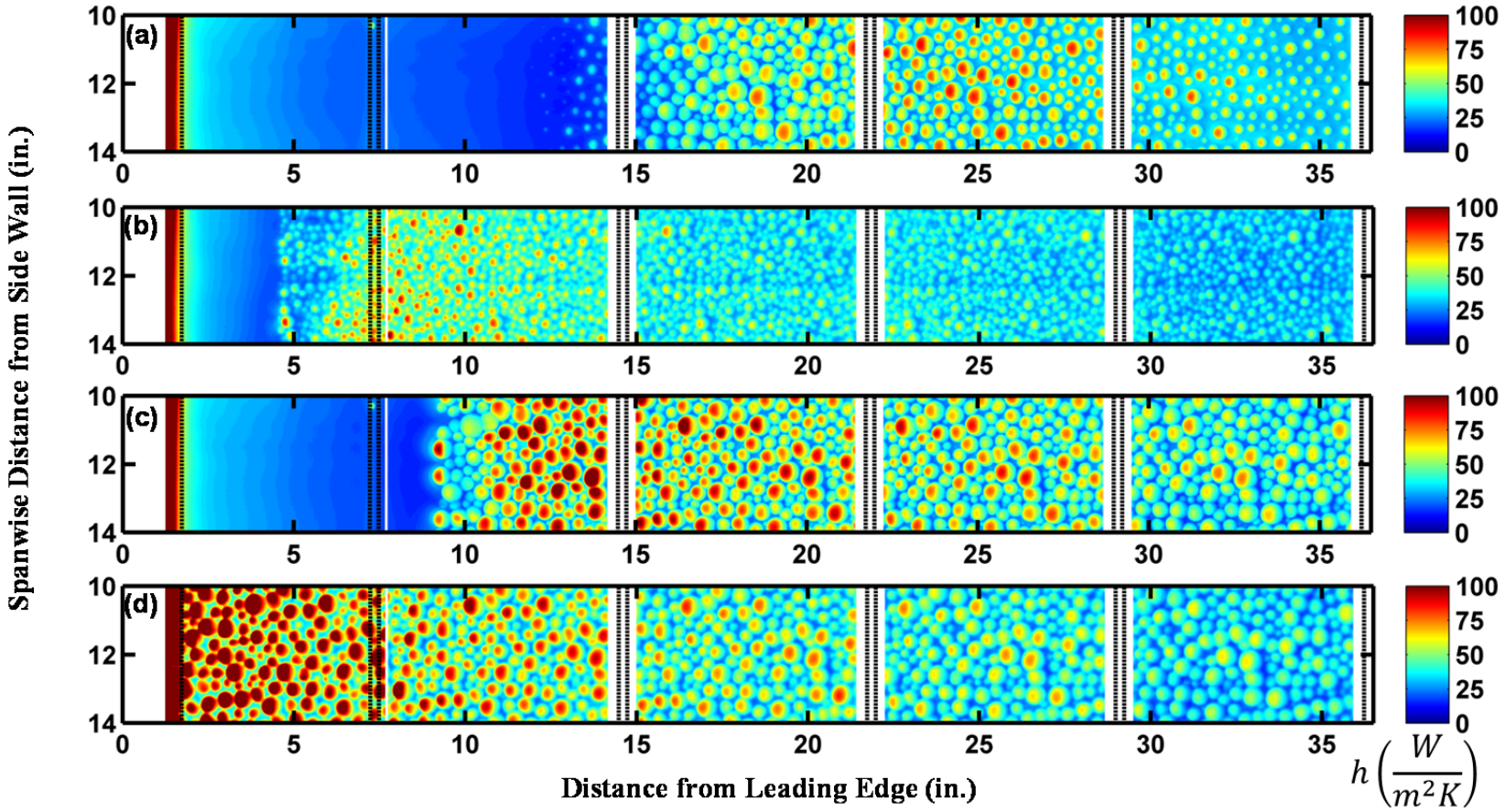


Figure 5.1: Convection coefficient contour maps without ceiling insert for a) 113012.04_IRT surface, b) 053096.01_x10 surface [5], c) 052996.04_x10_SSL surface, and d) 052996.04_x10 surface [5] (flow is from left to right)

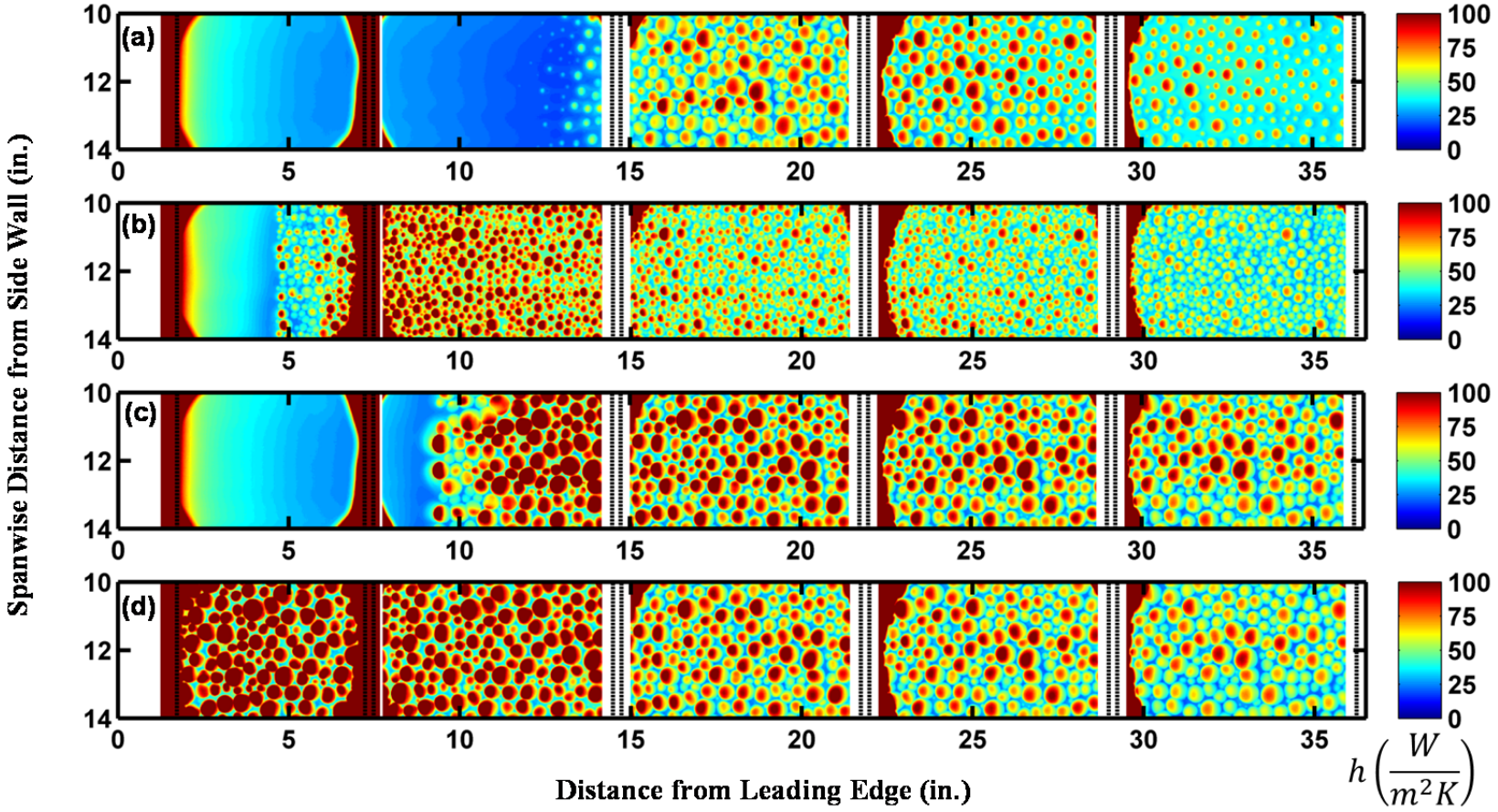


Figure 5.2: Convection coefficient contour maps with ceiling insert for a) 113012.04_IRT surface, b) 053096.01_x10 surface, c) 052996.04_x10_SSL surface, and d) 052996.04_x10 surface (flow is from left to right)

Table 5.1: Convection coefficients for reported cases (units of $W/m^2 \cdot K$)

| Case | 0a | 0b | 0c | 1a | 1b | 2 | 3 | 4 |
|---|---|---|---|---|---|---|---|---|
| Smooth Laminar | | | | | | | | |
| Accelerated | 37.75 ± 2.00 | 30.48 ± 2.05 | 26.54 ± 1.97 | 21.06 ± 0.59 | 18.49 ± 0.50 | 14.05 ± 0.84 | 12.01 ± 0.84 | 7.92 ± 0.79 |
| Smooth Turbulent | | | | | | | | |
| Accelerated | 92.39 ± 7.30 | 57.60 ± 0.41 | 47.36 ± 1.84 | 37.34 ± 1.97 | 34.00 ± 1.82 | 33.35 ± 1.76 | 31.78 ± 2.05 | 29.94 ± 1.92 |
| 113012.04_IRT | | | | | | | | |
| Un-accelerated | 31.50 ± 2.07 | 25.16 ± 1.94 | 21.88 ± 1.81 | 17.46 ± 0.23 | 14.49 ± 0.19 | 44.69 ± 3.00 | 43.87 ± 3.25 | 39.77 ± 2.55 |
| Accelerated | 38.57 ± 1.99 | 30.72 ± 2.05 | 26.93 ± 1.97 | 21.64 ± 0.58 | 18.64 ± 0.27 | 53.58 ± 3.78 | 53.02 ± 4.20 | 46.28 ± 3.11 |
| 053096.01_x10 | | | | | | | | |
| Un-accelerated [5] | 27.78 ± 2.01 | 21.55 ± 1.88 | 31.40 ± 2.09 | 48.85 ± 2.17 | 44.34 ± 2.11 | 35.73 ± 1.91 | 33.57 ± 2.07 | 29.22 ± 1.75 |
| Accelerated | 42.81 ± 1.82 | 32.11 ± 2.10 | 48.84 ± 1.65 | 60.21 ± 3.77 | 57.26 ± 3.69 | 50.87 ± 3.02 | 48.16 ± 3.18 | 42.01 ± 2.65 |
| 052996.04_x10_SSL | | | | | | | | |
| Un-accelerated | 30.64 ± 2.06 | 24.77 ± 1.92 | 20.83 ± 1.75 | 29.58 ± 0.96 | 47.64 ± 2.86 | 47.84 ± 3.20 | 47.33 ± 4.02 | 42.80 ± 3.31 |
| Accelerated | 41.80 ± 1.77 | 32.56 ± 2.04 | 27.95 ± 2.01 | 36.23 ± 1.61 | 57.99 ± 4.40 | 62.83 ± 4.99 | 59.13 ± 5.71 | 61.54 ± 5.49 |
| 052996.04_x10 | | | | | | | | |
| Un-accelerated [5] | 81.23 ± 7.16 | 66.72 ± 4.06 | 62.32 ± 2.47 | 48.87 ± 2.95 | 48.09 ± 3.09 | 45.00 ± 3.05 | 40.77 ± 3.48 | 37.48 ± 2.93 |
| Accelerated | 84.93 ± 8.96 | 76.55 ± 6.67 | 72.73 ± 5.06 | 63.62 ± 4.71 | 59.12 ± 4.25 | 58.26 ± 4.36 | 55.01 ± 4.93 | 55.09 ± 4.72 |

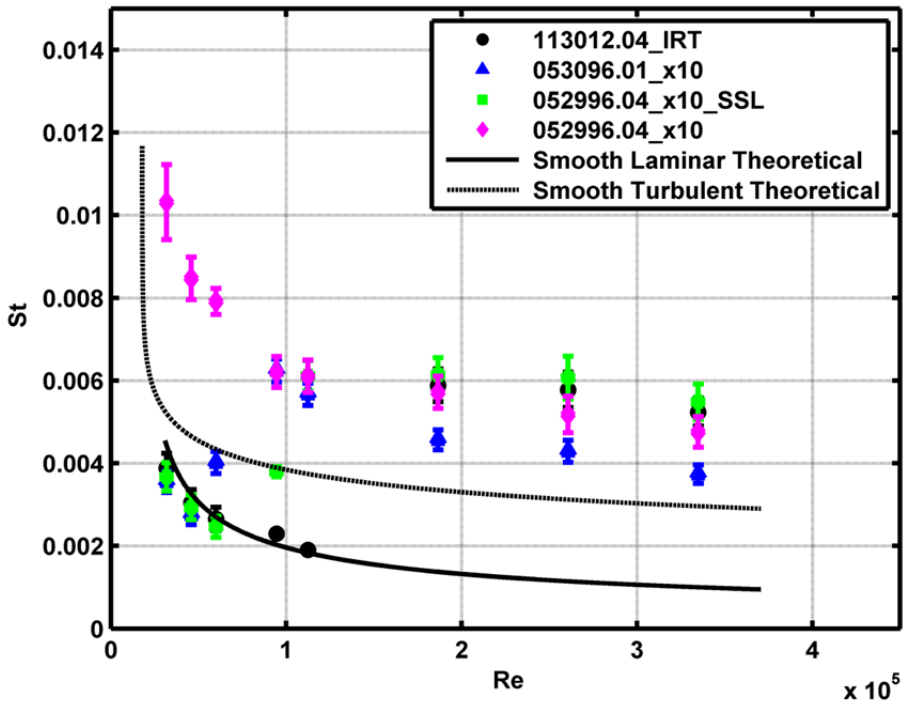


Figure 5.3: Local Stanton number measurements for the rough surfaces in flow with negligible freestream acceleration

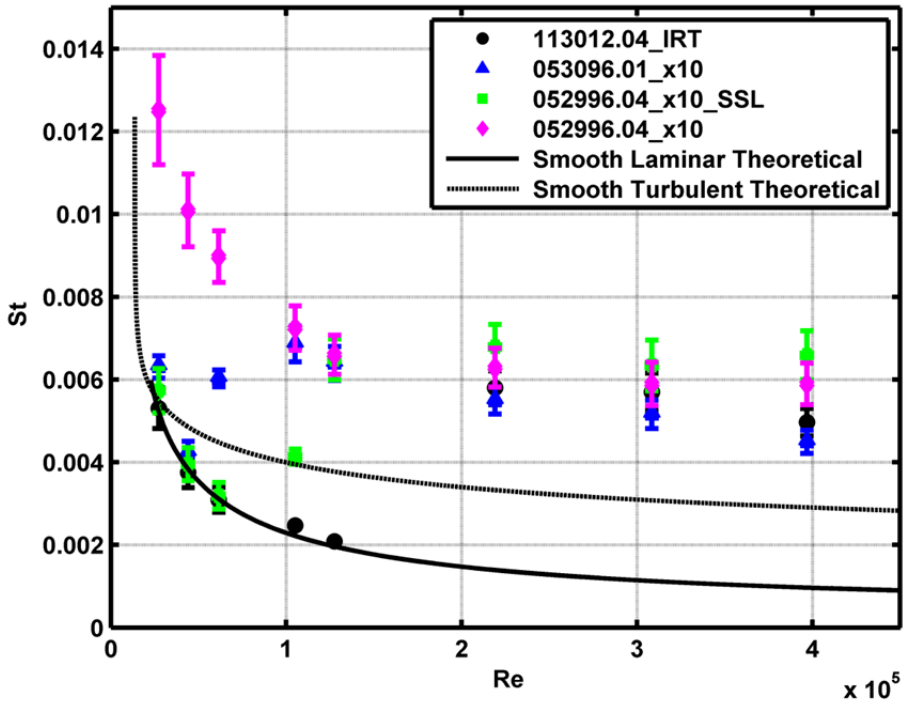


Figure 5.4: Local Stanton number measurements for the rough surfaces in accelerating flow

*Velocity Boundary Layer Characterization*

Figures 5.5-5.10 present the results of the velocity boundary layer measurements at the center of each surface panel in the heated sections for each surface studied. In Figures 5.5-5.10 the left-hand figures are for the cases with negligible freestream acceleration, and the right-hand figures are for the same surfaces with freestream acceleration.

In general, the boundary layers developed as expected. The velocity profiles corresponding to the Smooth Laminar case in Figure 5.5 exhibit laminar behavior. This further validates the assumption that flow over the test plate remains laminar unless it is forced to transition to turbulent. Figure 5.6(a) demonstrates that for the un-accelerated Smooth Turbulent case, the flow at the center of Section 0 has not fully transitioned to turbulent. This is a result of the flow separation and reattachment as it passes over the 2 mm trip at the leading edge of Section 0. However, Figure 5.6(b) demonstrates that the accelerated Smooth Turbulent case does not exhibit the same transitional profile at the center of Section 0. This implies that the flow reattachment length is reduced in the accelerated case relative to negligible flow acceleration case. Figure 5.8(a) demonstrates that at Section 0, the 053096.01_x10 surface exhibits flow acceleration in the smooth zone. This can be attributed to the roughness just downstream of the measurement location.

Figures 5.5(b)-5.10(b) show that there is a variation in the measured freestream velocities from surface to surface. The reduction in freestream velocities compared to the Smooth Laminar case can be attributed to the method of setting the wind tunnel velocity described in Chapter Three, in which the Pitot-static probe installed on the floor of the

test section is used to set the flow condition. Since this method was used, the flow on the bottom of the test plate was matched for each case but the increased resistance of the roughness on the test plate lowered the flow rate traveling through the top part of the wind tunnel test section.

Figures 5.7-5.10 show that there are disturbances in the velocity profiles caused by the roughness elements in the accelerating flow condition that are not apparent in the cases with negligible flow acceleration. This is particularly noticeable for the 052996.04_x10 and 052996.04_x10_SSL surfaces shown in Figures 5.9(b) and 5.10(b), respectively. The 113012.04_IRT case presented in Figure 5.7(b) even shows a disturbance at heated Section 1, which is upstream of the beginning of the roughness for the surface.

To investigate the hypothesis regarding the difference in turbulence intensity for the 113012.04_IRT and 052996.04_x10_SSL surfaces in the presence of freestream acceleration, the measured turbulence intensities of these surfaces at the center of heated Section 2 is given in Figure 5.11. Figure 5.11 shows that at the middle of this heated section, the flow acceleration reduces the maximum turbulence intensities of these surfaces. However, the reduction in turbulence intensity is more significant for the 113012.04_IRT surface than for the 052996.04_x10_SSL surface. While this does not prove the hypothesis, it supports the hypothesis that the later and more gradual increase in roughness characteristics influences the turbulence intensity near the roughness elements and therefore reduces the measured St for the 113012.04_IRT surface.

Figure 5.11 also supports the hypothesis regarding the increase in turbulence intensity for the 053096.01_x10 surface in the presence of freestream acceleration. Figure

5.11 shows that at the middle of heated Section 2 the 053096.01_x10 surface exhibits an incremental increase in turbulence intensity from the case with negligible freestream acceleration to the accelerated case, while the 052996.04_x10 and 052996.04_x10_SSL surfaces show a decrease in turbulence intensities.

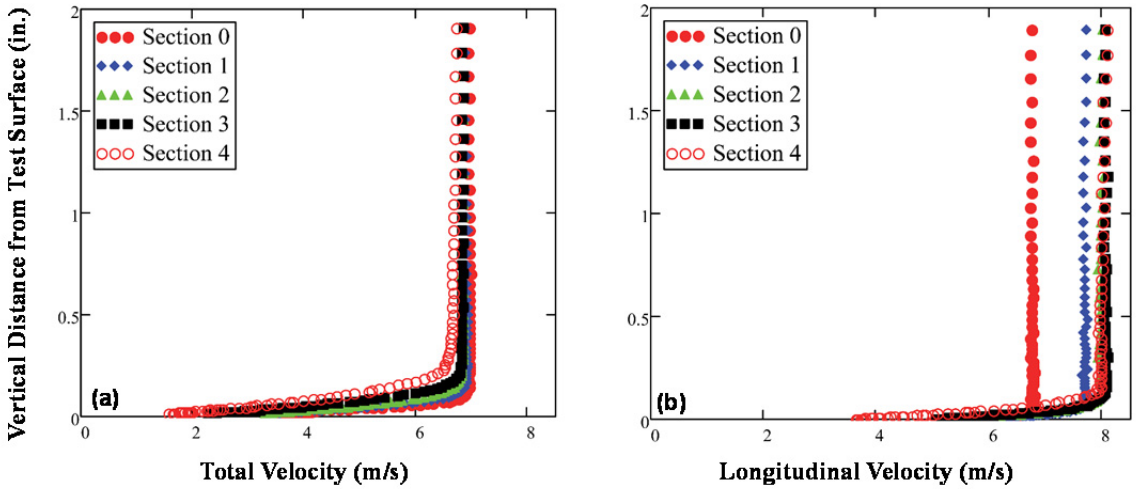


Figure 5.5: Velocity profiles for Smooth Laminar surface at the center of the heated sections for the a) negligible flow acceleration case [4] and b) accelerated flow case

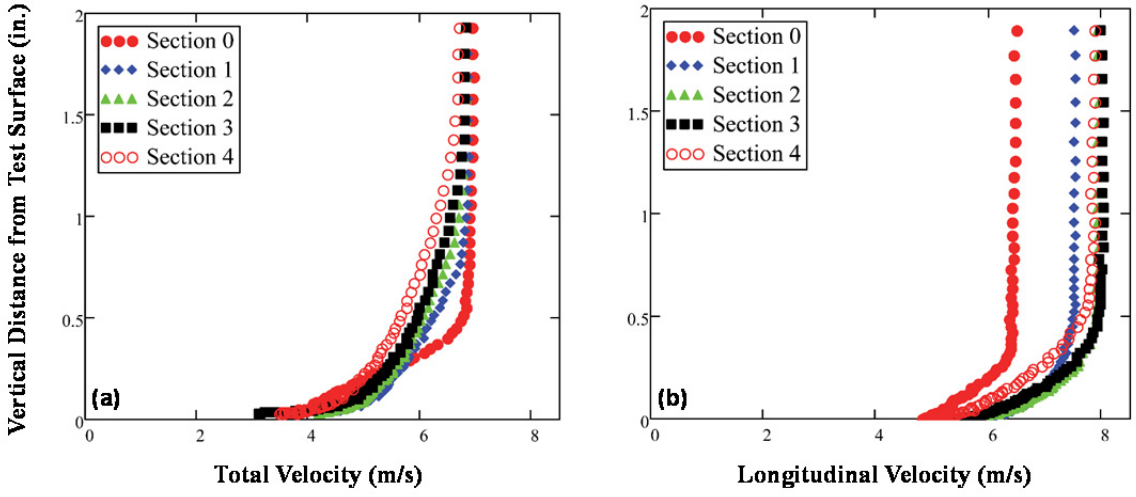


Figure 5.6: Velocity profiles for Smooth Turbulent surface at the center of the heated sections for the a) negligible flow acceleration case [4] and b) accelerated flow case

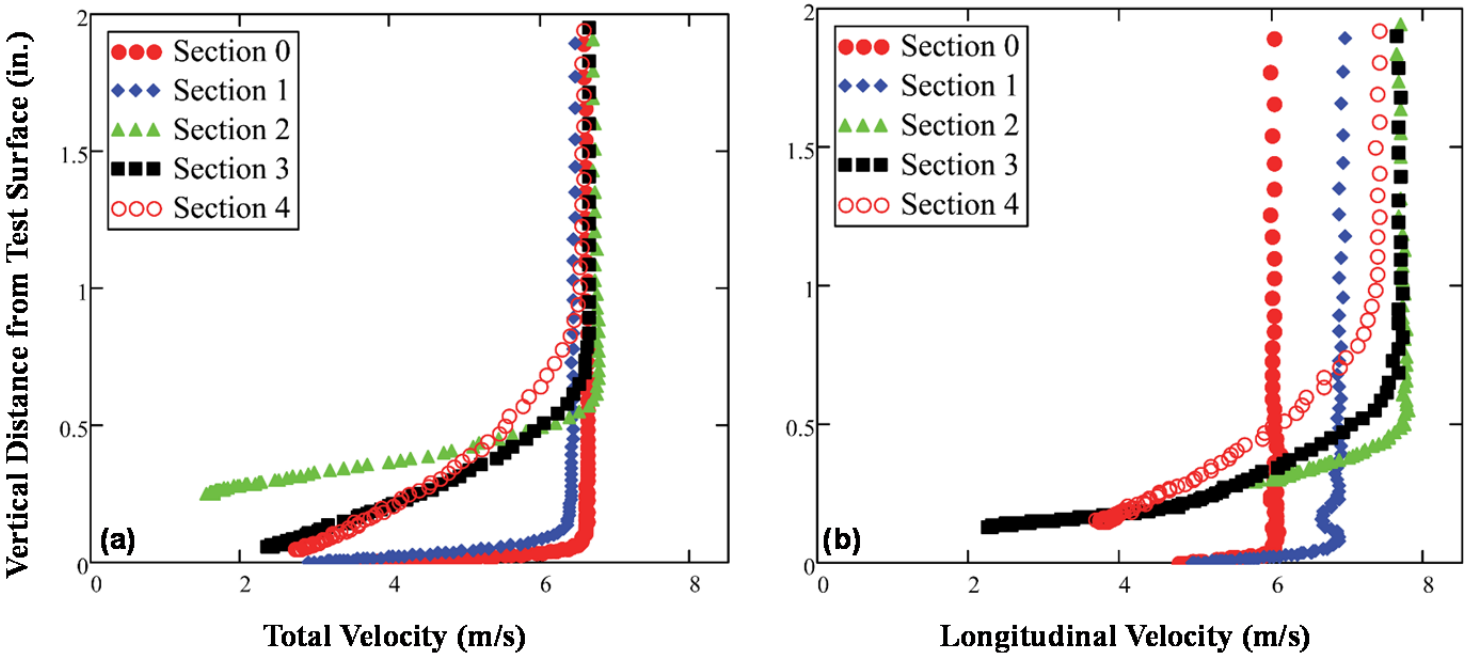


Figure 5.7: Velocity profiles for 113012.04_IRT surface at the center of the heated sections for the a) negligible flow acceleration case and b) accelerated flow case

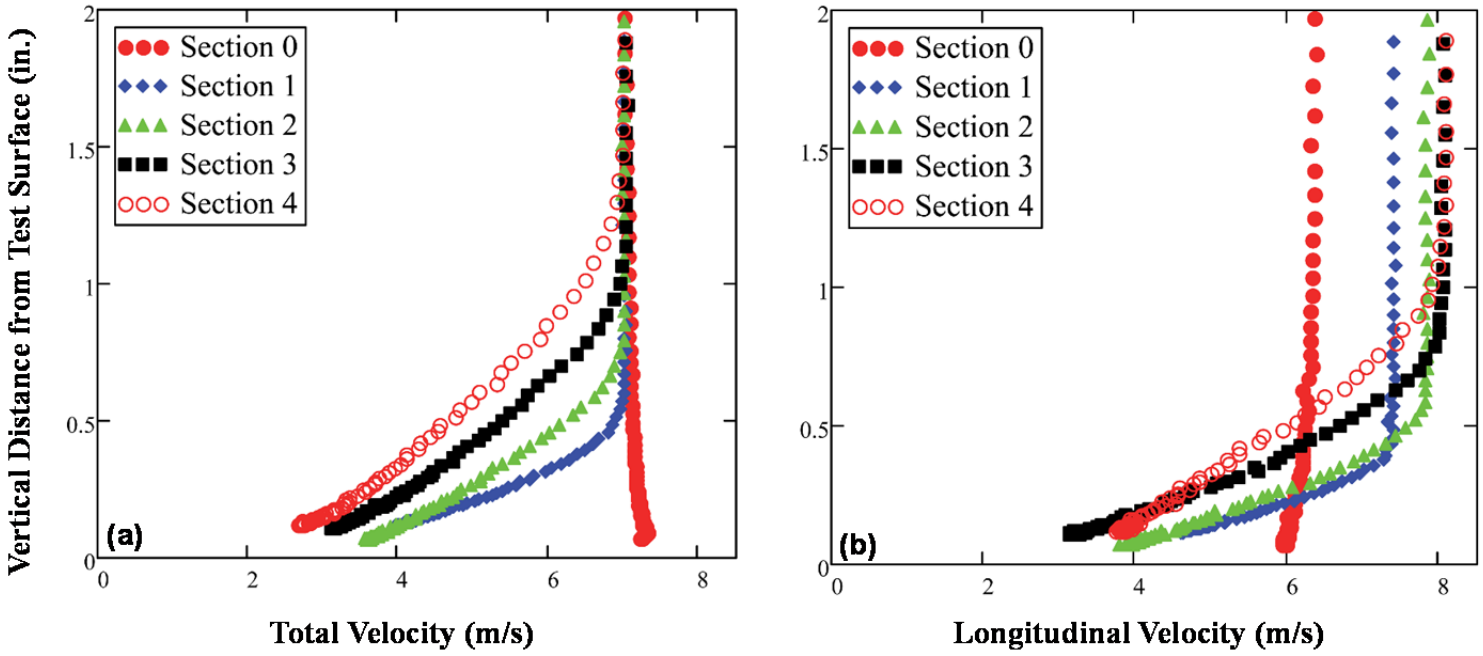


Figure 5.8: Velocity profiles for 053096.01_x10 surface at the center of the heated sections for the a) negligible flow acceleration case [4] and b) accelerated flow case

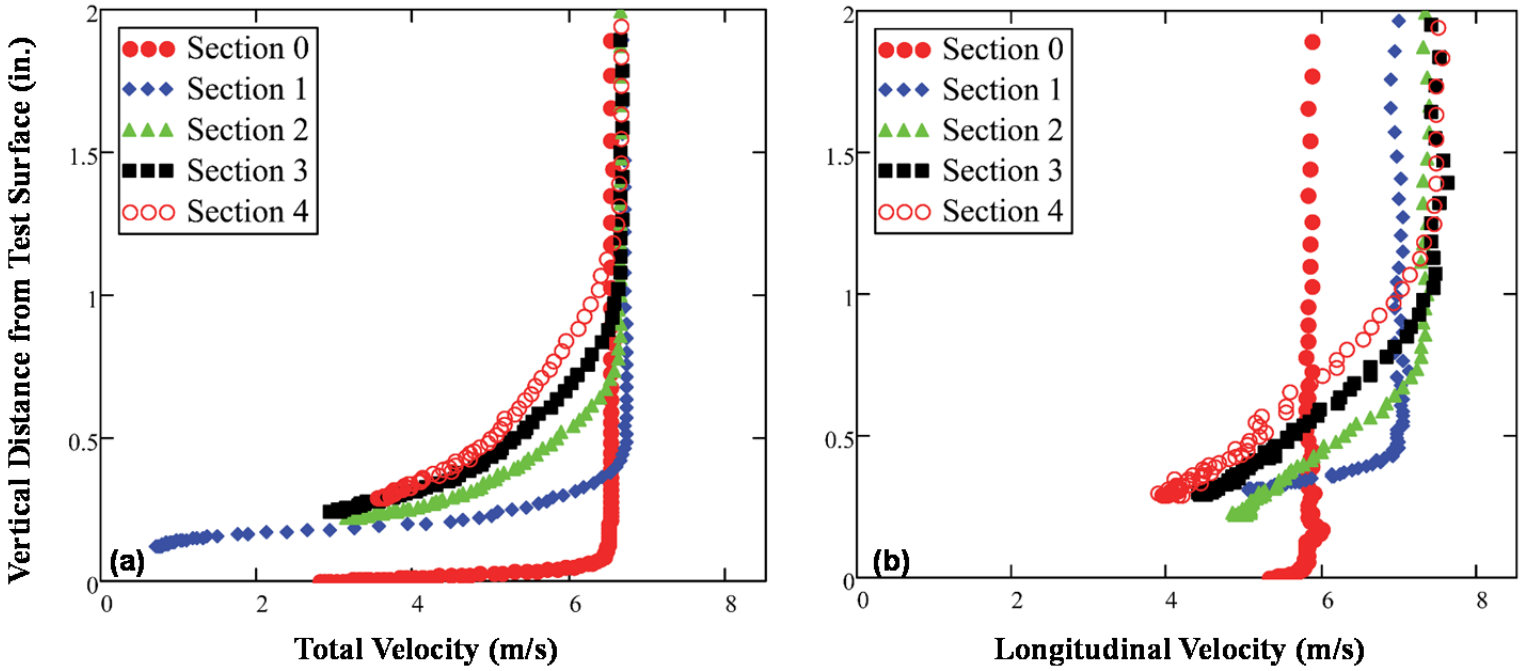


Figure 5.9: Velocity profiles for 052996.04_x10_SSL surface at the center of the heated sections for the a) negligible flow acceleration case and b) accelerated flow case

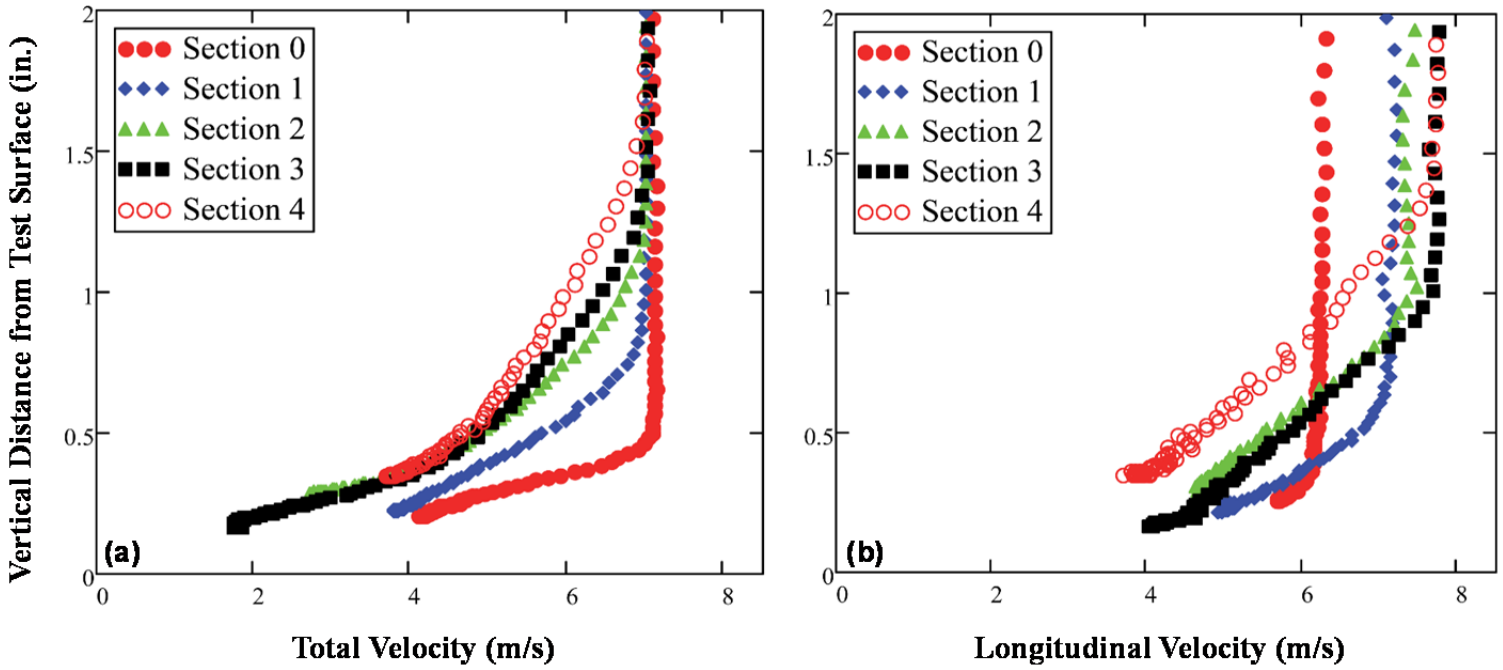


Figure 5.10: Velocity profiles for 052996.04_x10 surface at the center of the heated sections for the a) negligible flow acceleration case [4] and b) accelerated flow case

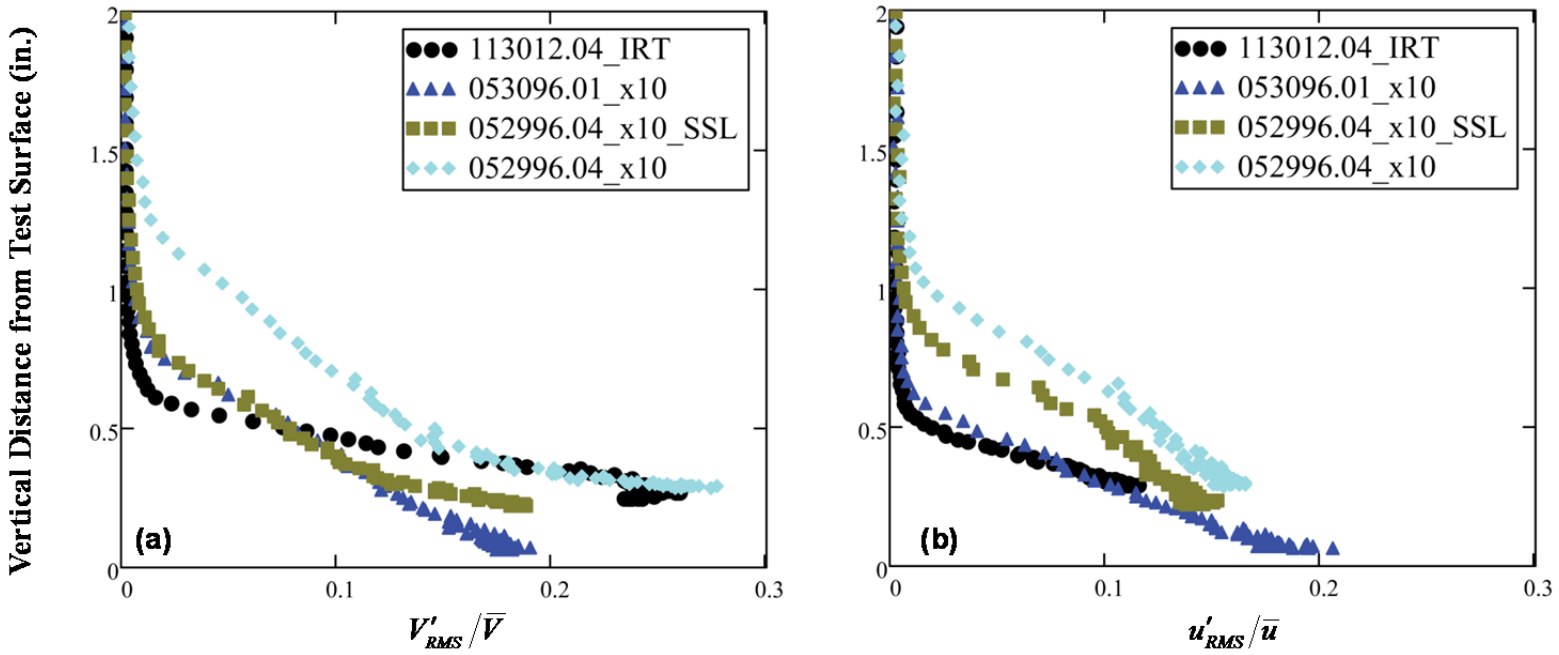


Figure 5.11: Comparison of turbulence intensities for the rough surfaces at the center of heated Section 2 for the a) negligible flow acceleration case [4] and b) accelerated flow case

# CHAPTER SIX

# Conclusions

## *Summary of Work*

A series of experiments were performed to investigate the effects of realistic roughness variations and freestream acceleration on convective heat transfer from surfaces with realistic ice roughness. Four rough surfaces were tested in this investigation. Three of the surface were based on the historical treatment of ice roughness, which is characterized by an abrupt smooth-to-rough transition and constant roughness properties downstream of the transition. The other surface was based on matching the surface roughness variations measured in the IRT at the NASA Glenn Research Center using laser scanning. The primary findings were:

- For the rough surfaces with constant properties in the flow direction (i.e. 052996.04_x10, 052996.04_x10_SSL, and 053096.01_x10 surfaces), the accelerated flow cases exhibited St enhancement values up to 20% relative to the cases with negligible flow acceleration.
- For the surfaces with similar roughness properties in heated Section 2 (i.e. 052996.04_x10, 052996.04_x10_SSL, and 113012.04_IRT), the differences in the measured convection coefficients were not discernable for these surfaces downstream of the location of the maximum roughness on the 113012.04_IRT surface for a flow condition with negligible freestream acceleration.

- For the surfaces with similar roughness properties in heated Section 2, there was a difference between the measured convection coefficients for a flow condition with freestream acceleration. The surface with the more realistic roughness variation exhibited lower convection coefficients. An explanation for this is that interaction of the pressure gradient with the gradual increase in surface roughness leads to lower turbulence intensities in the flow near the roughness elements. Consequently, the measured convection coefficients are lower for this surface.

### *Future Work*

Future research efforts will continue to isolate different aspects of realistic ice roughness in an attempt to improve upon the characterization of convective enhancement in LEWICE. This can be done by 1) changing the roughness element shapes from hemispherical to conical and 2) modeling/investigating the Stefan condition. The investigation performed by McClain et al. [6] showed that the ice roughness elements can be better characterized through the use of cones. Because of the local freezing of liquid water (Stefan condition), the surface of the ice roughness exhibits essentially a constant temperature acting as a surface with near infinite thermal conductivity even though ice in isolation has a relatively low thermal conductivity. A constant surface temperature can be modeled by employing surfaces machined from high thermal conductivity metals for the surface panels.

# APPENDICES

# APPENDIX A

## Sample MATLAB Script

This Appendix provides the MATLAB script used to reduce the data from the convection tests. This code in particular was used to reduce the experimental data for the Smooth Turbulent surface in accelerated flow.

```
% Data Analysis (Smooth Turbulent Constant)
% Steady state convective heat transfer test
%Date: 03/09/14

clear all
close all
clc

%% Constants %%%%%%%%%%%%%%%%%%%%%%%%%%%%%%%%%%%%%%%%%%%%%%%%%%%%%%%%%%%%
% Pixel area [m^2] (0.02" x 0.02")
A_p = 2.58064e-7;
% Total heated area [m^2] (5.5in X 6.375in and 7in X 6.375in)
A_t = [0.02262092, 0.02879026-.002, 0.02879026, 0.02879026,
0.02879026];
% Plexiglas thickness [m]
t_p = 0.018288;
% Plexglas thermal conductivity [W/mK]
k_p = 0.205;
% Unheated started length [in]
zeta = 1.7285;
% Surface emissivity (flat black spray paint)
eps = 0.95;
% Stefan-Boltzman constant [W/m^2K^4]
sig = 0.0000000567;
% Conduction term correction coefficients
c_0 = .9;
c_1 = .9;
c_2 = 1.05;
c_3 = 1.1;
c_4 = 1.05;
%% Set up the imaging grid in real coordinates %%%%%%%%%%%%%%%%%%%%%%%
% Pixel to inch conversions were determined by using the screw holes
% visible in the IR images of heated section 0
IPP = 4/200; % [inch/pixel]
PPI = 200/4; % [pixel/inch]

x_ref  = 305; % reference pixel (screw hole centerline)
x_span = 320; % pixel span in x-axis
```

```
% Heated section 0 x-direction grid [in]
x_0_start = 7.3535 - x_ref*IPP;
x_0_end   = 7.3535 + (x_span - x_ref)*IPP;
x_0       = linspace(x_0_start, x_0_end, x_span);

% Heated section 1 x-direction grid [in]
x_1_start = 13.8535 - x_ref*IPP;
x_1_end   = 13.8535 + (x_span - x_ref)*IPP;
x_1       = linspace(x_1_start, x_1_end, x_span);

% Heated section 2 x-direction grid [in]
x_2_start = 21.1035 - x_ref*IPP;
x_2_end   = 21.1035 + (x_span - x_ref)*IPP;
x_2       = linspace(x_2_start, x_2_end, x_span);

% Heated section 3 x-direction grid [in]
x_3_start = 28.3535 - x_ref*IPP;
x_3_end   = 28.3535 + (x_span - x_ref)*IPP;
x_3       = linspace(x_3_start, x_3_end, x_span);

% Heated section 4 x-direction grid [in]
x_4_start = 35.6035 - x_ref*IPP;
x_4_end   = 35.6035 + (x_span - x_ref)*IPP;
x_4       = linspace(x_4_start, x_4_end, x_span);

y_ref  = 24;  % reference pixel (top screw hole centerline)
y_span = 256; % pixel span in y-axis

% Universal y-direction grid
y_start = 10 - y_ref*IPP;
y_end   = 10 + (y_span - y_ref)*IPP;
y       = linspace(y_start, y_end, y_span);

%% Import IR image data %%%%%%%%%%%%%%%%%%%%%%%%%%%%%%%%%%%%%%%%%%%%%%%%%%%%
% Images were previously analyzed and averaged using a seperate MATLAB
% function. Temperatures are converted from C to K
% _Cal = calibration and _SS = steady state
% Heated section 0
Pos_0_Cal = dlmread('Pos_0_Cal.txt');
Pos_0_SS = dlmread('Pos_0_SS.txt');
Pos_0_Cal = Pos_0_Cal + 273.15;
Pos_0_SS = Pos_0_SS + 273.15;

% Heated section 1
Pos_1_Cal = dlmread('Pos_1_Cal.txt');
Pos_1_SS = dlmread('Pos_1_SS.txt');
Pos_1_Cal = Pos_1_Cal + 273.15;
Pos_1_SS = Pos_1_SS + 273.15;

% Heated section 2
Pos_2_Cal = dlmread('Pos_2_Cal.txt');
Pos_2_SS = dlmread('Pos_2_SS.txt');
Pos_2_Cal = Pos_2_Cal + 273.15;
Pos_2_SS = Pos_2_SS + 273.15;
```

```
% Heated section 3
Pos_3_Cal = dlmread('Pos_3_Cal.txt');
Pos_3_SS = dlmread('Pos_3_SS.txt');
Pos_3_Cal = Pos_3_Cal + 273.15;
Pos_3_SS = Pos_3_SS + 273.15;

% Heated section 4
Pos_4_Cal = dlmread('Pos_4_Cal.txt');
Pos_4_SS = dlmread('Pos_4_SS.txt');
Pos_4_Cal = Pos_4_Cal + 273.15;
Pos_4_SS = Pos_4_SS + 273.15;

%% Import the LABVIEW data %%%%%%%%%%%%%%%%%%%%%%%%%%%%%%%%%%%%%%%%%%%%%%%%
% Raw data from LABVIEW generated text file
rawdata = importdata('052314.txt');
% Indices where calibration images were taken for each heated section
Cal_ind = [36,41,46,50,54];
% Indices where steady state images were taken for each section
SS_ind = [2717,2721,2726,2730,2733];

% Break rawdata into the calibration and steady state data only and
% write to text file for use in Mathcad
avg_data = [rawdata.data(Cal_ind,:) ; rawdata.data(SS_ind,:)];
dlmwrite('Stead_State_Data.txt',avg_data)
% Column indices with power data for each heated section
E_ind = [36, 37, 38, 39]; % voltage
I_ind = [40, 41, 42, 43]; % current

% Extract voltage for sections 0-3 at steady state [V]
for i = 1:4
    E(i) = avg_data(i+5, E_ind(i));
end
E(5) = 6.05; % Manually input voltage for section 4

% Extract current for sections 0-3 at steady state [A]
for i = 1:4
    I(i) = avg_data(i+5, I_ind(i))-rawdata.data(1,I_ind(i));
end
I(1) = I(1)*2; % Apply current transducer factor for section 0
I(5) = 2.61;  % Manually input current for section 4

% Inlet air pressure
P = avg_data(:,53); % [Pa]

% Inlet air relative humidity
RH = avg_data(:,54); % [%]

%% Thermocouple values at calibration %%%%%%%%%%%%%%%%%%%%%%%%%%%%%%%%%%%%
% Subsurface and underplate TCs, converted to K
TC0_Cal = avg_data(1,2) + 273.15;   TC8_Cal = avg_data(1,10)  + 273.15;
TC1_Cal = avg_data(1,3) + 273.15;   TC9_Cal = avg_data(1,11)  + 273.15;
TC2_Cal = avg_data(1,4) + 273.15;   TC10_Cal = avg_data(1,12) + 273.15;
TC3_Cal = avg_data(2,5) + 273.15;   TC11_Cal = avg_data(2,13) + 273.15;
TC4_Cal = avg_data(2,6) + 273.15;   TC12_Cal = avg_data(2,14) + 273.15;
TC5_Cal = avg_data(3,7) + 273.15;   TC13_Cal = avg_data(3,15) + 273.15;
```

```
TC6_Cal = avg_data(4,8) + 273.15;   TC14_Cal = avg_data(4,16) + 273.15;
TC7_Cal = avg_data(5,9) + 273.15;   TC15_Cal = avg_data(5,17) + 273.15;

% Freestream TCs, converted to K
FS_0_Cal = avg_data(1,18) + 273.15;
FS_1_Cal = avg_data(2,18) + 273.15;
FS_2_Cal = avg_data(3,18) + 273.15;
FS_3_Cal = avg_data(4,18) + 273.15;
FS_4_Cal = avg_data(5,18) + 273.15;

% Average freestream temperature (for TC calibration)
FS_Cal_Avg = (FS_0_Cal + FS_1_Cal + FS_2_Cal + FS_3_Cal + FS_4_Cal)/5;

%% Thermocouple values at steady state %%%%%%%%%%%%%%%%%%%%%%%%%%%%%%%
% Subsurface and underplate TCs, converted to K
TC0_SS = avg_data(6,2) + 273.15;     TC8_SS = avg_data(6,10)  + 273.15;
TC1_SS = avg_data(6,3) + 273.15;     TC9_SS = avg_data(6,11)  + 273.15;
TC2_SS = avg_data(6,4) + 273.15;     TC10_SS = avg_data(6,12) + 273.15;
TC3_SS = avg_data(7,5) + 273.15;     TC11_SS = avg_data(7,13) + 273.15;
TC4_SS = avg_data(7,6) + 273.15;     TC12_SS = avg_data(7,14) + 273.15;
TC5_SS = avg_data(8,7) + 273.15;     TC13_SS = avg_data(8,15) + 273.15;
TC6_SS = avg_data(9,8) + 273.15;     TC14_SS = avg_data(9,16) + 273.15;
TC7_SS = avg_data(10,9)+ 273.15;     TC15_SS = avg_data(10,17)+ 273.15;

% Freestream TCs, converted to K
FS_0_SS = avg_data(6,18)  + 273.15;
FS_1_SS = avg_data(7,18)  + 273.15;
FS_2_SS = avg_data(8,18)  + 273.15;
FS_3_SS = avg_data(9,18)  + 273.15;
FS_4_SS = avg_data(10,18) + 273.15;

%Center 50x50 pixels of each IR window for calibration
Pos_0_SS_calibration = mean(mean(Pos_0_Cal(103:153,135:185)));
Pos_1_SS_calibration = mean(mean(Pos_1_Cal(103:153,135:185)));
Pos_2_SS_calibration = mean(mean(Pos_2_Cal(103:153,135:185)));
Pos_3_SS_calibration = mean(mean(Pos_3_Cal(103:153,135:185)));
Pos_4_SS_calibration = mean(mean(Pos_4_Cal(103:153,135:185)));

%% Corrected thermocouple steady state values %%%%%%%%%%%%%%%%%%%%%%%%
% Heated section 0 TCs
TC0_Cor = TC0_SS - (TC0_Cal - Pos_0_SS_calibration);
TC8_Cor = TC8_SS - (TC8_Cal - Pos_0_SS_calibration);
TC1_Cor = TC1_SS - (TC1_Cal - Pos_0_SS_calibration);
TC9_Cor = TC9_SS - (TC9_Cal - Pos_0_SS_calibration);
TC2_Cor = TC2_SS - (TC2_Cal - Pos_0_SS_calibration);
TC10_Cor = TC10_SS - (TC10_Cal - Pos_0_SS_calibration);
FS_0_Cor = FS_0_SS - (FS_0_Cal - Pos_0_SS_calibration);

% Heated section 1 TCs
TC3_Cor = TC3_SS - (TC3_Cal - Pos_1_SS_calibration);
TC11_Cor = TC11_SS - (TC11_Cal - Pos_1_SS_calibration);
TC4_Cor = TC4_SS - (TC4_Cal - Pos_1_SS_calibration);
TC12_Cor = TC12_SS - (TC12_Cal - Pos_1_SS_calibration);
FS_1_Cor = FS_1_SS - (FS_1_Cal - Pos_1_SS_calibration);
```

```
% Heated section 2 TCs
TC5_Cor = TC5_SS - (TC5_Cal - Pos_2_SS_calibration);
TC13_Cor = TC13_SS - (TC13_Cal - Pos_2_SS_calibration);
FS_2_Cor = FS_2_SS - (FS_2_Cal - Pos_2_SS_calibration);

% Heated section 3 TCs
TC6_Cor = TC6_SS - (TC6_Cal - Pos_3_SS_calibration);
TC14_Cor = TC14_SS - (TC14_Cal - Pos_3_SS_calibration);
FS_3_Cor = FS_3_SS - (FS_3_Cal - Pos_3_SS_calibration);

% Heated section 4 TCs
TC7_Cor = TC7_SS - (TC7_Cal - Pos_4_SS_calibration);
TC15_Cor = TC15_SS - (TC15_Cal - Pos_4_SS_calibration);
FS_4_Cor = FS_4_SS - (FS_4_Cal - Pos_4_SS_calibration);

%% Correct IR temperatures for transmissivity %%%%%%%%%%%%%%%%%%%%%%%%
% Apply correction to each heated section pixel map
Pos_0_Cor = Pos_0_SS;
Pos_1_Cor = Pos_1_SS;
Pos_2_Cor = Pos_2_SS;
Pos_3_Cor = Pos_3_SS;
Pos_4_Cor = Pos_4_SS;

%% Calculate air properties %%%%%%%%%%%%%%%%%%%%%%%%%%%%%%%%%%%%%%%%
% Average freestream properties
T_inf = (FS_0_Cor + FS_1_Cor + FS_2_Cor + FS_3_Cor + FS_4_Cor)/5 %[K]
P_inf = mean(P(6:10)) % [Pa]
RH_inf = mean(RH(6:10)) % [%]
U_inf = avg_data(6,57); % [m/s]

% Use the freestream properties above in MathCAD to get air properties
rho_air = 1.1662;   % density [kg/m^3]
mu_air = 1.8995*10^-5; % viscosity [kg/ms]
k_air = 0.0258;   % thermal conductivity [(m*kg)/(K*s^3)]
Pr_air = 0.7455;    % Prandtl number

%% Experimental local convective heat transfer coefficients %%%%%%%%%
FS_avg = (FS_0_Cor+FS_1_Cor+FS_2_Cor+FS_3_Cor+FS_4_Cor)/5;

h_0 = (E(1)*I(1)/A_t(1) - c_0*k_p/t_p*(TC1_Cor - TC9_Cor)  -
sig*eps*(Pos_0_Cor.^4 - FS_avg^4)).*(Pos_0_Cor - FS_avg).^(-1);
h_1 = (E(2)*I(2)/A_t(2) - c_1*k_p/t_p*(TC4_Cor - TC12_Cor) -
sig*eps*(Pos_1_Cor.^4 - FS_avg^4)).*(Pos_1_Cor - FS_avg).^(-1);
h_2 = (E(3)*I(3)/A_t(3) - c_2*k_p/t_p*(TC5_Cor - TC13_Cor) -
sig*eps*(Pos_2_Cor.^4 - FS_avg^4)).*(Pos_2_Cor - FS_avg).^(-1);
h_3 = (E(4)*I(4)/A_t(4) - c_3*k_p/t_p*(TC6_Cor - TC14_Cor) -
sig*eps*(Pos_3_Cor.^4 - FS_avg^4)).*(Pos_3_Cor - FS_avg).^(-1);
h_4 = (E(5)*I(5)/A_t(5) - c_4*k_p/t_p*(TC7_Cor - TC15_Cor) -
sig*eps*(Pos_4_Cor.^4 - FS_avg^4)).*(Pos_4_Cor - FS_avg).^(-1);
```

# APPENDIX B

## Sample Mathcad Sheet

This Appendix provides an example Mathcad sheet used generate the 50x50 pixel area averaged convection coefficients. This sheet also contains the uncertainty analysis for the convection tests.

**Read in data and assign variable names**

**Steady-state data file from MATLAB**

SS_Data := Stead_State_Data.txt

**Heated area power measurements**

Voltage

$$E := \begin{pmatrix} SS_Data_{5,35} \\ SS_Data_{5,35} \\ SS_Data_{5,35} \\ SS_Data_{6,36} \\ SS_Data_{6,36} \\ SS_Data_{7,37} \\ SS_Data_{8,38} \\ 6.05 \end{pmatrix} V = \begin{pmatrix} 5.82 \\ 5.82 \\ 5.82 \\ 5.86 \\ 5.86 \\ 5.97 \\ 6.18 \\ 6.05 \end{pmatrix} V$$

Current

$$I := \begin{bmatrix} 2\cdot(SS_Data_{5,39} - SS_Data_{0,39}) \\ 2\cdot(SS_Data_{5,39} - SS_Data_{0,39}) \\ 2\cdot(SS_Data_{5,39} - SS_Data_{0,39}) \\ SS_Data_{6,40} - SS_Data_{1,40} \\ SS_Data_{6,40} - SS_Data_{1,40} \\ SS_Data_{7,41} - SS_Data_{2,41} \\ SS_Data_{8,42} - SS_Data_{3,42} \\ 2.61 \end{bmatrix} A = \begin{pmatrix} 2.1 \\ 2.1 \\ 2.1 \\ 2.65 \\ 2.65 \\ 2.64 \\ 2.75 \\ 2.61 \end{pmatrix} A$$

**Heated area measurements**

Heated area width and length

$$W_{ha} := \begin{pmatrix} 6.375 \\ 6.375 \\ 6.375 \\ 6.375 \\ 6.375 \\ 6.375 \\ 6.375 \\ 6.375 \end{pmatrix} in \qquad L_{ha} := \begin{pmatrix} 5.5 \\ 5.5 \\ 5.5 \\ 7 \\ 7 \\ 7 \\ 7 \\ 7 \end{pmatrix} in$$

$$A_t := \overrightarrow{(W_{ha} \cdot L_{ha})} = \begin{pmatrix} 35.06 \\ 35.06 \\ 35.06 \\ 44.62 \\ 44.62 \\ 44.62 \\ 44.62 \\ 44.62 \end{pmatrix} \cdot in^2$$

**Plexiglas properties**

Thickness

$$t_p := \begin{pmatrix} 0.72 \\ 0.72 \\ 0.72 \\ 0.72 \\ 0.72 \\ 0.72 \\ 0.72 \\ 0.72 \end{pmatrix} in$$

Thermal conductivity

$$k_p := 0.205 \frac{W}{m \cdot K}$$

$$c_c := \begin{pmatrix} 0.9 \\ 0.9 \\ 0.9 \\ 0.9 \\ 0.9 \\ 1.05 \\ 1.1 \\ 1.05 \end{pmatrix}$$

**Radiation constants**

Surface emissivity

$\varepsilon := 0.95$

Stefan-Boltzman constant

$\sigma := 5.67 \times 10^{-8} \frac{W}{m^2 \cdot K^4}$

**Uncertainty constants**

Student's t value

$t := 2$

Correlated uncertainty

$B_T := 1.4K$

**Section 0 IR temperature maps and 50 pixel by 50 pixel center point submatrix**

SS_0_raw := Pos_0_SS.txt

Cal_0_raw := Pos_0_Cal.txt

SS_0a := submatrix(SS_0_raw, 102, 151, 65, 114) °C

SS_0b := submatrix(SS_0_raw, 102, 151, 134, 183) °C

SS_0c := submatrix(SS_0_raw, 102, 151, 203, 252) °C

Cal_0a := submatrix(Cal_0_raw, 102, 151, 65, 114) °C

Cal_0b := submatrix(Cal_0_raw, 102, 151, 134, 183) °C

Cal_0c := submatrix(Cal_0_raw, 102, 151, 203, 252) °C

**Section 1 IR temperature maps and 50 pixel by 50 pixel center point submatrix**

SS_1_raw := Pos_1_SS.txt

Cal_1_raw := Pos_1_Cal.txt

SS_1a := submatrix(SS_1_raw, 102, 151, 47, 96) °C

SS_1b := submatrix(SS_1_raw, 102, 151, 134, 183) °C

Cal_1a := submatrix(Cal_1_raw, 102, 151, 47, 96) °C

Cal_1b := submatrix(Cal_1_raw, 102, 151, 134, 183) °C

**Section 2 IR temperature maps and 50 pixel by 50 pixel center point submatrix**

SS_2_raw := Pos_2_SS.txt

Cal_2_raw := Pos_2_Cal.txt

SS_2 := submatrix(SS_2_raw, 102, 151, 134, 183) °C

Cal_2 := submatrix(Cal_2_raw, 102, 151, 134, 183) °C

**Section 3 IR temperature maps and 50 pixel by 50 pixel center point submatrix**

SS_3_raw := Pos_3_SS.txt

Cal_3_raw := Pos_3_Cal.txt

SS_3 := submatrix(SS_3_raw, 102, 151, 134, 183) °C

Cal_3 := submatrix(Cal_3_raw, 102, 151, 134, 183) °C

**Section 4 IR temperature maps and 50 pixel by 50 pixel center point submatrix**

SS_4_raw := Pos_4_SS.txt

Cal_4_raw := Pos_4_Cal.txt

$SS_4 := submatrix(SS_4_raw, 102, 151, 134, 183)$ °C

$Cal_4 := submatrix(Cal_4_raw, 102, 151, 134, 183)$ °C

**Subsurface, under plate, and freestream thermocouple measurements**

calibration steady state

$$T_{SS_raw} := \begin{pmatrix} SS_Data_{0,1} & SS_Data_{5,1} \\ SS_Data_{0,2} & SS_Data_{5,2} \\ SS_Data_{0,3} & SS_Data_{5,3} \\ SS_Data_{1,4} & SS_Data_{6,4} \\ SS_Data_{1,5} & SS_Data_{6,5} \\ SS_Data_{2,6} & SS_Data_{7,6} \\ SS_Data_{3,7} & SS_Data_{8,7} \\ SS_Data_{4,8} & SS_Data_{9,8} \end{pmatrix} °C$$

calibration steady state

$$T_{UP_raw} := \begin{pmatrix} SS_Data_{0,9} & SS_Data_{5,9} \\ SS_Data_{0,10} & SS_Data_{5,10} \\ SS_Data_{0,11} & SS_Data_{5,11} \\ SS_Data_{1,12} & SS_Data_{6,12} \\ SS_Data_{1,13} & SS_Data_{6,13} \\ SS_Data_{2,14} & SS_Data_{7,14} \\ SS_Data_{3,15} & SS_Data_{8,15} \\ SS_Data_{4,16} & SS_Data_{9,16} \end{pmatrix} °C$$

calibration steady state

$$T_{inf_raw} := \begin{pmatrix} SS_Data_{0,17} & SS_Data_{5,17} \\ SS_Data_{0,17} & SS_Data_{5,17} \\ SS_Data_{0,17} & SS_Data_{5,17} \\ SS_Data_{1,17} & SS_Data_{6,17} \\ SS_Data_{1,17} & SS_Data_{6,17} \\ SS_Data_{2,17} & SS_Data_{7,17} \\ SS_Data_{3,17} & SS_Data_{8,17} \\ SS_Data_{4,17} & SS_Data_{9,17} \end{pmatrix} °C$$

**Calculate the corrected temperature values**

**Freestream average temperature at calibration**

$T_{0cal} := \text{mean}(\text{mean}(Cal_0b)) = 295.73\,K$

$T_{1cal} := \text{mean}(\text{mean}(Cal_1b)) = 295.72\,K$

$T_{2cal} := \text{mean}(\text{mean}(Cal_2)) = 295.71\,K$

$T_{3cal} := \text{mean}(\text{mean}(Cal_3)) = 295.75\,K$

$T_{4cal} := \text{mean}(\text{mean}(Cal_4)) = 295.76\,K$

Create a calibration matrix

$$T_{cal} := \begin{pmatrix} T_{0cal} \\ T_{0cal} \\ T_{0cal} \\ T_{1cal} \\ T_{1cal} \\ T_{2cal} \\ T_{3cal} \\ T_{4cal} \end{pmatrix}$$

**Corrected steady state temperatures for subsurface, under plate, and freestream thermocouples**

$$T_{SS} := T_{SS_raw}^{\langle 1 \rangle} - \left( T_{SS_raw}^{\langle 0 \rangle} - T_{cal} \right) = \begin{pmatrix} 310.53 \\ 311.99 \\ 313.22 \\ 316.12 \\ 317.73 \\ 314.98 \\ 317.9 \\ 317.93 \end{pmatrix} K$$

Subsurface temperature

$$T_{UP} := T_{UP_raw}^{\langle 1 \rangle} - \left(T_{UP_raw}^{\langle 0 \rangle} - T_{cal}\right) = \begin{pmatrix} 295.91 \\ 296.62 \\ 297.32 \\ 298.39 \\ 298.65 \\ 299.44 \\ 300.64 \\ 300.88 \end{pmatrix} K$$

Under the plate temperature

$$T_{\infty} := T_{inf_raw}^{\langle 1 \rangle} - \left(T_{inf_raw}^{\langle 0 \rangle} - T_{cal}\right) = \begin{pmatrix} 295.22 \\ 295.22 \\ 295.22 \\ 295.1 \\ 295.1 \\ 295.2 \\ 295.29 \\ 295.15 \end{pmatrix} K$$

Freestream temperature

**Corrected IR temperture measurement, averaged in the 50x50 pixel center area**

$$T_{avg} := \begin{pmatrix} \overrightarrow{mean(SS_0a)} \\ \overrightarrow{mean(SS_0b)} \\ \overrightarrow{mean(SS_0c)} \\ \overrightarrow{mean(SS_1a)} \\ \overrightarrow{mean(SS_1b)} \\ \overrightarrow{mean(SS_2)} \\ \overrightarrow{mean(SS_3)} \\ \overrightarrow{mean(SS_4)} \end{pmatrix} = \begin{pmatrix} 299.2 \\ 301.28 \\ 302.35 \\ 303.55 \\ 303.91 \\ 304.48 \\ 305.21 \\ 304.91 \end{pmatrix} K$$

Area averaged IR temperature

**IR temperture standard deviation**

$$S_{Tavg} := \begin{bmatrix} \text{stdev}((SS_0a)) \\ \text{stdev}(SS_0b) \\ \text{stdev}(SS_0c) \\ \text{stdev}(SS_1a) \\ \text{stdev}(SS_1b) \\ \text{stdev}(SS_2) \\ \text{stdev}(SS_3) \\ \text{stdev}(SS_4) \end{bmatrix} = \begin{pmatrix} 0.5 \\ 0.33 \\ 0.14 \\ 0.11 \\ 0.08 \\ 0.05 \\ 0.05 \\ 0.06 \end{pmatrix} K$$

$$T_{inf_avg} := \begin{bmatrix} \frac{\left(T_{\infty 1} + T_{\infty 4} + T_{\infty 5} + T_{\infty 7} + T_{\infty 6}\right)}{5} \\ \frac{\left(T_{\infty 1} + T_{\infty 4} + T_{\infty 5} + T_{\infty 7} + T_{\infty 6}\right)}{5} \\ \frac{\left(T_{\infty 1} + T_{\infty 4} + T_{\infty 5} + T_{\infty 7} + T_{\infty 6}\right)}{5} \\ \frac{\left(T_{\infty 1} + T_{\infty 4} + T_{\infty 5} + T_{\infty 7} + T_{\infty 6}\right)}{5} \\ \frac{\left(T_{\infty 1} + T_{\infty 4} + T_{\infty 5} + T_{\infty 7} + T_{\infty 6}\right)}{5} \\ \frac{\left(T_{\infty 1} + T_{\infty 4} + T_{\infty 5} + T_{\infty 7} + T_{\infty 6}\right)}{5} \\ \frac{\left(T_{\infty 1} + T_{\infty 4} + T_{\infty 5} + T_{\infty 7} + T_{\infty 6}\right)}{5} \\ \frac{\left(T_{\infty 1} + T_{\infty 4} + T_{\infty 5} + T_{\infty 7} + T_{\infty 6}\right)}{5} \end{bmatrix}$$

**Calculated average convective heat transfer coefficients**

$$h_{avg}\left(E, I, A_t, k_p, t_p, T_{SS}, T_{UP}, \varepsilon, \sigma, T_{inf_avg}, T_{avg}, c_c\right) := \overrightarrow{\left[ \frac{\frac{E \cdot I}{A_t} - \frac{c_c \cdot k_p}{t_p} \cdot \left(T_{SS} - T_{UP}\right) - \varepsilon \cdot \sigma \cdot \left(T_{avg}^{\ 4} - T_{inf_avg}^{\ 4}\right)}{\left(T_{avg} - T_{inf_avg}\right)} \right]}$$

$$h := h_{avg}\left(E, I, A_t, k_p, t_p, T_{SS}, T_{UP}, \varepsilon, \sigma, T_{inf_avg}, T_{avg}, c_c\right) = \begin{pmatrix} 92.39 \\ 57.6 \\ 47.36 \\ 37.34 \\ 34 \\ 33.35 \\ 31.78 \\ 29.94 \end{pmatrix} \cdot \frac{W}{m^2 K}$$

Calculated convective heat transfer coefficients

**Uncertainty components for voltage**

**Random and fixed uncertainties**

$$U_{E_rand} := \begin{pmatrix} SS_Data_{5,43} \\ SS_Data_{5,43} \\ SS_Data_{5,43} \\ SS_Data_{6,44} \\ SS_Data_{6,44} \\ SS_Data_{7,45} \\ SS_Data_{8,46} \\ 0 \end{pmatrix} V = \begin{pmatrix} 9.22 \times 10^{-5} \\ 9.22 \times 10^{-5} \\ 9.22 \times 10^{-5} \\ 9.79 \times 10^{-5} \\ 9.79 \times 10^{-5} \\ 9.03 \times 10^{-5} \\ 1.11 \times 10^{-4} \\ 0 \end{pmatrix} V$$

$$U_{E_fixed} := \begin{pmatrix} 0.03\% \cdot E_0 \\ 0.03\% \cdot E_1 \\ 0.03\% \cdot E_2 \\ 0.03\% \cdot E_3 \\ 0.03\% \cdot E_4 \\ 0.03\% \cdot E_5 \\ 0.03\% \cdot E_6 \\ 0.25\% \cdot E_7 \end{pmatrix} = \begin{pmatrix} 1.74 \times 10^{-3} \\ 1.74 \times 10^{-3} \\ 1.74 \times 10^{-3} \\ 1.76 \times 10^{-3} \\ 1.76 \times 10^{-3} \\ 1.79 \times 10^{-3} \\ 1.85 \times 10^{-3} \\ 0.02 \end{pmatrix} V$$

**Total uncertainty**

$$U_E := \sqrt{U_{E_rand}^2 + U_{E_fixed}^2} = \begin{pmatrix} 1.75 \times 10^{-3} \\ 1.75 \times 10^{-3} \\ 1.75 \times 10^{-3} \\ 1.76 \times 10^{-3} \\ 1.76 \times 10^{-3} \\ 1.79 \times 10^{-3} \\ 1.86 \times 10^{-3} \\ 0.02 \end{pmatrix} V$$

## Uncertainty components for current

### Random and fixed uncertainties

$$U_{I_rand} := \begin{pmatrix} SS_Data_{5,47} \\ SS_Data_{5,47} \\ SS_Data_{5,47} \\ SS_Data_{6,48} \\ SS_Data_{6,48} \\ SS_Data_{7,49} \\ SS_Data_{8,50} \\ 0 \end{pmatrix} A = \begin{pmatrix} 4.38 \times 10^{-4} \\ 4.38 \times 10^{-4} \\ 4.38 \times 10^{-4} \\ 6.89 \times 10^{-4} \\ 6.89 \times 10^{-4} \\ 6.92 \times 10^{-4} \\ 5.3 \times 10^{-4} \\ 0 \end{pmatrix} A$$

$$U_{I_fixed} := \begin{pmatrix} 0.1A \\ 0.1A \\ 0.1A \\ 0.05A \\ 0.05A \\ 0.05A \\ 0.05A \\ 2.5\% \cdot I_4 \end{pmatrix} = \begin{pmatrix} 0.1 \\ 0.1 \\ 0.1 \\ 0.05 \\ 0.05 \\ 0.05 \\ 0.05 \\ 0.07 \end{pmatrix} A$$

### Total uncertainty

$$U_I := \sqrt{U_{I_rand}^2 + U_{I_fixed}^2} = \begin{pmatrix} 0.100001 \\ 0.100001 \\ 0.100001 \\ 0.0500047 \\ 0.0500047 \\ 0.0500048 \\ 0.0500028 \\ 0.0662756 \end{pmatrix} A$$

## Uncertainty components for heated area and Plexiglas thickness

### Fixed uncertainty for all distance measurements

$$U_{dist_fixed} := \frac{1}{32} in$$

$$U_{At} := \sqrt{\left(U_{dist_fixed} \cdot W_{ha}\right)^2 + \left(U_{dist_fixed} \cdot L_{ha}\right)^2} = \begin{pmatrix} 0.26 \\ 0.26 \\ 0.26 \\ 0.3 \\ 0.3 \\ 0.3 \\ 0.3 \\ 0.3 \end{pmatrix} \cdot in^2$$

**Total uncertainty in thickness**

$$U_{tp} := \begin{pmatrix} U_{dist_fixed} \\ U_{dist_fixed} \\ U_{dist_fixed} \\ U_{dist_fixed} \\ U_{dist_fixed} \\ U_{dist_fixed} \\ U_{dist_fixed} \\ U_{dist_fixed} \end{pmatrix} = \begin{pmatrix} 0.03 \\ 0.03 \\ 0.03 \\ 0.03 \\ 0.03 \\ 0.03 \\ 0.03 \\ 0.03 \end{pmatrix} \cdot in$$

**<u>Uncertainty for thermocouple temperatures</u>**

**Random uncertainties**

calibration steady state

$$U_{TSS_raw} := \begin{pmatrix} SS_Data_{5,18} & SS_Data_{5,18} \\ SS_Data_{0,19} & SS_Data_{5,19} \\ SS_Data_{5,20} & SS_Data_{5,20} \\ SS_Data_{1,21} & SS_Data_{6,21} \\ SS_Data_{1,22} & SS_Data_{6,22} \\ SS_Data_{2,23} & SS_Data_{7,23} \\ SS_Data_{3,24} & SS_Data_{8,24} \\ SS_Data_{4,25} & SS_Data_{9,25} \end{pmatrix} \Delta°C = \begin{pmatrix} 7.36 \times 10^{-3} & 7.36 \times 10^{-3} \\ 4.27 \times 10^{-3} & 4.56 \times 10^{-3} \\ 6.13 \times 10^{-3} & 6.13 \times 10^{-3} \\ 4.59 \times 10^{-3} & 5.22 \times 10^{-3} \\ 4.45 \times 10^{-3} & 4.39 \times 10^{-3} \\ 4.07 \times 10^{-3} & 6.69 \times 10^{-3} \\ 3.97 \times 10^{-3} & 3.8 \times 10^{-3} \\ 5.39 \times 10^{-3} & 4.4 \times 10^{-3} \end{pmatrix} K$$

calibration steady state

$$U_{TUP_raw} := \begin{pmatrix} SS_Data_{0,26} & SS_Data_{5,26} \\ SS_Data_{0,27} & SS_Data_{5,27} \\ SS_Data_{0,28} & SS_Data_{5,28} \\ SS_Data_{1,29} & SS_Data_{6,29} \\ SS_Data_{1,30} & SS_Data_{6,30} \\ SS_Data_{2,31} & SS_Data_{7,31} \\ SS_Data_{3,32} & SS_Data_{8,32} \\ SS_Data_{4,33} & SS_Data_{9,33} \end{pmatrix} \Delta°C = \begin{pmatrix} 5.02 \times 10^{-3} & 5.65 \times 10^{-3} \\ 4.68 \times 10^{-3} & 5.83 \times 10^{-3} \\ 5.36 \times 10^{-3} & 3.3 \times 10^{-3} \\ 6.05 \times 10^{-3} & 4.09 \times 10^{-3} \\ 3.77 \times 10^{-3} & 8.01 \times 10^{-3} \\ 4.36 \times 10^{-3} & 3.28 \times 10^{-3} \\ 5.58 \times 10^{-3} & 6.72 \times 10^{-3} \\ 6.67 \times 10^{-3} & 3.79 \times 10^{-3} \end{pmatrix} K$$

calibration steady state

$$U_{Tinf_raw} := \begin{pmatrix} SS_Data_{0,34} & SS_Data_{5,34} \\ SS_Data_{0,34} & SS_Data_{5,34} \\ SS_Data_{0,34} & SS_Data_{5,34} \\ SS_Data_{1,34} & SS_Data_{6,34} \\ SS_Data_{1,34} & SS_Data_{6,34} \\ SS_Data_{2,34} & SS_Data_{7,34} \\ SS_Data_{3,34} & SS_Data_{8,34} \\ SS_Data_{4,34} & SS_Data_{9,34} \end{pmatrix} \Delta°C = \begin{pmatrix} 7.22 \times 10^{-3} & 7.36 \times 10^{-3} \\ 7.22 \times 10^{-3} & 7.36 \times 10^{-3} \\ 7.22 \times 10^{-3} & 7.36 \times 10^{-3} \\ 5.53 \times 10^{-3} & 7.19 \times 10^{-3} \\ 5.53 \times 10^{-3} & 7.19 \times 10^{-3} \\ 5.73 \times 10^{-3} & 7.26 \times 10^{-3} \\ 6.86 \times 10^{-3} & 6.31 \times 10^{-3} \\ 4.74 \times 10^{-3} & 8.21 \times 10^{-3} \end{pmatrix} K$$

**Uncertainty for IR camera temperatures**

**Random uncertainty**

$$U_{Tavg_rand} := \frac{t \cdot S_{Tavg}}{\sqrt{2500}} = \begin{pmatrix} 0.02 \\ 0.01 \\ 5.72 \times 10^{-3} \\ 4.46 \times 10^{-3} \\ 3.14 \times 10^{-3} \\ 1.85 \times 10^{-3} \\ 1.9 \times 10^{-3} \\ 2.37 \times 10^{-3} \end{pmatrix} K$$

**Total uncertainty**

$$U_{Tavg} := \sqrt{U_{Tavg_rand}^{2} + B_T^{2}} = \begin{pmatrix} 1.4001445 \\ 1.400061 \\ 1.4000117 \\ 1.4000071 \\ 1.4000035 \\ 1.4000012 \\ 1.4000013 \\ 1.400002 \end{pmatrix} K$$

**Total uncertainty in subsurface TC measurements**

$$U_{TSS} := \sqrt{\left(U_{TSS_raw}^{\langle 0 \rangle}\right)^2 + \left(U_{TSS_raw}^{\langle 1 \rangle}\right)^2 + \left(U_{Tavg_rand}\right)^2 + B_T^{\,2}} = \begin{pmatrix} 1.4001832 \\ 1.4000749 \\ 1.4000385 \\ 1.4000244 \\ 1.4000175 \\ 1.4000231 \\ 1.4000121 \\ 1.4000193 \end{pmatrix} K$$

**Total uncertainty in under the plate TC measurements**

$$U_{TUP} := \sqrt{\left(U_{TUP_raw}^{\langle 0 \rangle}\right)^2 + \left(U_{TUP_raw}^{\langle 1 \rangle}\right)^2 + \left(U_{Tavg_rand}\right)^2 + B_T^{\,2}} = \begin{pmatrix} 1.4001648 \\ 1.4000809 \\ 1.4000258 \\ 1.4000262 \\ 1.4000315 \\ 1.4000119 \\ 1.4000285 \\ 1.400023 \end{pmatrix} K$$

**Total uncertainty in freestream TC measurements**

$$U_{T\infty} := \sqrt{\left(U_{Tinf_raw}^{\langle 0 \rangle}\right)^2 + \left(U_{Tavg_rand}\right)^2 + \left(B_T\right)^2} = \begin{pmatrix} 1.4001631 \\ 1.4000796 \\ 1.4000303 \\ 1.400018 \\ 1.4000144 \\ 1.4000129 \\ 1.4000181 \\ 1.40001 \end{pmatrix} K$$

$$U_{T.inf_avg} := \begin{bmatrix} \sqrt{\frac{(U_{T\infty 1})^2}{5} + \frac{(U_{T\infty 4})^2}{5} + \frac{(U_{T\infty 5})^2}{5} + \frac{(U_{T\infty 6})^2}{5} + \frac{(U_{T\infty 7})^2}{5}} \\ \sqrt{\frac{(U_{T\infty 1})^2}{5} + \frac{(U_{T\infty 4})^2}{5} + \frac{(U_{T\infty 5})^2}{5} + \frac{(U_{T\infty 6})^2}{5} + \frac{(U_{T\infty 7})^2}{5}} \\ \sqrt{\frac{(U_{T\infty 1})^2}{5} + \frac{(U_{T\infty 4})^2}{5} + \frac{(U_{T\infty 5})^2}{5} + \frac{(U_{T\infty 6})^2}{5} + \frac{(U_{T\infty 7})^2}{5}} \\ \sqrt{\frac{(U_{T\infty 1})^2}{5} + \frac{(U_{T\infty 4})^2}{5} + \frac{(U_{T\infty 5})^2}{5} + \frac{(U_{T\infty 6})^2}{5} + \frac{(U_{T\infty 7})^2}{5}} \\ \sqrt{\frac{(U_{T\infty 1})^2}{5} + \frac{(U_{T\infty 4})^2}{5} + \frac{(U_{T\infty 5})^2}{5} + \frac{(U_{T\infty 6})^2}{5} + \frac{(U_{T\infty 7})^2}{5}} \\ \sqrt{\frac{(U_{T\infty 1})^2}{5} + \frac{(U_{T\infty 4})^2}{5} + \frac{(U_{T\infty 5})^2}{5} + \frac{(U_{T\infty 6})^2}{5} + \frac{(U_{T\infty 7})^2}{5}} \\ \sqrt{\frac{(U_{T\infty 1})^2}{5} + \frac{(U_{T\infty 4})^2}{5} + \frac{(U_{T\infty 5})^2}{5} + \frac{(U_{T\infty 6})^2}{5} + \frac{(U_{T\infty 7})^2}{5}} \\ \sqrt{\frac{(U_{T\infty 1})^2}{5} + \frac{(U_{T\infty 4})^2}{5} + \frac{(U_{T\infty 5})^2}{5} + \frac{(U_{T\infty 6})^2}{5} + \frac{(U_{T\infty 7})^2}{5}} \end{bmatrix}$$

$$U_{kp} := 0.033 \frac{W}{m \cdot K}$$

## Overall uncertainty in average convective heat transfer coefficients

### Partial derivatives of *h* with respect to each variable

$$\theta_E(E, I, A_t, k_p, t_p, T_{SS}, T_{UP}, \varepsilon, \sigma, T_{inf_avg}, T_{avg}, c_c) := \frac{d}{dE} h_{avg}(E, I, A_t, k_p, t_p, T_{SS}, T_{UP}, \varepsilon, \sigma, T_{inf_avg}, T_{avg}, c_c)$$

$$\theta_I(E, I, A_t, k_p, t_p, T_{SS}, T_{UP}, \varepsilon, \sigma, T_{inf_avg}, T_{avg}, c_c) := \frac{d}{dI} h_{avg}(E, I, A_t, k_p, t_p, T_{SS}, T_{UP}, \varepsilon, \sigma, T_{inf_avg}, T_{avg}, c_c)$$

$$\theta_{At}(E, I, A_t, k_p, t_p, T_{SS}, T_{UP}, \varepsilon, \sigma, T_{inf_avg}, T_{avg}, c_c) := \frac{d}{dA_t} h_{avg}(E, I, A_t, k_p, t_p, T_{SS}, T_{UP}, \varepsilon, \sigma, T_{inf_avg}, T_{avg}, c_c)$$

$$\theta_{tp}(E, I, A_t, k_p, t_p, T_{SS}, T_{UP}, \varepsilon, \sigma, T_{inf_avg}, T_{avg}, c_c) := \frac{d}{dt_p} h_{avg}(E, I, A_t, k_p, t_p, T_{SS}, T_{UP}, \varepsilon, \sigma, T_{inf_avg}, T_{avg}, c_c)$$

$$\theta_{TSS}(E,I,A_t,k_p,t_p,T_{SS},T_{UP},\varepsilon,\sigma,T_{inf_avg},T_{avg},c_c) := \frac{d}{dT_{SS}} h_{avg}(E,I,A_t,k_p,t_p,T_{SS},T_{UP},\varepsilon,\sigma,T_{inf_avg},T_{avg},c_c)$$

$$\theta_{TUP}(E,I,A_t,k_p,t_p,T_{SS},T_{UP},\varepsilon,\sigma,T_{inf_avg},T_{avg},c_c) := \frac{d}{dT_{UP}} h_{avg}(E,I,A_t,k_p,t_p,T_{SS},T_{UP},\varepsilon,\sigma,T_{inf_avg},T_{avg},c_c)$$

$$\theta_{T\infty}(E,I,A_t,k_p,t_p,T_{SS},T_{UP},\varepsilon,\sigma,T_{inf_avg},T_{avg},c_c) := \frac{d}{dT_{inf_avg}} h_{avg}(E,I,A_t,k_p,t_p,T_{SS},T_{UP},\varepsilon,\sigma,T_{inf_avg},T_{avg},c_c)$$

$$\theta_{Tavg}(E,I,A_t,k_p,t_p,T_{SS},T_{UP},\varepsilon,\sigma,T_{inf_avg},T_{avg},c_c) := \frac{d}{dT_{avg}} h_{avg}(E,I,A_t,k_p,t_p,T_{SS},T_{UP},\varepsilon,\sigma,T_{inf_avg},T_{avg},c_c)$$

$$\theta_{kp}(E,I,A_t,k_p,t_p,T_{SS},T_{UP},\varepsilon,\sigma,T_{inf_avg},T_{avg},c_c) := \frac{d}{dk_p} h_{avg}(E,I,A_t,k_p,t_p,T_{SS},T_{UP},\varepsilon,\sigma,T_{inf_avg},T_{avg},c_c)$$

**Calculated uncertainty components**

$$\Psi_E := \left[\overrightarrow{\left(U_E \cdot \theta_E(E,I,A_t,k_p,t_p,T_{SS},T_{UP},\varepsilon,\sigma,T_{inf_avg},T_{avg},c_c)\right)}\right]^2 = \begin{pmatrix} 1.64\times10^{-3} \\ 7.12\times10^{-4} \\ 5.15\times10^{-4} \\ 3.76\times10^{-4} \\ 3.46\times10^{-4} \\ 3.12\times10^{-4} \\ 3.13\times10^{-4} \\ 0.02 \end{pmatrix} \cdot \left(\frac{W}{m^2 K}\right)^2$$

$$\Psi_I := \left[\overrightarrow{\left(U_I \cdot \theta_I(E,I,A_t,k_p,t_p,T_{SS},T_{UP},\varepsilon,\sigma,T_{inf_avg},T_{avg},c_c)\right)}\right]^2 = \begin{pmatrix} 41.17 \\ 17.85 \\ 12.91 \\ 1.48 \\ 1.36 \\ 1.24 \\ 1.15 \\ 2.05 \end{pmatrix} \cdot \left(\frac{W}{m^2 K}\right)^2$$

$$\Psi_{At} := \left[\overrightarrow{\left(U_{At}\cdot\theta_{At}\left(E, I, A_t, k_p, t_p, T_{SS}, T_{UP}, \varepsilon, \sigma, T_{inf_avg}, T_{avg}, c_c\right)\right)}\right]^2 = \begin{pmatrix} 1.02 \\ 0.44 \\ 0.32 \\ 0.18 \\ 0.17 \\ 0.15 \\ 0.15 \\ 0.14 \end{pmatrix} \cdot \left(\frac{W}{m^2 K}\right)^2$$

$$\Psi_{tp} := \left[\overrightarrow{\left(U_{tp}\cdot\theta_{tp}\left(E, I, A_t, k_p, t_p, T_{SS}, T_{UP}, \varepsilon, \sigma, T_{inf_avg}, T_{avg}, c_c\right)\right)}\right]^2 = \begin{pmatrix} 2.55 \\ 1.22 \\ 0.95 \\ 0.86 \\ 0.92 \\ 0.73 \\ 0.85 \\ 0.8 \end{pmatrix} \cdot \left(\frac{W}{m^2 K}\right)^2$$

$$\Psi_{TSS} := \left[\overrightarrow{\left(U_{TSS}\cdot\theta_{TSS}\left(E, I, A_t, k_p, t_p, T_{SS}, T_{UP}, \varepsilon, \sigma, T_{inf_avg}, T_{avg}, c_c\right)\right)}\right]^2 = \begin{pmatrix} 12.43 \\ 5.39 \\ 3.9 \\ 2.85 \\ 2.62 \\ 3.15 \\ 2.97 \\ 2.87 \end{pmatrix} \cdot \left(\frac{W}{m^2 K}\right)^2$$

$$\Psi_{TUP} := \left[\overrightarrow{\left(U_{TUP}\cdot\theta_{TUP}\left(E, I, A_t, k_p, t_p, T_{SS}, T_{UP}, \varepsilon, \sigma, T_{inf_avg}, T_{avg}, c_c\right)\right)}\right]^2 = \begin{pmatrix} 12.43 \\ 5.39 \\ 3.9 \\ 2.85 \\ 2.62 \\ 3.15 \\ 2.97 \\ 2.87 \end{pmatrix} \cdot \left(\frac{W}{m^2 K}\right)^2$$

$$\Psi_{T\infty} := \overrightarrow{\left[\left[\frac{\frac{E\cdot I}{A_t} - \sigma\cdot\varepsilon\cdot\left(T_{avg}^{\ 4} - T_{inf_avg}^{\ 4}\right) + \frac{k_p\cdot\left(T_{UP} - T_{SS}\right)}{t_p}}{\left(T_{avg} - T_{inf_avg}\right)^2} + \frac{4\cdot\sigma\cdot\varepsilon\cdot T_{inf_avg}^{\ 3}}{T_{avg} - T_{inf_avg}}\right]\cdot U_{T.inf_avg}\right]^2} = \begin{pmatrix} 1.07\times10^3 \\ 192.51 \\ 97.28 \\ 45.96 \\ 35.45 \\ 36.04 \\ 30.09 \\ 27.57 \end{pmatrix}\cdot\left(\frac{W}{m^2K}\right)^2$$

$$\Psi_{Tavg} := \left[\overrightarrow{\left(U_{Tavg}\cdot\theta_{Tavg}\left(E, I, A_t, k_p, t_p, T_{SS}, T_{UP}, \varepsilon, \sigma, T_{inf_avg}, T_{avg}, c_c\right)\right)}\right]^2 = \begin{pmatrix} 1.18\times10^3 \\ 213.37 \\ 108.81 \\ 52.68 \\ 41.33 \\ 35.32 \\ 28.06 \\ 26.94 \end{pmatrix}\cdot\left(\frac{W}{m^2K}\right)^2$$

$$\Psi_{kp} := \left[\overrightarrow{\left(U_{kp}\cdot\theta_{kp}\left(E, I, A_t, k_p, t_p, T_{SS}, T_{UP}, \varepsilon, \sigma, T_{inf_avg}, T_{avg}, c_c\right)\right)}\right]^2 = \begin{pmatrix} 35.12 \\ 16.83 \\ 13.03 \\ 11.86 \\ 12.62 \\ 10.04 \\ 11.69 \\ 11.05 \end{pmatrix}\cdot\left(\frac{W}{m^2K}\right)^2$$

**Correlated uncertainty contributions**

$$\Psi_{CU1} := \overrightarrow{\left[\frac{2\theta_{TSS}\left(E, I, A_t, k_p, t_p, T_{SS}, T_{UP}, \varepsilon, \sigma, T_{inf_avg}, T_{avg}, c_c\right)}{\left(\theta_{TUP}\left(E, I, A_t, k_p, t_p, T_{SS}, T_{UP}, \varepsilon, \sigma, T_{inf_avg}, T_{avg}, c_c\right)\cdot B_T^{\ 2}\right)^{-1}}\right]} = \begin{pmatrix} -24.85 \\ -10.77 \\ -7.79 \\ -5.7 \\ -5.25 \\ -6.29 \\ -5.94 \\ -5.74 \end{pmatrix}\cdot\left(\frac{W}{m^2K}\right)^2$$

$$\Psi_{CU2} := \overrightarrow{\left[\frac{2\theta_{TSS}\left(E, I, A_t, k_p, t_p, T_{SS}, T_{UP}, \varepsilon, \sigma, T_{inf_avg}, T_{avg}, c_c\right)}{\left(\theta_{T\infty}\left(E, I, A_t, k_p, t_p, T_{SS}, T_{UP}, \varepsilon, \sigma, T_{inf_avg}, T_{avg}, c_c\right) \cdot B_T^{\,2}\right)^{-1}}\right]} = \begin{pmatrix} -241.17 \\ -67.43 \\ -40.86 \\ -24.24 \\ -20.56 \\ -20.79 \\ -17.97 \\ -17.32 \end{pmatrix} \cdot \left(\frac{W}{m^2 K}\right)^2$$

$$\overrightarrow{\left(\theta_{TSS}\left(E, I, A_t, k_p, t_p, T_{SS}, T_{UP}, \varepsilon, \sigma, T_{inf_avg}, T_{avg}, c_c\right)\right)} = \begin{pmatrix} -2.52 \\ -1.66 \\ -1.41 \\ -1.21 \\ -1.16 \\ -1.27 \\ -1.23 \\ -1.21 \end{pmatrix} \frac{kg}{K^2 \cdot s^3}$$

$$\Psi_{CU3} := \overrightarrow{\left[\frac{2\theta_{TSS}\left(E, I, A_t, k_p, t_p, T_{SS}, T_{UP}, \varepsilon, \sigma, T_{inf_avg}, T_{avg}, c_c\right)}{\left(\theta_{Tavg}\left(E, I, A_t, k_p, t_p, T_{SS}, T_{UP}, \varepsilon, \sigma, T_{inf_avg}, T_{avg}, c_c\right) \cdot B_T^{\,2}\right)^{-1}}\right]} = \begin{pmatrix} 241.74 \\ 67.8 \\ 41.18 \\ 24.51 \\ 20.82 \\ 21.08 \\ 18.25 \\ 17.59 \end{pmatrix} \cdot \left(\frac{W}{m^2 K}\right)^2$$

$$\Psi_{CU4} := \overrightarrow{\left[\frac{2\theta_{TUP}\left(E, I, A_t, k_p, t_p, T_{SS}, T_{UP}, \varepsilon, \sigma, T_{inf_avg}, T_{avg}, c_c\right)}{\left(\theta_{T\infty}\left(E, I, A_t, k_p, t_p, T_{SS}, T_{UP}, \varepsilon, \sigma, T_{inf_avg}, T_{avg}, c_c\right) \cdot B_T^{\,2}\right)^{-1}}\right]} = \begin{pmatrix} 241.17 \\ 67.43 \\ 40.86 \\ 24.24 \\ 20.56 \\ 20.79 \\ 17.97 \\ 17.32 \end{pmatrix} \cdot \left(\frac{W}{m^2 K}\right)^2$$

$$\Psi_{CU5} := \left[ \frac{2\theta_{TUP}\left(E, I, A_t, k_p, t_p, T_{SS}, T_{UP}, \varepsilon, \sigma, T_{inf_avg}, T_{avg}, c_c\right)}{\left(\theta_{Tavg}\left(E, I, A_t, k_p, t_p, T_{SS}, T_{UP}, \varepsilon, \sigma, T_{inf_avg}, T_{avg}, c_c\right) \cdot B_T{}^2\right)^{-1}} \right] = \begin{pmatrix} -241.74 \\ -67.8 \\ -41.18 \\ -24.51 \\ -20.82 \\ -21.08 \\ -18.25 \\ -17.59 \end{pmatrix} \cdot \left( \frac{W}{m^2 K} \right)^2$$

$$\Psi_{CU6} := \left[ \frac{2\theta_{T\infty}\left(E, I, A_t, k_p, t_p, T_{SS}, T_{UP}, \varepsilon, \sigma, T_{inf_avg}, T_{avg}, c_c\right)}{\left(\theta_{Tavg}\left(E, I, A_t, k_p, t_p, T_{SS}, T_{UP}, \varepsilon, \sigma, T_{inf_avg}, T_{avg}, c_c\right) \cdot B_T{}^2\right)^{-1}} \right] = \begin{pmatrix} -2.35 \times 10^3 \\ -424.34 \\ -215.93 \\ -104.18 \\ -81.62 \\ -69.67 \\ -55.26 \\ -53.03 \end{pmatrix} \cdot \left( \frac{W}{m^2 K} \right)^2$$

**Overall uncertainty in h**

$$U_{havg} := \left[ \sqrt{\left( \begin{matrix} \Psi_E + \Psi_I + \Psi_{At} + \Psi_{TSS} + \Psi_{TUP} + \Psi_{T\infty} + \Psi_{Tavg} \cdots \\ + \Psi_{CU1} + \Psi_{CU2} + \Psi_{CU3} + \Psi_{CU4} + \Psi_{CU5} + \Psi_{CU6} \end{matrix} \right)^2} \right]^{\frac{1}{2}} = \begin{pmatrix} 7.2973 \\ 0.41342 \\ 1.84226 \\ 1.9696 \\ 1.81776 \\ 1.75551 \\ 2.04806 \\ 1.91986 \end{pmatrix} \cdot \frac{W}{m^2 K}$$

Percent uncertainty

$$\overrightarrow{\frac{U_{havg}}{h}} = \begin{pmatrix} 7.9 \\ 0.72 \\ 3.89 \\ 5.28 \\ 5.35 \\ 5.26 \\ 6.44 \\ 6.41 \end{pmatrix} \cdot \%$$

$$h_{low} := h - U_{havg} = \begin{pmatrix} 85.09 \\ 57.19 \\ 45.52 \\ 35.37 \\ 32.18 \\ 31.6 \\ 29.74 \\ 28.02 \end{pmatrix} \cdot \frac{W}{m^2 K}$$

$$h_{high} := h + U_{havg} = \begin{pmatrix} 99.69 \\ 58.01 \\ 49.2 \\ 39.31 \\ 35.82 \\ 35.11 \\ 33.83 \\ 31.86 \end{pmatrix} \cdot \frac{W}{m^2 K}$$

$$x := \begin{pmatrix} 3.1035\,\text{in} \\ 4.4785\,\text{in} \\ 5.8535\,\text{in} \\ 9.2285\,\text{in} \\ 10.9785\,\text{in} \\ 18.2285\,\text{in} \\ 25.4785\,\text{in} \\ 32.7285\,\text{in} \end{pmatrix} \qquad h = \begin{pmatrix} 92.39 \\ 57.6 \\ 47.36 \\ 37.34 \\ 34 \\ 33.35 \\ 31.78 \\ 29.94 \end{pmatrix} \frac{\text{kg}}{\text{K}\cdot\text{s}^3}$$

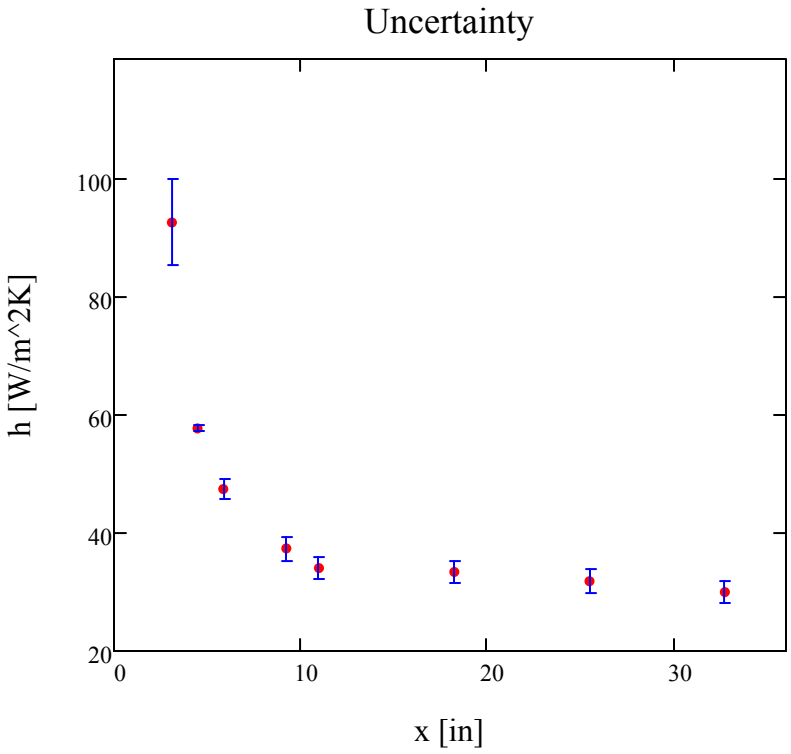


$$A_{pix} := 0.02\,\text{in}\cdot 0.02\,\text{in} = 4 \times 10^{-4}\,\text{in}^2$$

$$Q_{CONV} := \overrightarrow{\left[h \cdot A_{pix} \cdot \left(T_{avg} - T_{\infty}\right)\right]} = \begin{pmatrix} 9.49 \times 10^{-5} \\ 9 \times 10^{-5} \\ 8.71 \times 10^{-5} \\ 8.15 \times 10^{-5} \\ 7.74 \times 10^{-5} \\ 7.99 \times 10^{-5} \\ 8.14 \times 10^{-5} \\ 7.54 \times 10^{-5} \end{pmatrix} W$$

$$Q_{FLUX} := \overrightarrow{\left(\frac{E \cdot I}{A_t} \cdot A_{pix}\right)} = \begin{pmatrix} 1.39 \times 10^{-4} \\ 1.39 \times 10^{-4} \\ 1.39 \times 10^{-4} \\ 1.39 \times 10^{-4} \\ 1.39 \times 10^{-4} \\ 1.41 \times 10^{-4} \\ 1.52 \times 10^{-4} \\ 1.42 \times 10^{-4} \end{pmatrix} \cdot W$$

$$Q_{HL} := \overrightarrow{\left[\frac{k_p}{t_p} \cdot A_{pix} \cdot \left(T_{SS} - T_{UP}\right)\right]} = \begin{pmatrix} 4.23 \times 10^{-5} \\ 4.45 \times 10^{-5} \\ 4.6 \times 10^{-5} \\ 5.13 \times 10^{-5} \\ 5.52 \times 10^{-5} \\ 4.5 \times 10^{-5} \\ 4.99 \times 10^{-5} \\ 4.93 \times 10^{-5} \end{pmatrix} W$$

$$Q_{RAD} := \overrightarrow{\left[\sigma \cdot \varepsilon \cdot A_{pix} \cdot \left(T_{avg}^{4} - T_{\infty}^{4}\right)\right]} = \begin{pmatrix} 5.81 \times 10^{-6} \\ 8.94 \times 10^{-6} \\ 1.06 \times 10^{-5} \\ 1.26 \times 10^{-5} \\ 1.32 \times 10^{-5} \\ 1.39 \times 10^{-5} \\ 1.49 \times 10^{-5} \\ 1.47 \times 10^{-5} \end{pmatrix} \cdot W$$

$$\frac{Q_{HL}}{Q_{FLUX}} = \begin{pmatrix} 30.33 \\ 31.89 \\ 32.99 \\ 36.84 \\ 39.64 \\ 31.86 \\ 32.8 \\ 34.86 \end{pmatrix} \cdot \%$$

$$\frac{Q_{CONV}}{Q_{FLUX}} = \begin{pmatrix} 68.01 \\ 64.56 \\ 62.45 \\ 58.53 \\ 55.56 \\ 56.64 \\ 53.48 \\ 53.28 \end{pmatrix} \cdot \%$$

$$\frac{Q_{RAD}}{Q_{FLUX}} = \begin{pmatrix} 4.16 \\ 6.41 \\ 7.58 \\ 9.06 \\ 9.46 \\ 9.87 \\ 9.82 \\ 10.36 \end{pmatrix} \cdot \%$$

$$\text{mean}\left(\frac{Q_{HL}}{Q_{FLUX}}\right) = 33.9 \cdot \%$$

$$\text{mean}\left(\frac{Q_{CONV}}{Q_{FLUX}}\right) = 59.06 \cdot \%$$

$$\text{mean}\left(\frac{Q_{RAD}}{Q_{FLUX}}\right) = 8.34 \cdot \%$$

# APPENDIX C

## Test Data

This appendix provides the test data for the all of the accelerated cases, as well as the un-accelerated 052996.04_x10_SSL and 113012.04_IRT cases.

Table C.1: Accelerated Smooth Laminar case

| Parameter | 0a | 0b | 0c | 1a | 1b | 2 | 3 | 4 |
|---|---|---|---|---|---|---|---|---|
| x (in) | 3.10 | 4.48 | 5.85 | 9.23 | 10.98 | 18.23 | 25.48 | 32.73 |
| $A_t$ ($in^2$) | 35.06 | 35.06 | 35.06 | 44.62 | 44.62 | 44.62 | 44.62 | 44.62 |
| $\varepsilon$ | 0.95 | 0.95 | 0.95 | 0.95 | 0.95 | 0.95 | 0.95 | 0.95 |
| $\sigma$ ($W/m^2K^4$) | 5.67e-8 | 5.67e-8 | 5.67e-8 | 5.67e-8 | 5.67e-8 | 5.67e-8 | 5.67e-8 | 5.67e-8 |
| $t_p$ (in) | 0.72 | 0.72 | 0.72 | 0.72 | 0.72 | 0.72 | 0.72 | 0.72 |
| $C_k$ | 0.90 | 0.90 | 0.90 | 0.90 | 0.90 | 1.05 | 1.10 | 1.05 |
| E (V) | 5.92 | 5.92 | 5.92 | 5.88 | 5.88 | 5.92 | 6.20 | 6.05 |
| I (A) | 2.09 | 2.09 | 2.09 | 2.64 | 2.64 | 2.60 | 2.74 | 2.59 |
| $k_p$ (W/mK) | 0.205 | 0.205 | 0.205 | 0.205 | 0.205 | 0.205 | 0.205 | 0.205 |
| $T_{SS}$ (K) | 319.76 | 321.52 | 321.26 | 322.24 | 324.25 | 322.81 | 327.21 | 328.86 |
| $T_{UP}$ (K) | 300.50 | 301.44 | 302.05 | 302.88 | 303.25 | 304.35 | 305.99 | 306.63 |
| $T_\infty$ (K) | 298.05 | 298.05 | 298.05 | 298.05 | 298.05 | 298.05 | 298.05 | 298.05 |
| $T_{IR}$ (K) | 306.14 | 307.52 | 308.92 | 310.68 | 311.31 | 313.76 | 316.06 | 317.87 |
| h ($W/m^2K$) | 37.75 ± 2.00 | 30.48 ± 2.05 | 26.54 ± 1.97 | 21.06 ± 0.59 | 18.49 ± 0.50 | 14.05 ± 0.84 | 12.01 ± 0.84 | 7.92 ± 0.79 |

Table C.2: Accelerated Smooth Turbulent case

| Parameter | 0a | 0b | 0c | 1a | 1b | 2 | 3 | 4 |
|---|---|---|---|---|---|---|---|---|
| x (in) | 3.10 | 4.48 | 5.85 | 9.23 | 10.98 | 18.23 | 25.48 | 32.73 |
| $A_t$ ($in^2$) | 35.06 | 35.06 | 35.06 | 44.62 | 44.62 | 44.62 | 44.62 | 44.62 |
| $\varepsilon$ | 0.95 | 0.95 | 0.95 | 0.95 | 0.95 | 0.95 | 0.95 | 0.95 |
| $\sigma$ ($W/m^2K^4$) | 5.67e-8 | 5.67e-8 | 5.67e-8 | 5.67e-8 | 5.67e-8 | 5.67e-8 | 5.67e-8 | 5.67e-8 |
| $t_p$ (in) | 0.72 | 0.72 | 0.72 | 0.72 | 0.72 | 0.72 | 0.72 | 0.72 |
| $C_k$ | 0.90 | 0.90 | 0.90 | 0.90 | 0.90 | 1.05 | 1.10 | 1.05 |
| E (V) | 5.82 | 5.82 | 5.82 | 5.86 | 5.86 | 5.97 | 6.18 | 6.05 |
| I (A) | 2.10 | 2.10 | 2.10 | 2.65 | 2.65 | 2.64 | 2.75 | 2.61 |
| $k_p$ (W/mK) | 0.205 | 0.205 | 0.205 | 0.205 | 0.205 | 0.205 | 0.205 | 0.205 |
| $T_{SS}$ (K) | 310.53 | 311.99 | 313.22 | 316.12 | 317.73 | 314.98 | 317.90 | 317.93 |
| $T_{UP}$ (K) | 295.91 | 296.62 | 297.32 | 298.39 | 298.65 | 299.44 | 300.64 | 300.88 |
| $T_\infty$ (K) | 295.19 | 295.19 | 295.19 | 295.19 | 295.19 | 295.19 | 295.19 | 295.19 |
| $T_{IR}$ (K) | 299.20 | 301.28 | 302.35 | 303.55 | 303.91 | 304.48 | 305.21 | 304.91 |
| h ($W/m^2K$) | 92.39 ± 7.30 | 57.60 ± 0.41 | 47.36 ± 1.84 | 37.34 ± 1.97 | 34.00 ± 1.82 | 33.35 ± 1.76 | 31.78 ± 2.05 | 29.94 ± 1.92 |

Table C.3: Accelerated 113012.04_IRT case

| Parameter | 0a | 0b | 0c | 1a | 1b | 2 | 3 | 4 |
|---|---|---|---|---|---|---|---|---|
| x (in) | 3.10 | 4.48 | 5.85 | 9.23 | 10.98 | 18.23 | 25.48 | 32.73 |
| $A_t$ ($in^2$) | 35.06 | 35.06 | 35.06 | 44.62 | 44.62 | 44.62 | 44.62 | 44.62 |
| ε | 0.95 | 0.95 | 0.95 | 0.95 | 0.95 | 0.95 | 0.95 | 0.95 |
| σ ($W/m^2K^4$) | 5.67e-8 | 5.67e-8 | 5.67e-8 | 5.67e-8 | 5.67e-8 | 5.67e-8 | 5.67e-8 | 5.67e-8 |
| $t_p$ (in) | 0.72 | 0.72 | 0.72 | 0.72 | 0.72 | 0.72 | 0.72 | 0.72 |
| $C_k$ | 0.90 | 0.90 | 0.90 | 0.90 | 0.90 | 1.05 | 1.10 | 1.05 |
| E (V) | 5.85 | 5.85 | 5.85 | 5.88 | 5.88 | 5.91 | 6.23 | 6.05 |
| I (A) | 2.09 | 2.09 | 2.09 | 2.64 | 2.64 | 2.63 | 2.73 | 2.63 |
| $k_p$ (W/mK) | 0.205 | 0.205 | 0.205 | 0.205 | 0.205 | 0.205 | 0.205 | 0.205 |
| $T_{SS}$ (K) | 315.72 | 317.26 | 317.09 | 318.03 | 318.01 | 315.48 | 316.32 | 316.20 |
| $T_{UP}$ (K) | 297.00 | 297.81 | 298.36 | 299.02 | 299.24 | 299.74 | 300.42 | 300.59 |
| $T_\infty$ (K) | 294.61 | 294.61 | 294.61 | 294.61 | 294.61 | 294.61 | 294.61 | 294.61 |
| $T_{IR}$ (K) | 302.56 | 304.06 | 305.36 | 307.24 | 308.85 | 300.59 | 301.34 | 301.68 |
| h ($W/m^2K$) | 38.57 ± 1.99 | 30.72 ± 2.05 | 26.93 ± 1.97 | 21.64 ± 0.58 | 18.64 ± 0.27 | 53.58 ± 3.78 | 53.02 ± 4.20 | 46.28 ± 3.11 |

Table C.4: Accelerated 053096.01_x10 case

| Parameter | 0a | 0b | 0c | 1a | 1b | 2 | 3 | 4 |
|---|---|---|---|---|---|---|---|---|
| x (in) | 3.10 | 4.48 | 5.85 | 9.23 | 10.98 | 18.23 | 25.48 | 32.73 |
| $A_t$ ($in^2$) | 35.06 | 35.06 | 35.06 | 44.62 | 44.62 | 44.62 | 44.62 | 44.62 |
| $\varepsilon$ | 0.95 | 0.95 | 0.95 | 0.95 | 0.95 | 0.95 | 0.95 | 0.95 |
| $\sigma$ ($W/m^2K^4$) | 5.67e-8 | 5.67e-8 | 5.67e-8 | 5.67e-8 | 5.67e-8 | 5.67e-8 | 5.67e-8 | 5.67e-8 |
| $t_p$ (in) | 0.72 | 0.72 | 0.72 | 0.72 | 0.72 | 0.72 | 0.72 | 0.72 |
| $C_k$ | 0.90 | 0.90 | 0.90 | 0.90 | 0.90 | 1.05 | 1.10 | 1.05 |
| E (V) | 5.89 | 5.89 | 5.89 | 5.84 | 5.84 | 5.86 | 6.19 | 6.01 |
| I (A) | 2.07 | 2.07 | 2.07 | 2.64 | 2.64 | 2.63 | 2.75 | 2.63 |
| $k_p$ (W/mK) | 0.205 | 0.205 | 0.205 | 0.205 | 0.205 | 0.205 | 0.205 | 0.205 |
| $T_{SS}$ (K) | 315.03 | 317.03 | 315.10 | 311.90 | 312.60 | 312.27 | 313.92 | 315.02 |
| $T_{UP}$ (K) | 296.36 | 297.40 | 297.79 | 297.86 | 297.64 | 298.70 | 299.67 | 300.12 |
| $T_\infty$ (K) | 294.91 | 294.91 | 294.91 | 294.91 | 294.91 | 294.91 | 294.91 | 294.91 |
| $T_{IR}$ (K) | 302.15 | 303.93 | 301.61 | 300.91 | 301.04 | 301.56 | 302.64 | 302.75 |
| h ($W/m^2K$) | 42.81 ± 1.82 | 32.11 ± 2.10 | 48.84 ± 1.65 | 60.21 ± 3.77 | 57.26 ± 3.69 | 50.87 ± 3.02 | 48.16 ± 3.18 | 42.01 ± 2.65 |

Table C.5: Accelerated 052996.04_x10_SSL case

| Parameter | 0a | 0b | 0c | 1a | 1b | 2 | 3 | 4 |
|---|---|---|---|---|---|---|---|---|
| x (in) | 3.10 | 4.48 | 5.85 | 9.23 | 10.98 | 18.23 | 25.48 | 32.73 |
| $A_t$ ($in^2$) | 35.06 | 35.06 | 35.06 | 44.62 | 44.62 | 44.62 | 44.62 | 44.62 |
| ε | 0.95 | 0.95 | 0.95 | 0.95 | 0.95 | 0.95 | 0.95 | 0.95 |
| σ ($W/m^2K^4$) | 5.67e-8 | 5.67e-8 | 5.67e-8 | 5.67e-8 | 5.67e-8 | 5.67e-8 | 5.67e-8 | 5.67e-8 |
| $t_p$ (in) | 0.72 | 0.72 | 0.72 | 0.72 | 0.72 | 0.72 | 0.72 | 0.72 |
| $C_k$ | 0.90 | 0.90 | 0.90 | 0.90 | 0.90 | 1.05 | 1.10 | 1.05 |
| E (V) | 5.81 | 5.81 | 5.81 | 5.87 | 5.87 | 5.89 | 6.17 | 6.10 |
| I (A) | 2.08 | 2.08 | 2.08 | 2.64 | 2.64 | 2.65 | 2.76 | 2.59 |
| $k_p$ (W/mK) | 0.205 | 0.205 | 0.205 | 0.205 | 0.205 | 0.205 | 0.205 | 0.205 |
| $T_{SS}$ (K) | 315.39 | 317.43 | 317.26 | 316.31 | 315.78 | 316.03 | 318.56 | 318.70 |
| $T_{UP}$ (K) | 296.57 | 297.54 | 298.12 | 298.78 | 298.65 | 299.88 | 301.00 | 301.13 |
| $T_\infty$ (K) | 295.32 | 295.32 | 295.32 | 295.32 | 295.32 | 295.32 | 295.32 | 295.32 |
| $T_{IR}$ (K) | 302.55 | 304.01 | 305.40 | 303.94 | 301.07 | 300.45 | 301.08 | 300.41 |
| h ($W/m^2K$) | 41.80 ± 1.77 | 32.56 ± 2.04 | 27.95 ± 2.01 | 36.23 ± 1.61 | 57.99 ± 4.40 | 62.83 ± 4.99 | 59.13 ± 5.71 | 61.54 ± 5.49 |

Table C.6: Accelerated 052996.04_x10 case

| Parameter | 0a | 0b | 0c | 1a | 1b | 2 | 3 | 4 |
|---|---|---|---|---|---|---|---|---|
| x (in) | 3.10 | 4.48 | 5.85 | 9.23 | 10.98 | 18.23 | 25.48 | 32.73 |
| $A_t$ ($in^2$) | 35.06 | 35.06 | 35.06 | 44.62 | 44.62 | 44.62 | 44.62 | 44.62 |
| $\varepsilon$ | 0.95 | 0.95 | 0.95 | 0.95 | 0.95 | 0.95 | 0.95 | 0.95 |
| $\sigma$ ($W/m^2K^4$) | 5.67e-8 | 5.67e-8 | 5.67e-8 | 5.67e-8 | 5.67e-8 | 5.67e-8 | 5.67e-8 | 5.67e-8 |
| $t_p$ (in) | 0.72 | 0.72 | 0.72 | 0.72 | 0.72 | 0.72 | 0.72 | 0.72 |
| $C_k$ | 0.90 | 0.90 | 0.90 | 0.90 | 0.90 | 1.05 | 1.10 | 1.05 |
| E (V) | 5.80 | 5.80 | 5.80 | 5.86 | 5.86 | 5.92 | 6.18 | 6.04 |
| I (A) | 2.08 | 2.08 | 2.08 | 2.64 | 2.64 | 2.69 | 2.78 | 2.62 |
| $k_p$ (W/mK) | 0.205 | 0.205 | 0.205 | 0.205 | 0.205 | 0.205 | 0.205 | 0.205 |
| $T_{SS}$ (K) | 314.91 | 315.64 | 315.09 | 313.61 | 314.02 | 316.07 | 318.13 | 318.85 |
| $T_{UP}$ (K) | 296.04 | 297.07 | 297.58 | 297.97 | 297.86 | 299.53 | 300.64 | 300.96 |
| $T_\infty$ (K) | 294.84 | 294.84 | 294.84 | 294.84 | 294.84 | 294.84 | 294.84 | 294.84 |
| $T_{IR}$ (K) | 298.63 | 299.05 | 299.39 | 300.31 | 300.61 | 300.44 | 301.12 | 300.41 |
| h ($W/m^2K$) | 84.93 ± 8.96 | 76.55 ± 6.67 | 72.73 ± 5.06 | 63.62 ± 4.71 | 59.12 ± 4.25 | 58.26 ± 4.36 | 55.01 ± 4.93 | 55.09 ± 4.72 |

Table C.7: Un-accelerated 113012.04_IRT case

| Parameter | 0a | 0b | 0c | 1a | 1b | 2 | 3 | 4 |
|---|---|---|---|---|---|---|---|---|
| x (in) | 3.10 | 4.48 | 5.85 | 9.23 | 10.98 | 18.23 | 25.48 | 32.73 |
| $A_t$ ($in^2$) | 35.06 | 35.06 | 35.06 | 44.62 | 44.62 | 44.62 | 44.62 | 44.62 |
| ε | 0.95 | 0.95 | 0.95 | 0.95 | 0.95 | 0.95 | 0.95 | 0.95 |
| σ ($W/m^2K^4$) | 5.67e-8 | 5.67e-8 | 5.67e-8 | 5.67e-8 | 5.67e-8 | 5.67e-8 | 5.67e-8 | 5.67e-8 |
| $t_p$ (in) | 0.72 | 0.72 | 0.72 | 0.72 | 0.72 | 0.72 | 0.72 | 0.72 |
| $C_k$ | 0.90 | 0.90 | 0.90 | 0.90 | 0.90 | 1.05 | 1.10 | 1.05 |
| E (V) | 5.75 | 5.75 | 5.75 | 5.90 | 5.90 | 5.80 | 6.16 | 6.05 |
| I (A) | 2.06 | 2.06 | 2.06 | 2.65 | 2.65 | 2.64 | 2.73 | 2.63 |
| $k_p$ (W/mK) | 0.205 | 0.205 | 0.205 | 0.205 | 0.205 | 0.205 | 0.205 | 0.205 |
| $T_{SS}$ (K) | 316.76 | 318.20 | 318.23 | 319.42 | 320.79 | 316.27 | 316.96 | 316.53 |
| $T_{UP}$ (K) | 299.71 | 299.23 | 299.76 | 299.58 | 299.62 | 300.13 | 300.70 | 300.71 |
| $T_\infty$ (K) | 294.37 | 294.37 | 294.37 | 294.37 | 294.37 | 294.37 | 294.37 | 294.37 |
| $T_{IR}$ (K) | 303.83 | 305.13 | 306.57 | 309.00 | 310.44 | 301.15 | 302.09 | 302.45 |
| h ($W/m^2K$) | 31.50 ± 2.07 | 25.16 ± 1.94 | 21.88 ± 1.81 | 17.46 ± 0.23 | 14.49 ± 0.19 | 44.69 ± 3.00 | 43.87 ± 3.25 | 39.77 ± 2.55 |

Table C.8: Un-accelerated 052996.04_x10_SSL case

| Parameter | 0a | 0b | 0c | 1a | 1b | 2 | 3 | 4 |
|---|---|---|---|---|---|---|---|---|
| x (in) | 3.10 | 4.48 | 5.85 | 9.23 | 10.98 | 18.23 | 25.48 | 32.73 |
| $A_t$ ($in^2$) | 35.06 | 35.06 | 35.06 | 44.62 | 44.62 | 44.62 | 44.62 | 44.62 |
| ε | 0.95 | 0.95 | 0.95 | 0.95 | 0.95 | 0.95 | 0.95 | 0.95 |
| σ ($W/m^2K^4$) | 5.67e-8 | 5.67e-8 | 5.67e-8 | 5.67e-8 | 5.67e-8 | 5.67e-8 | 5.67e-8 | 5.67e-8 |
| $t_p$ (in) | 0.72 | 0.72 | 0.72 | 0.72 | 0.72 | 0.72 | 0.72 | 0.72 |
| $C_k$ | 0.90 | 0.90 | 0.90 | 0.90 | 0.90 | 1.05 | 1.10 | 1.05 |
| E (V) | 5.88 | 5.88 | 5.88 | 5.89 | 5.89 | 5.85 | 6.04 | 6.00 |
| I (A) | 2.09 | 2.09 | 2.09 | 2.66 | 2.66 | 2.62 | 2.71 | 2.64 |
| $k_p$ (W/mK) | 0.205 | 0.205 | 0.205 | 0.205 | 0.205 | 0.205 | 0.205 | 0.205 |
| $T_{SS}$ (K) | 317.51 | 319.00 | 319.17 | 317.15 | 316.13 | 315.31 | 317.65 | 319.57 |
| $T_{UP}$ (K) | 299.59 | 299.61 | 300.15 | 299.51 | 299.06 | 299.88 | 300.83 | 301.42 |
| $T_\infty$ (K) | 294.15 | 294.15 | 294.15 | 294.15 | 294.15 | 294.15 | 294.15 | 294.15 |
| $T_{IR}$ (K) | 304.15 | 305.57 | 307.37 | 304.51 | 301.13 | 300.71 | 300.99 | 301.10 |
| h ($W/m^2K$) | 30.64 ± 2.06 | 24.77 ± 1.92 | 20.83 ± 1.75 | 29.58 ± 0.96 | 47.64 ± 2.86 | 47.84 ± 3.20 | 47.33 ± 4.02 | 42.80 ± 3.31 |

# REFERENCES


[1] Addy, H. E., 2000, "Ice Accretions and Icing Effects for Modern Airfoil," NASA/TP-2000-210031.

[2] Petty, K. R., and Floyd, C. D. J., 2004, "A Statistical Review of Aviation Airframe Icing Accidents in the U.S.," 11th American Society for Microbiology Conference on Aviation, Range, and Aerospace, Hyannis, MA.

[3] Wright, W. B., and Bidwell, C. S., 2014, "How Roughness Research can Improve LEWICE," Invited Oral Presentation, 6th AIAA Atmospheric and Space Environments Conference, 16-20 June, Atlanta, GA.

[4] Tecson, L., 2013, "Convective Heat Transfer from Realistic Ice Roughness Distributions," MS thesis, Department of Mechanical Engineering, Baylor University.

[5] Walker, C. W., 2014, "Convection from Manufactured Ice Roughness with Varying Flux Boundary Conditions," MS thesis, Department of Mechanical Engineering, Baylor University.

[6] McClain, S.T., Reed, D., Vargas, M., Kreeger, R.E., and Tsao, J.-C., 2014, "Ice roughness in Short Duration SLD Icing Events," 6th AIAA Atmospheric and Space Environments Conference, 16-20 June, Atlanta, GA, AIAA-2014-2330.

[7] McClain, S.T. and Kreeger, R.E., (2013), "Assessment of Ice Shape Roughness Using a Self-Organizing Map Approach," Presented at the 5th AIAA Atmospheric and Space Environments Conference, June 24-27, 2013, San Diego, CA, AIAA-2013-2546.

[8] Munson, B.R., Okiishi, T.H., Huebsch, W.W., and Rothmayer, A.P., 2013, *Fundamentals of Fluid Mechanics*, 7th ed., John Wiley & Sons, Inc., Hoboken, NJ, pp. 482.

[9] Incropera, F. P., Dewitt, D. P., Bergman, T. L., and Lavine, A. S., (2007), *Fundamentals of Heat and Mass Transfer*, Hoboken, NJ: John Wiley & Sons, Inc., 6th edition.

[10] Smith, A.G., and Spaulding, D.B., (1958), "Heat Transfer in a Laminar Boundary Layer with Constant Fluid Properties and Constant Wall Temperature," *J. Roy. Aero. Soc.*, Vol. 62, pg 60-64.

[11] Ambrok, G. S., (1957), "Approximate Solutions of the Equations for the Thermal Boundary Layer with Variations in the Boundary Layer Structure," *Soviet Phys.-Tech. Phys.*, Vol. 2, No. 9, pg 1979-1986.

[12] Nikuradse, J., 1933, "Laws for Flows in Rough Pipes," *VDI-Forschungsheft*, **4**, pp. 361.

[13] Schlichting, H., 1936, "Experimental Investigation of the Problem of Surface Roughness," TM-832, National Advisory Committee on Aeronautics.

[14] J. P. Bons and S. T. McClain, "The Effect of Real Turbine Roughness with Pressure Gradient on Heat Transfer," *Journal of Turbomachinery*, Vol. 126, No. 3, pg 385-394, 2004.

[15] Coleman, H. W., Moffat, R. J., and Kays, W. M., 1981, "Heat Transfer in the Accelerated Fully Rough Turbulent Boundary Layer," *Journal of Heat Transfer*, Vol. 103, No. 1, pp. 153-158.

[16] Chakroun, W., and Taylor, R. P., 1993, "The Effects of Moderately Strong Acceleration on Heat Transfer in the Turbulent Rough-Wall Boundary Layer," *Journal of Heat Transfer*, Vol. 115, No. 3, pp. 1187-1201.

[17] Turner, A. B., Hubbe-Walker, S. E., and Bayley, F. J., 2000, "Fluid Flow and Heat Transfer Over Straight and Curved Rough Surfaces," *Int. Journal of Heat Transfer*, Vol. 43, pp. 251-262.

[18] Mart, S. R., 2011, "The Effect of Roughness Element Thermal Conductivity on Turbulent Convection," MS thesis, Department of Mechanical Engineering, Baylor University.

[19] McClain, S. T., Vargas, M., Kreeger, R. E., and Tsao, J. C., 2007, "Heat Transfer from Protuberances", *Journal of Thermophysics and Heat Transfer*, **21**(2), pp. 337-345.

[20] Bons, J. P., McClain, S. T., Wang, Z. J., Chi, X., Shih, T. I., 2005, "A Comparison of approximate vs. Exact Geometrical Representations of Roughness for CFD Calculations of $c_f$ and St," ASME International Mechanical Engineering Congress and Exposition.

[21] "Compliance of Transport Category Airplanes with Certification Requirements for Flight in Icing Conditions," 2014, AC No: 25-28.

[22] "14 CFR Part 25: Airworthiness Standards: Transport Category Airplanes - Appendix C, Part I: Atmospheric Icing Conditions," 2012, *Code of Federal Regulations*.

[23] "14 CFR Part 25: Airworthiness Standards: Transport Category Airplanes - Appendix O, Part I: Meteorology," 2014, *Code of Federal Regulations*.

[24] Olsen, W., Walker, E., 1986, "Experimental Evidence for Modifying the Current Physical Model for Ice Accretion on Aircraft Surfaces," NASA TM-87184.

[25] Anderson, D. N., and Shin, J., 1997, "Characterization of Ice Roughness from Simulated Icing Encounters," NASA TM-107400.

[26] Messinger, B.L., 1953, "Equilibrium Temperature of an Unheated Icing Surface as a Function of Air Speed," *Journal of Aeronautical Sciences*, pp. 29-42.

[27] Dukhan, N., Van Fossen, G. J., DeWitt, K. J., Masiulaniec, K. C., 2003, "Experimental Frossling Numbers for Ice-Roughened NACA 0012 Airfoils," *Journal of Aircraft* **40**(6), pp. 1161-1167.

[28] Wright, W.B., 2002, "User Manual for the NASA Glenn Ice Accretion Code LEWICE," NASA/CR-2002-211793.

[29] Shin, J., 1994, "Characteristics of Surface Roughness Associated With Leading Edge Ice Accretion," NASA TM-106459.

[30] Bons, J. P., 2002, "St and Cf Augmentation for Real Turbine Roughness With Elevated Freestream Turbulence," *Journal of Turbomachinery*, **124**, pp. 632–644.

[31] Poinsatte, P.E., Van Fossen, G.J., and DeWitt, K.J., 1990, "Convective Heat Transfer Measurements from a NACA 0012 Airfoil in Flight and in the NASA Lewis Icing Research Tunnel," NASA TM-102448.

[32] Bragg, M. B., Cummings, M. J., Lee, S., Henze, C. M., 1996, "Boundary-Layer and Heat-Transfer Measurements on an Airfoil with Simulated Ice Roughness," AIAA Paper 96-0866.

[33] Han, Y. and Palacios, J., (2014), "Transient Heat Transfer Measurements of Surface Roughnes due to Ice Accretion," 6th AIAA Atmospheric and Space Environments Conference, 16-20 June, Atlanta, GA, AIAA-2014-2464.

[34] Anderson, D. N., Hentschel, D. B., and Ruff, G. A., 1998, "Measurement and Correlation of Ice Accretion Roughness," NASA CR-2003-211823.

[35] Tecson, L. and McClain, S.T., (2013), "Convective Enhancement of Surfaces with Realistic Ice Roughness Distributions," 5th AIAA Atmospheric and Space Environments Conference, 24-27 June, San Diego, CA, AIAA-2013-3060.

[36] Tecson, L. and McClain, S.T., (2013), "Modeling of Realistic Ice Roughness Element Distributions to Characterize Convective Heat Transfer," 5th AIAA Atmospheric and Space Environments Conference, 24-27 June, San Diego, CA, AIAA-2013-3059.

[37] Walker C. W., McClain S. T., and Shannon T. A., (2014), "Convection from Ice Roughness with Varying Flux Boundary Conditions," 6th AIAA Atmospheric and Space Environments Conference, 16-20 June, Atlanta, GA, AIAA-2014-2463.

[38] Altuglas International, Arkema Group, (2006), "Plexiglas-Acrylic Sheet: General Information and Physical Properties," www.plexiglas.com.

[39] The International Association for the Properties of Water and Steam, 2007, "Revised Release on the IAPWS Industrial Formulation 1997 for the Thermodynamic Properties of Water and Steam," http://www.iapws.org/.

[40] White, F. M., 2006, *Viscous Fluid Flow*, 3rd Ed, Boston, McGraw-Hill, Inc., New York, NY.

[41] Wilke, C. R., 1950, "A Viscosity Equation for Gas Mixtures," *Journal of Chemical Physics*, **18**(4), pp. 517-519.

[42] Coleman, H. W., and Steele, W. G., 1999, *Experimentation and Uncertainty Analysis for Engineers*, 2nd ed., John Wiley and Sons, Inc., Hoboken, NJ.

[43] Kline, S. J., and McClintock, F. A., 1953, "Describing Uncertainties in Single-Sample Experiments," *Mechanical Engineering*, **75**, pp. 3-8.